

**SYNTHESIS, REACTIVITY AND
COMPUTATIONAL STUDIES OF REDOX-
ACTIVE INDIUM THIOLATE COMPLEXES**

By
Padmapriya Srinivasan

A thesis submitted to the
Department of Chemistry and Biochemistry
Mount Allison University
in partial fulfillment of the requirements for the
Bachelor of Science degree with Honours
April 2022

Thesis Committee

Supervisor

Dr. Glen Briand
Professor of Chemistry

Reviewer

Dr. Gregory Sandala
Professor of Chemistry

Contents

<i>Thesis Committee</i>	<i>1</i>
<i>Acknowledgements</i>	<i>5</i>
<i>List of Figures, Tables and Schemes</i>	<i>6</i>
<i>List of Spectra and Tables in Appendix</i>	<i>9</i>
<i>Glossary of Abbreviation and Symbols</i>	<i>11</i>
<i>Abstract</i>	<i>12</i>
1. Introduction	13
1.1 Green Chemistry	13
1.2 Catalysis	16
1.3 Indium complexes as catalysts	18
1.4 Ligands for designing redox-active indium compounds	19
1.4.1 Redox-active ligands.....	19
1.4.2 Redox-active toluene-3,4-dithiol and <i>o</i> -aminobenzenethiol ligands.....	21
1.4.3 Pincer ligand	23
1.5 Computational Chemistry	24
1.6 Current study	24
1.6.1 Synthesis and characterization of target compounds	24
1.6.2 Computational calculations.....	25
2. Experimental	26
2.1 General Methods and Considerations	26
2.1.1 Instrumentation	26
2.1.2 Reagents.....	26
2.2 Synthesis of C₆H₃Br-2,6-(CH₂Br)₂ (5)	27
2.2.1 Synthesis of C ₆ H ₃ Br-2,6-(CH ₂ Br) ₂ (5) using ultraviolet light (UV) ³⁸	27
2.2.2 Synthesis of C ₆ H ₃ Br-2,6-(CH ₂ Br) ₂ (5) using infrared light (IR) ³⁹	27
2.3 Synthesis of C₆H₃Br(CH₂NMe₂)₂-2,6 (6) ⁴⁰	27
2.4 Synthesis of (NCN)InCl₂ (7) ⁴¹	28

2.5 Synthesis of InMe₂Cl (8) ⁴²	28
2.6 Synthesis of (NCN)InMe₂ (9) ⁴⁴	28
2.7 Attempted synthesis of (NCN)In(ABT) (4)	29
2.7.1 Attempted synthesis of (NCN)In(ABT) via hydrocarbon elimination	29
2.7.2 Attempted synthesis of (NCN)In(ABT) via salt elimination using sodium hydride	29
2.8 Synthesis of (NCN)In(ABT) (4) via salt elimination using butyllithium	29
2.9 Synthesis of (NCN)In(HABT)₂ (10)	30
2.10 Reactions of indium complexes 1–4 with I₂ as an oxidizing agent	31
2.10.1 Addition of (NCN)In(TDT) (2) to a solution of I ₂	31
2.10.2 Addition of [MeIn(TDT)py] ₂ (1) to a solution of I ₂	31
2.10.3 Reaction of (NCN)In(TDT) (2) with excess I ₂	32
2.10.4 Addition of [MeIn(ABT)py] ₂ (3) to a solution of I ₂	32
2.10.5 Addition of (NCN)In(TDT) (4) to a solution of I ₂	32
2.10.6 Addition of [MeIn(TDT)py] ₂ (1) to four equivalence of I ₂	33
2.11 Computational methods	33
3. Results and Discussion	33
General Synthesis	33
3.1 Synthesis of C₆H₃Br-2,6-(CH₂Br)₂ (5)	33
3.1.1 Synthesis of C ₆ H ₃ Br-2,6-(CH ₂ Br) ₂ (5) using UV light	33
3.1.2 Synthesis of C ₆ H ₃ Br-2,6-(CH ₂ Br) ₂ (5) using infrared light (IR)	34
3.2 Synthesis of (NCN)Br (6)	35
3.3 Synthesis of InMe₂Cl (8)	35
3.4 Synthesis of (NCN)InMe₂ (9)	37
3.5 Attempted synthesis of (NCN)In(ABT) (4)	38
3.5.1 Attempted synthesis of (NCN)In(ABT) (4) via hydrocarbon elimination	38
3.5.2 Attempted synthesis of (NCN)In(ABT) (4) via salt elimination using sodium hydride	39
3.6 Synthesis of (NCN)In(ABT) (4) and accidental synthesis of (NCN)In(HABT)₂ (10) via salt elimination using n-butyllithium	39
Reactivity and Theoretical Calculations	43
3.7 [MeIn(TDT)py]₂ (1)	43

3.7.1 Structure of [MeIn(TDT)py] ₂ (1).....	43
3.7.2 Dimerization of [MeIn(TDT)py] ₂ (1).....	44
3.7.3 Reactivity of [MeIn(TDT)py] ₂ (1) with a mild oxidizing agent	46
3.7.4 Theoretical calculations on [MeIn(TDT)py] ₂ (1).....	49
3.8 (NCN)In(TDT) (2).....	51
3.8.1 Structure of (NCN)In(TDT) (2).....	51
3.8.2 Reaction of (NCN)In(TDT) (2) with I ₂	52
3.8.3 Theoretical calculations on (NCN)In(TDT) (2).....	53
3.9 [MeIn(ABT)py]₂ (3)	56
3.9.1 Structure of [MeIn(ABT)py] ₂ (3).....	56
3.9.2 Dimerization of [MeIn(ABT)py] ₂ (3) via bridging nitrogen atoms of ABT	58
3.9.3 Reaction of [MeIn(ABT)py] ₂ (3) with I ₂	59
3.9.4 Theoretical calculations on [MeIn(ABT)py] ₂ (3).....	60
3.10 (NCN)In(ABT) (4).....	64
3.10.1 Structure of (NCN)In(ABT) (4).....	64
3.10.2 Reaction of (NCN)In(ABT) (4) with I ₂	64
3.10.3 Theoretical calculations on (NCN)In(ABT) (4).....	65
3.10.4 Investigation of frontier molecular orbitals of (NCN)In(TDT) (2) and (NCN)In(ABT) (4).....	66
4. Conclusions	69
5. Future Directions	69
6. References	71
7. Appendices.....	75
Appendix A: Spectroscopic data	75
Appendix B: Calculated energies of molecules using PBE1PBE-GD3BJ/def2-TZVP	85

Acknowledgements

Over the last four years as an undergrad student at Mount Allison I have learned a great deal not only about science and academics, but also about myself, and for this I give thanks. Firstly, I want to convey my sincere gratitude to Dr. Glen Briand, a model supervisor and a great professor. Dr. Briand allowed me the freedom to incorporate computational calculations in a synthetic chemistry thesis and discover my path. I have learned a great deal from Dr. Briand directly and by subtle and not-so-subtle example. Dr. Briand was always ready to listen and advise on problems and I want to thank him for that.

Secondly, I'd like to thank my second reader and my co-supervisor Dr. Gregory Sandala. Dr. Sandala teaches advanced physical chemistry and emphasizes independent thinking and trains us on clear scientific writing. His lectures truly fuelled my interests in physical chemistry. Dr. Sandala has helped me learn a great deal about computational chemistry. I would like to thank both my supervisors for taking the time to read my thesis, give helpful comments, suggestions and listen to my arguments.

Thirdly, I owe many thanks to Dr. Andrew Grant, who teaches the majority of organic chemistry at Mount Allison, for always believing in me and encouraging me to take higher level chemistry courses in my first year. I would like to thank him for his support with my independent study in organic synthesis which helped me learn important skills about research, without which I couldn't have done this work.

I would like to extend my acknowledgement to the Department of Chemistry and Biochemistry at Mount Allison. To the lab instructors, Susan and Eva and to all my TAs, thank you for teaching me the skills required in laboratory. To Dan, thank you fixing the NMR spectrometer every time it is broken, and for always being approachable when needed. To Phil, thank you for your patience with all the nitrogen tanks I have had to get over the year. To Chris, thank you for teaching me to use the instruments in the Wild Toads lab and for always encouraging me with your kind words.

Finally, I would like to thank my family for their constant support of my academic ventures from the beginning to the present. None of this would have been possible without them. I'd also like to thank all the Metalheads—Alex.S, Viveka, Alex.M, John and Grace—for all the fun we had in lab. The conversations in lab made it a great place to work. A special thanks to Alicia for always having my back during hard times and for all the great meals we cooked together.

Thank you all for taking the time to read my thesis.

List of Figures, Tables and Schemes

Figure 1: The Twelve Principles of Green Chemistry as proposed by Anastas and Warner.⁵

Figure 2: A rhodium-based Wilkinson's catalyst undergoing a redox-active catalytic cycle.¹⁶

Figure 3: Empty p-orbital on indium (III).

Figure 4: Modes of redox-active ligands: Actor and Spectator, where M is metal and L is ligand.²⁷

Figure 5: The oxidation of *o*-amidophenolate indium (III) complex (APInI(TMEDA)) with iodine and TMEDA.

Figure 6: The structures of toluene-3,4-dithiolate (TDT)²⁻ and xanthate.

Figure 7: Deprotonation and electronic resonance structures of ligands (a) benzenedithiolate (TDT)²⁻ and (b) *o*-aminobenzenethiolate (ABT)²⁻.

Figure 8: Initially postulated (A) and later confirmed (B) structures of Ni(ABT).

Figure 9: Pincer ligand (NCN, in bolded black) stabilizing an indium-centred molecule [(NCN)InMe₂] by coordinating through its amine groups.

Figure 10: Target indium complexes in this study, where NCN = {2,6-bis[(dimethylamino)methyl]phenyl}, TDT = toluene-3,4-dithiolate and ABT = *o*-amidobenzenethiolate.

Figure 11: X-ray crystal structure of **10** (30% probability ellipsoids). Except for N-H, hydrogen atoms are omitted for clarity. Selected bond distances (Å) and angles (°): In1–N1 = 2.527(2), In–N2 = 2.557(2), In1–C1 = 2.138(3), In1–S1 = 2.4468(8), In1–S2 =

2.4487(8), C1–In1–S1 = 137.96(7), C1–In1–S2 = 114.77(7), S1–In1–S2 = 107.07(2), N1–In1–N2 = 143.07(7).

Figure 12: X-ray crystal structure of **4** (30% probability ellipsoids). Except for N-H, hydrogen atoms are omitted for clarity. Selected bond distances (Å) and angles (°): In1–C1 = 2.1169(9), In1–S1 = 2.4459(4), In1–N1 = 2.5101(9), In1–N2 = 2.538(1), In1–N3 = 2.062(1), C1–In1–S1 = 132.62(3), C1–In1–N3 = 142.24(4), S1–In1–N3 = 85.13(3), N1–In1–N2 = 148.07(3).

Figure 13: X-ray crystal structure of **4** (30% probability ellipsoids) co-crystallised with LiCl and THF. Except for N-H, hydrogen atoms are omitted for clarity.

Figure 14: X-ray crystal (left, 30% probability ellipsoids) and geometry-optimized (right) structures of [MeIn(TDT)(py)]₂ (**1**). Hydrogen atoms are omitted for clarity.

Figure 15: Chemical structures of mononuclear bis-pyridine [MeIn(TDT)py₂] (**11**) and binuclear mono-pyridine [MeIn(TDT)py]₂ (**1**).

Figure 16: Calculated structure of [MeIn(TDT)(py)]₂ (**11**). Hydrogen atoms are omitted for clarity.

Figure 17: Colour change during the addition of [MeIn(TDT)py]₂ to a solution of I₂.

Figure 18: Colour change during the sequential addition of iodine to [MeIn(TDT)py]₂.

Figure 19: HOMO of complex **1**.

Figure 20: Geometry-optimized structure and the chemical structure of **12**. Hydrogen atoms are omitted for clarity.

Figure 21: X-ray crystal (left, 30% probability ellipsoids) and geometry-optimized (right) structures of (NCN)In(TDT) (**2**). Hydrogen atoms are omitted for clarity.

Figure 22: HOMO of complex **2**.

Figure 23: HOMO of the cation radical of complex **2**.

Figure 24: Geometry-optimized structure of **13**. Hydrogen atoms are omitted for clarity.

Figure 25: X-ray crystal (left, 30% probability ellipsoids) and geometry-optimized (right) structures of [MeIn(ABT)py]₂ (**3**). Except for N-H, hydrogen atoms are omitted for clarity.

Figure 26: Geometry-optimized structures of *N*-linked (left) and *S*-linked (right) [MeIn(ABT)py]₂ dimers. Except for N-H, hydrogen atoms are omitted for clarity.

Figure 27: Center rings of the *N*-linked and *S*-linked [MeIn(ABT)py]₂ dimers. N1 in the *N*-linked ring is located behind In1*. Hydrogen atoms are omitted for clarity.

Figure 28: Colour change during the addition of [MeIn(TDT)py]₂ to a solution of I₂.

Figure 29: Geometry-optimized structure of **14**. Except for N-H, hydrogen atoms are omitted for clarity.

Figure 30: X-ray crystal (left, 30% probability ellipsoids) and geometry-optimized (right) structures of (NCN)In(ABT) (**4**). Except for N-H, hydrogen atoms are omitted for clarity.

Figure 31: Intensification of purple colour during the addition of (NCN)In(ABT) to a solution of I₂.

Figure 32: Geometry-optimized structure of complex **15**. Except for N-H, hydrogen atoms are omitted for clarity.

Table 1: Comparison of experimental and calculated bond distances (Å) and bond angles (°) of [MeIn(TDT)(py)]₂ (**1**).

Table 2: Comparison of bond distances (Å) and bond angles (°) of X-ray crystal structure and geometry-optimized structure of (NCN)In(TDT) (**2**).

Table 3: Comparison of bond distances (Å) and bond angles (°) of the X-ray crystal structure and geometry-optimized structure of [MeIn(ABT)py]₂ (**3**).

Table 4: Comparing the bond distances (Å) and the bond angles (°) of the calculated structures of *N*-linked and *S*-linked [MeIn(ABT)py]₂ (**3**) dimers.

Table 5: Frontier molecular orbitals for complexes **1** and **3** along with their calculated energies.

Table 6: Comparison of bond distances (Å) and bond angles (°) of the X-ray crystal structure and geometry-optimized structure of (NCN)In(ABT) (**4**).

Table 7: Frontier molecular orbitals of complexes **2** and **4** along with their calculated energies.

Scheme 1: Synthesis of C₆H₃Br-2,6-(CH₂Br)₂ (**5**) from 2-bromo-*m*-xylene and NBS using UV light and AIBN to initiate the radical reaction with CCl₄ as the solvent.

Scheme 2: Synthesis of C₆H₃Br-2,6-(CH₂Br)₂ (**5**) from 2-bromo-*m*-xylene and NBS using IR light with methyl acetate as the solvent.

Scheme 3: Synthesis of (NCN)Br (**6**) from C₆H₃Br-2,6-(CH₂Br)₂ and dimethyl amine.

Scheme 4: Synthesis of InMe₂Cl from trityl chloride and trimethyl indium.

Scheme 5: Synthesis of InMe_2Cl with indium trichloride and methyl lithium.

Scheme 6: Synthesis of InMe_2Cl with indium trichloride and methyl magnesium bromide.

Scheme 7: Synthesis of $(\text{NCN})\text{InMe}_2$ using $(\text{NCN})\text{Br}$, butyllithium and InMe_2Cl .

Scheme 8: Attempted synthesis of $(\text{NCN})\text{In}(\text{ABT})$ via hydrocarbon elimination.

Scheme 9: Attempted synthesis of $(\text{NCN})\text{In}(\text{ABT})$ via salt elimination using sodium hydride.

Scheme 10: Synthesis of $(\text{NCN})\text{In}(\text{ABT})$ via salt elimination using butyllithium.

Scheme 11: Synthesis of $(\text{NCN})\text{In}(\text{HABT})_2$ via salt elimination using butyllithium and two equivalence of ABT.

Scheme 12: Addition of **1** to a solution of I_2 .

Scheme 13: Addition of a catalytic amount of $[\text{MeIn}(\text{TDT})\text{py}]_2$ to a solution I_2 did not cause reduction of diiodine.

Scheme 14: Attempted addition of 4 equivalence of I_2 to a solution of $[\text{MeIn}(\text{TDT})\text{py}]_2$.

Scheme 15: Electron oxidation of TDT to form a dimer linked through the terminal sulfur atoms.

Scheme 16: Addition of **2** to half an equivalence of I_2 solution.

Scheme 17: Addition of $[\text{MeIn}(\text{ABT})\text{py}]_2$ (**3**) to a solution of I_2 .

Scheme 18: Addition of $(\text{NCN})\text{In}(\text{ABT})$ (**4**) to a solution of 0.5 equivalence of I_2 .

List of Spectra and Tables in Appendix

Figure A.1: $^1\text{H-NMR}$ spectrum in CDCl_3 of $\text{C}_6\text{H}_3\text{Br-2,6-(CH}_2\text{Br)}_2$ (**5**) produced from reaction with ultraviolet light.

Figure A.2: $^1\text{H-NMR}$ spectrum in CDCl_3 of $\text{C}_6\text{H}_3\text{Br-2,6-(CH}_2\text{Br)}_2$ (**5**) from reaction with infrared light.

Figure A.3: $^1\text{H-NMR}$ spectrum in CDCl_3 of $\text{C}_6\text{H}_3\text{Br(CH}_2\text{NMe}_2)_2\text{-2,6}$ (**6**); pincer ligand.

Figure A.4: $^1\text{H-NMR}$ spectrum in CDCl_3 of $(\text{NCN})\text{InCl}_2$ (**7**).

Figure A.5: $^1\text{H-NMR}$ spectrum in DMSO-d_6 of InMe_2Cl (**8**).

Figure A.6: $^1\text{H-NMR}$ spectrum in DMSO-d_6 of $(\text{NCN})\text{InMe}_2$ (**9**).

Figure A.7: $^1\text{H-NMR}$ spectrum in DMSO-d_6 of $(\text{NCN})\text{InMe}(\text{H}_2\text{ABT})$ via hydrocarbon elimination.

Figure A.8: ^1H -NMR spectrum for attempted synthesis of $(\text{NCN})\text{In}(\text{ABT})$ via sodium hydride in DMSO-d_6 .

Figure A.9: ^1H -NMR spectrum of $(\text{NCN})\text{In}(\text{ABT})\cdot\text{LiCl}_2$ (**4**) via butyllithium in DMSO-d_6 .

Figure A.10: ^{13}C -NMR spectrum of $(\text{NCN})\text{In}(\text{ABT})\cdot\text{LiCl}_2$ (**4**) via butyllithium in DMSO-d_6 . **Figure A.11:** FT-IR spectrum of $(\text{NCN})\text{In}(\text{ABT})\cdot\text{LiCl}_2$ (**4**) via butyllithium.

Figure A.12: ^1H -NMR spectrum in DMSO-d_6 of $(\text{NCN})\text{In}(\text{HABT})_2$ (**10**).

Figure A.13: ^{13}C -NMR spectrum in DMSO-d_6 of $(\text{NCN})\text{In}(\text{HABT})_2$ (**10**).

Figure A.14: FT-IR spectrum of $(\text{NCN})\text{In}(\text{HABT})_2$ (**10**).

Figure A.15: ^1H -NMR spectrum in DMSO-d_6 of $[\text{MeIn}(\text{TDT})\text{py}]_2$ (**1**) after the addition of I_2 .

Figure A.16: FT-IR spectrum of $[\text{MeIn}(\text{TDT})\text{py}]_2$ (**1**) after the addition of I_2 .

Figure A.17: ^1H -NMR spectrum in DMSO-d_6 of $(\text{NCN})\text{In}(\text{TDT})$ (**2**) after the addition of I_2 .

Figure A.18: FT-IR spectrum of $(\text{NCN})\text{In}(\text{TDT})$ (**2**) after the addition of I_2 .

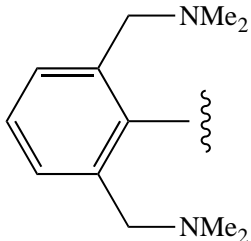
Table A.1: Calculated total energies E (hartree) for geometry-optimized $[\text{MeIn}(\text{ABT})]$ structures and pyridine (py).

Table A.2: Calculated total energies E (hartree) for geometry-optimized neutral and cationic $(\text{NCN})\text{In}(\text{TDT})$ structures and that reduced by iodine, $(\text{NCN})\text{InI}(\text{TDT})$.

Table A.3: Calculated total energies E (hartree) for geometry-optimized $[\text{MeIn}(\text{ABT})]$ structures.

Table A.4: Calculated total energies E (hartree) for geometry-optimized neutral and cationic $(\text{NCN})\text{In}(\text{ABT})$ structures and that reduced by iodine, $(\text{NCN})\text{InI}(\text{ABT})$.

Glossary of Abbreviation and Symbols

Symbol	Definition	Symbol	Definition
Me	Methyl Group (CH ₃)	NBS	<i>N</i> -bromosuccinimide
	Pincer Ligand [(C ₆ H ₃)-2,6-(CH ₂ NMe ₂) ₂]	AIBN	Azobisisobutyronitrile
NCN		TMEDA	Tetramethylethylenediamine
THF	Tetrahydrofuran	In	Indium
Et ₂ O	Diethyl Ether	^t Bu	<i>tert</i> -butyl
CDCl ₃	Deuterated Chloroform	py	Pyridine
M	Molarity (mol/L)	HOMO	Highest Occupied Molecular Orbital
mL	Millilitre	LUMO	Lowest Unoccupied Molecular Orbital
mmol	Millimole		
NMR	Nuclear Magnetic Resonance		
ppm	Parts per million		
J	Coupling constant		
d	Doublet		
t	Triplet		
m	Multiplet		

Abstract

Green Chemistry initiatives have recently been at the forefront of both industrial and academic communities in order to address fundamental scientific challenges of protecting human health and the environment. The Twelve Principles of Green Chemistry, of which catalysis is a primary tenet and the main motivation for this project, has led the path to reduce waste production in the chemical industry. The principle of catalysis states that catalytic reactions necessarily produce less waste than stoichiometric reactions. Traditionally, precious and toxic heavy transition metals such as platinum and palladium have been used as metal centres in catalysts because of their stability, favourable redox properties, and ease of characterization. These concerns prompted this research in finding more environmentally friendly alternatives as metal centres in catalysis, such as main group complexes. Indium is a heavy main group metal that is environmentally benign. It is most stable in the +3 oxidation state and, notably, does not possess other readily accessible oxidation states. To make indium complexes redox-active, so-called “non-innocent” redox-active ligands are being explored. The current work seeks to synthesize a series of redox-active indium catalysts with varied steric bulk about the indium centre and different redox-active ligands. The goals of this study are to first synthesize and structurally characterize organometallic indium compounds with the redox-active ligand 2-aminobenzenethiol, and then test the reactivity of indium complexes with dithiolate ligands using mild oxidizing agents. A third goal is to use DFT methods to rationalize the synthesized complexes in terms of structure, reactivity, bonding motifs, and in interpreting the experimental spectroscopic data.

1. Introduction

Chemistry plays a vital role in multiple aspects of our lives, from the toothpaste we use to brush our teeth to the beds in which we sleep. One aspect of our lives that has been greatly influenced by innovations in chemistry is the medical field. Indeed, diseases that were once understood to be incurable are now routinely cured with antibiotics, antivirals and other targeted therapeutics. The resultant enhancement of our quality of life has been achieved, in part, because of the large number of synthetic therapeutics that have been discovered, increasing the world life expectancy from 65.3 years in 1990 to 71.5 years in 2013.¹ However, the benefits of chemistry come at a cost. The manufacture, use and disposal of synthetic chemicals have had a significant effect on human health and the environment.

The negative effects of modern chemistry are most sadly demonstrated through the world's worst industrial catastrophe—the so-called Bhopal disaster in 1984. The Union Carbide India Limited pesticide plant accidentally and tragically released 42 tons of gaseous methyl isocyanate and hydrogen cyanide to the environment. These heavy compounds were suspended in the atmosphere for long periods of time and remained close to the ground, which ultimately contaminated the drinking water.² While there were many factors that contributed to this tragedy, its magnitude would have been reduced if non-toxic chemicals were used at the facility. The United States Congress subsequently passed legislation (referred to as the *Pollution Prevention Act*, PPA) that would prevent waste at the source by “utilizing a variety of methodologies and techniques to prevent pollution”.³ Clearly, successfully achieving this task would require close collaboration between several areas of science.

1.1 Green Chemistry

With the growing recognition of the need to adopt less toxic and environmentally friendly chemical processes, chemists are increasingly becoming concerned with the amount of waste being released into the environment. One significant outcome of these efforts and concerns is the development of Green Chemistry. The main driving force for

this initiative is the massive amount of hazardous waste produced in the myriad of chemical processes that occur worldwide, an issue that could no longer be ignored. Green Chemistry involves the design of chemical syntheses and processes that are more environmentally friendly, produce less waste, and avoid the use of toxic reagents.⁴ Figure 1 shows the twelve principles of Green Chemistry developed by Paul Anastas and John Warner that act as a guide for purposeful design (**Figure 1**).⁵ It is defined as “the utilization of a set of principles that reduces or eliminates the use or generation of hazardous substances in the design, manufacture and application of chemical products”.⁶

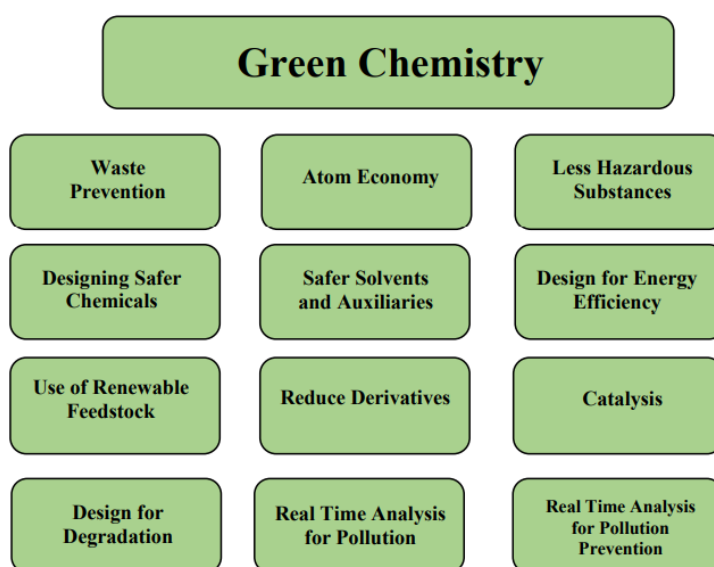


Figure 1: The Twelve Principles of Green Chemistry as proposed by Anastas and Warner.⁵

It is typically not possible to address all twelve principles simultaneously when designing a greener process. One must instead attempt to apply as many principles as possible during the various stages of a synthetic process.⁷ Notably, a number of chemists have changed their chemical design process by linking the concept of Green Chemistry with other metrics, such as the E-factor developed by Roger Sheldon. This metric calculates the amount of waste produced in a traditional chemical processes and also the amount of waste reduction by employing greener techniques.⁸ Since these principles were formulated, Green Chemistry initiatives have been at the forefront of both industrial and academic communities to address fundamental scientific challenges of advancing human health and protecting the environment.⁹

The continuing efforts of industry to reduce waste within existing synthetic routes highlight the effectiveness of the twelve principles of Green Chemistry. Some noteworthy examples on changing perspectives of chemical process design include Pfizer's redesign of the synthesis of sertraline, and the synthesis of polyisobutylene.¹⁰ As the active ingredient in the antidepressant drug; Zoloft, Pfizer applied the principles of Green Chemistry to develop a new synthetic route for sertraline that improved both worker and environmental safety. The original synthesis of sertraline involved the recovery of four solvents (methylene chloride, tetrahydrofuran, toluene and hexane) in a three-step synthesis that was neither cost effective nor energy efficient. Pfizer streamlined the process to a single step that consisted of imine formation of monomethylamine with tetralone, followed by reduction of the imine and resolution of the resultant diastereomer. Notably, this new process provided sertraline in a much higher yield than the original synthetic process. Plus, Pfizer used the benign solvent ethanol for this new process rather than the four solvent cocktail with concomitant solvent recovery it had used originally. This new process showcases the principles of waste prevention, use of safer solvents and maximizing the end product yield.

In another example of how the principles of Green Chemistry positively influenced an industrial process, Soltex Inc. (Synthetic Oils and Lubricants of Texas) in Houston, Texas developed a new synthetic design for polyisobutylene (PIB).¹¹ An isobutylene polymer that contains one double bond, PIB is used in the production of dispersants and detergents for lubricants and gasolines. Importantly, the position of the double bond in PIB changes its reactivity; highly reactive PIB is formed when the double bond is at or near the end of the polymer chain, whereas less reactive PIB is formed when it is at an internal position of the polymer. The process of producing highly reactive PIB has traditionally involved feeding boron trifluoride into a reactor with isobutylene monomer. Boron trifluoride is a toxic liquid polymerization catalyst that requires appropriate handling techniques to avoid exposure and vapour release. The catalyst must also be isolated and neutralised immediately upon completion of the reaction to stop further polymerization. The newly developed process by Soltex Inc. involves a novel solid catalyst that is fixed to

the bed of the reactor system. The stationary form of the solid catalyst facilitates polymerization as the isobutylene monomer is fed into the reactor at a controlled rate. Importantly, the polymer mixture does not require a catalyst separation step or water wash, because the polymer exits the reactor at the same control rate. This process produces high yields of pure product while using low amounts of catalyst and relatively less waste.¹² In an effective catalytic reaction, less reagents are required and in turn leads to less waste or co-product being generated. As one of the primary tenets of the Twelve Principles of Green Chemistry and the main motivation for this project, catalysis has led to reduced waste production in the chemical industry.

1.2 Catalysis

As the ninth principle of Green Chemistry, catalysis refers to the preference for catalyzed reactions that produce less waste than the corresponding stoichiometric reactions.¹¹ Reactions with metal hydrides, oxides, acids or elemental metals produce stoichiometric amounts of inorganic waste, which would be prevented with the use of catalysts. In other words, “catalytic reagents are superior to stoichiometric reagents”.⁷ Because catalysts are regenerated after each catalytic cycle, they can be used several times to form the desired product(s) from the reactant(s). This suggests that less than stoichiometric amounts of reagents will be consumed in a catalyzed reaction, thereby reducing the amount of chemical waste generated. Chemical industries have recognized the economic and environmental benefits provided by catalysts and have applied it to over 90% of all industrial processes.¹³ Of the 12 principles of Green Chemistry, catalysis is the foundational principle that offers numerous benefits including lower energy requirements, catalytic versus stoichiometric amounts of materials, increased selectivity, and the use of less toxic materials. In particular, heterogenous catalysis addresses the goals of Green Chemistry by eliminating the need for separation through distillation or extraction by providing facile separation of product and catalyst.¹⁴

Many synthetic routes currently use precious heavy transition-metals such as platinum, palladium, rhodium, and gold as metal centres in catalysts because of their stability, redox properties, and ease of characterization.¹⁵ Transition metals can easily

change between oxidation states and can facilitate π -bond activation, which allows them to interact with various organic functional groups in selective catalytic reactions. One example of a transition metal catalyst undergoing a redox reaction is shown in **Figure 2**. Wilkinson's rhodium catalyst is used to hydrogenate unsaturated hydrocarbons (olefins) by adding a molecular hydrogen across a carbon double bond in organic compounds. The reaction mechanism involves oxidative addition and reductive elimination steps that change the metal oxidation state. This type of chemistry is made possible because of the favourably redox activity of rhodium as the catalyst.

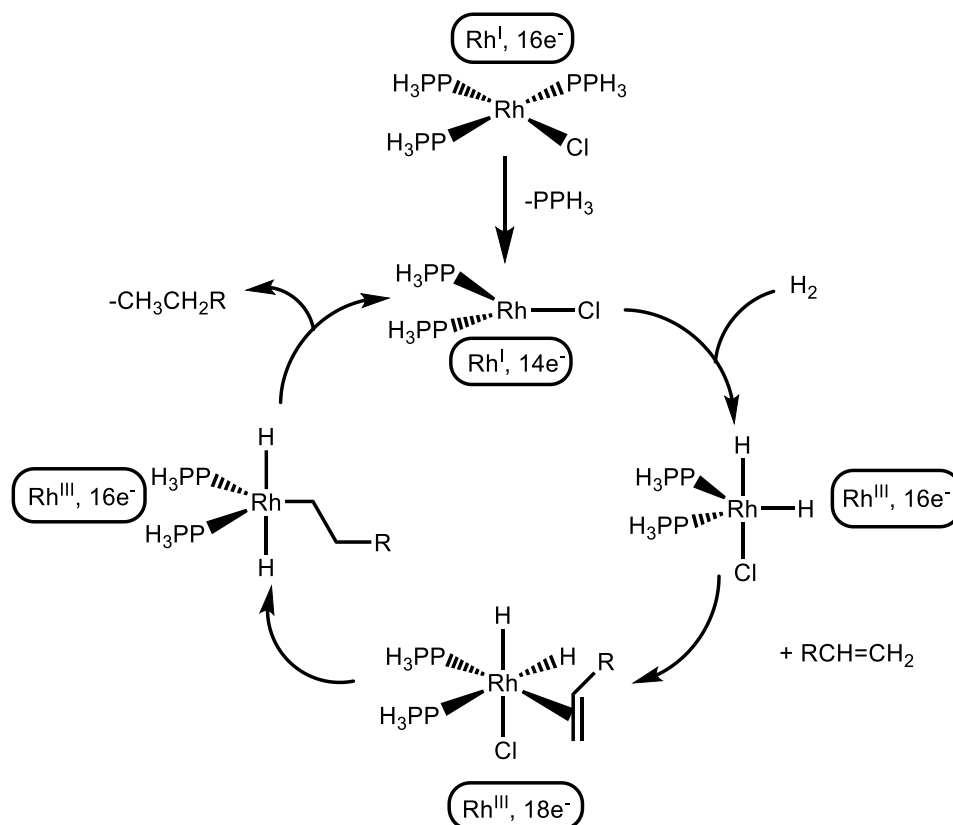


Figure 2: A rhodium-based Wilkinson's catalyst undergoing a redox-active catalytic cycle.¹⁶

Homogeneous catalysis is widely practiced by chemists throughout industry and is often used for the development of early kilo-lab syntheses, which are laboratory settings utilizing large glass vessels to produce kilogram quantities of the material or drug.¹⁷ Palladium-catalysed cross-coupling reactions are essential tools in synthesising carbon-

carbon and carbon-heteroatom bonds, and they have become especially prevalent in agrochemical production routes.¹⁸ One drawback of their use, however, is that palladium-based catalysts require purification after the completion of each catalytic cycle. This increases both the cost and generation of waste for these processes. Plus, transition metals like palladium are at risk of depletion, causing their price to increase and thus significantly increasing the cost of these reactions. Another drawback of palladium is its toxicity, which is especially problematic because it can contaminate the final product.¹⁹ Moreover, if the metal leaches into aquatic environments, it is prone to form nanoparticles and cause toxicity to larvae and adults aquatic organisms.²⁰ These drawbacks are significant for all precious metal catalysts to varying degrees, and have consequently stimulated efforts of this study in finding more environmentally friendly metal centre alternatives in catalysis, such as main group complexes.²¹ An ideal green catalyst would be cheap, stable, able to undergo reversible redox reactions and have a favorable risk-reward profile for human health and the environment.

1.3 Indium complexes as catalysts

Indium (In) is a main group heavy metal and is an attractive choice for use as a green organometallic catalyst. It is distinguished by its low toxicity and its potential as a Lewis acid catalyst in aqueous solution. As a group 13 and a fifth-row element, indium can form bonds using its three valence electrons occupied in $5s$ and $5p$ orbitals, and it can expand its octet to form bonds beyond trivalent species. It exists in oxidation states of +1 and +3, with indium-(III) being the most stable form.²² Indium-(III) is a soft Lewis acid and less reactive than boron-(III) or aluminum-(III), which are often used as effective organometallic catalysts.²³ However, it exhibits higher chemo-selectivity than boron-(III) or aluminium- (III) and can better tolerate organic functional groups such as alcohols or amines.

One of the most widespread uses of indium is in indium tin oxide (ITO), which is the thin-film coating used in many electronic appliances such as flatscreen TVs, touch screen and solar panels. In terms of catalysis, indium has been used as a metal centre in a variety of Lewis acid catalysts. Indium-(III) has an empty p -orbital, which makes it both

an excellent σ - and π -Lewis acid (**Figure 3**). As a σ -Lewis acid, indium-(III) has been used for a variety of reactions including nucleophilic addition, Diels-Alder and Friedel-Crafts reactions. Indium-(III) can also act as an efficient π -Lewis acid when coordinated with unsaturated systems such as alkynes. Indium Lewis acid catalysts have been shown to catalyse the ring-opening polymerization of lactide into poly(lactic) acid, a biodegradable material that is now very popular for 3D printing.²⁴

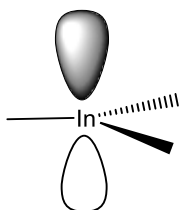


Figure 3: Empty p-orbital on indium (III).

In terms of Green Chemistry, indium has great potential as a green catalyst because it offers low toxicity, an efficient recycling methodology, is relatively cheap, and because it tolerates many different types of functional groups. In addition, indium Lewis acid catalysts are stable in water.^{15,25} Despite these potential advantages, indium is most stable in its +3 oxidation state and does not possess other readily accessible oxidation states.²² Indium itself is therefore not a redox-active metal and cannot undergo redox catalysis. As seen in the next section, however, indium centres can be made to be redox-active with the appropriate choice of ligands.

1.4 Ligands for designing redox-active indium compounds

1.4.1 Redox-active ligands

One approach to making an indium centre redox-active is to attach redox-active non-innocent ligands to the indium centre. The term “non-innocent” implies an ill-defined oxidation state for the metal complex that incorporates redox-active ligands. The inclusion of a redox-active ligand can modify the reactivity of a metal complex in four different ways. Specifically, redox-active ligands can: i) influence the Lewis acidity of the coordinated metals; ii) act as electron reservoirs; iii) form ligand radicals; and iv) participate in radical redox chemistry, in which case the redox-active ligand is also the

substrate of the catalytic reaction.²⁶ Once the redox-active ligands are introduced into the complex they can adopt either a “spectator” or “actor” role. Each role can have a profound effect on the overall reactivity and selectivity of the catalyst (**Figure 4**).²⁷ Redox-active ligands adopt a spectator role during single electron transfer reactions and when the reactivity occurs at the metal centre. By comparison, the ligands play an “actor” role for elementary bond formation in multi-electron catalytic transformations. One advantage of active ligands as electron reservoirs is that the oxidation state of the metal centre remains unchanged while the ligand participates in the electron transfer reactions. In other words, non-innocent ligands attached to a metal centre allow the complex to participate in redox chemistry without forcing the metal centre to adopt unfavourable oxidation states.^{26,28} Therefore, for a metal such as indium whose most stable oxidation state of +3 precludes facile reduction or oxidation, attaching a redox-active ligand to it may facilitate vital multi-electron catalytic transformations without requiring indium to adopt an unfavourable oxidation state.

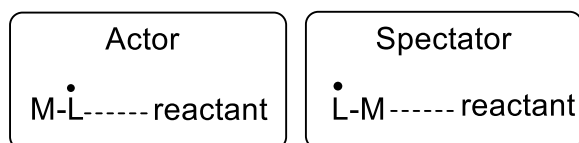


Figure 4: Modes of redox-active ligands: Actor and Spectator, where M is metal and L is ligand.²⁷

The concept of using redox-active ligands for catalytic transformations has been recently explored for indium (III) complexes. One example of a redox-active moiety was shown by Piskunov *et al.* using an (*o*-amidophenolato) indium (III) complex (Figure 5).²⁹ In this study, indium is bonded to an *o*-amidophenolate redox-active ligand (AP), tetramethylethylenediamine (TMEDA) and iodine. The reactivity of the resulting complex was characterized with different oxidizing agents (i.e., diiodine, mercury(II) chloride, tetramethylthiuramedisulphide (TMUDS), and dioxygen). **Figure 5** shows the mild oxidizing agent diiodine (I_2) reacting with (AP)InI(TMEDA) to form a (*o*-iminobenzosemiquinonato)-indium(III) product complex. Although the reaction formally requires oxidation of indium, there is no change in the metal oxidation state as the reaction proceeds via a one-electron oxidation of the amidophenolate ligand. The indium centre therefore maintains its formal 3+ oxidation state throughout the process, which results in

the formation of an additional indium-iodine bond. The complex shown in **Figure 5** has TMEDA coordinating to the indium center in a bidentate fashion, which acts to stabilize the complex.

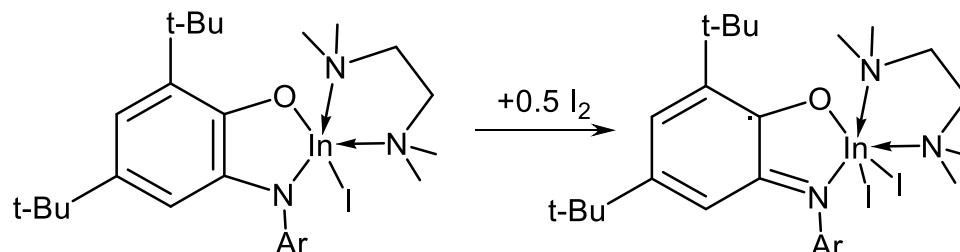


Figure 5: The oxidation of *o*-amidophenolate indium (III) complex (APInI(TMEDA)) with iodine and TMEDA.

Various redox-active ligands have been explored with different main group metals.²⁷ The present work examines the redox-active ligands toluenedithiol (TDT) and *o*-aminobenzenethiol (ABT).

1.4.2 Redox-active toluene-3,4-dithiol and *o*-aminobenzenethiol ligands

Dithiolate ligand metal complexes, whereby the ligand chelates to the metal center in a bidentate fashion, have been known since the late 1940s. Dithiolates are a subcategory of dithiolene ligands in which bidentate sulfur-donor atoms are bonded via an unsaturated carbon-carbon bond, which enhances the chelating effect on the metal. Chauhan *et al.* demonstrated this concept with toluene-3,4-dithiolatoantimony(III) complexes.³⁰ Electron spray ionization mass spectroscopy was used to confirm that the toluene-3,4-dithiolate ligand chelates stronger than xanthate (**Figure 6**). Notably, the increased chelating nature of toluene-3,4-dithiol (TDT) has shown greater antimicrobial activities than free ligands and standard drugs because of its ability to penetrate the cell membrane.

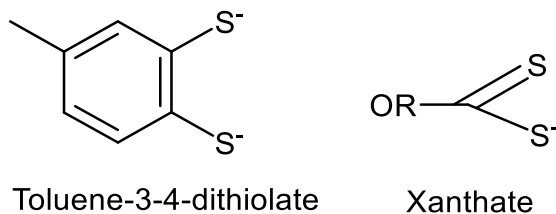


Figure 6: The structures of toluene-3,4-dithiolate (TDT)²⁻ and xanthate.

Unlike toluene-3,4-dithiol, which coordinates metal centres via its two S atoms, *o*-aminobenzenethiolate (ABT)²⁻ ligands coordinate through their N and S atoms. These ligands have increased versatility relative to TDT because of the presence of nitrogen (**Figure 7**). However, the complex is not redox-active if only the sulfur coordinating site, for example, becomes deprotonated and the nitrogen site does not (i.e., ABT¹⁻) or vice versa.

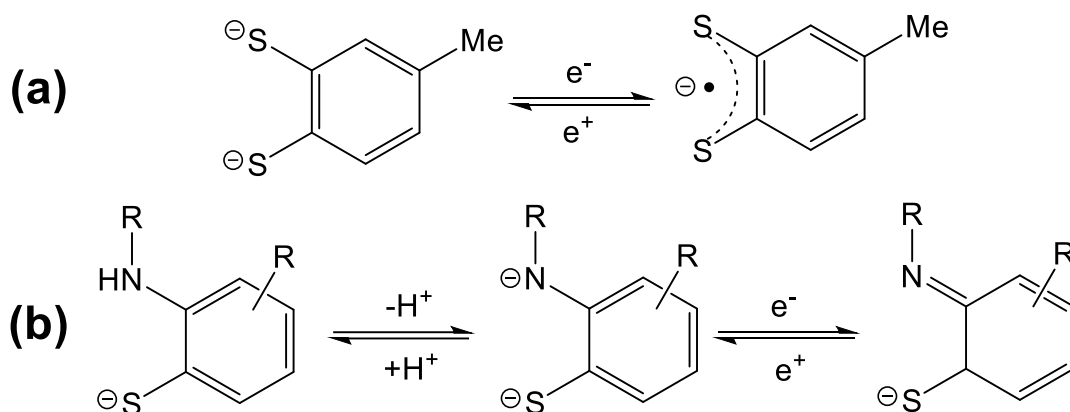


Figure 7: Deprotonation and electronic resonance structures of ligands (a) benzenedithiolate (TDT)²⁻ and (b) *o*-aminobenzenethiolate (ABT)²⁻.

Preliminary work reported that *o*-aminobenzenethiolate complexes of nickel were oxygen-bridged compounds (**Figure 8**, compound A). However, later work showed that the original structure contained *o*-amidobenzenethiolate (ABT)²⁻ ligands and that oxygen-bridging between adjacent Ni centres does not occur (**Figure 8**, compound B). This complete deprotonation of ABT showed that (ABT)²⁻ ligands have the ability to transfer or exchange protons as well as electrons.²⁸ The incorporation of toluene-3,4-dithiolate or *o*-aminobenzenethiolate ligands could potentially provide a pathway for redox chemistry in non-redox-active base metals such as indium.

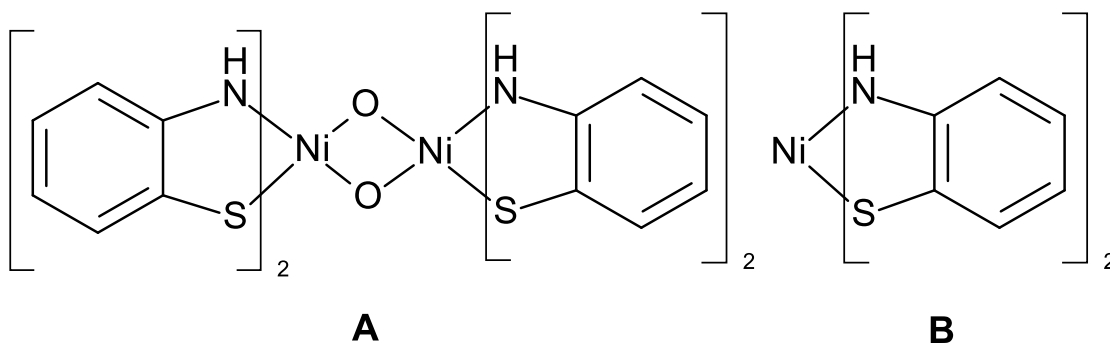


Figure 8: Initially postulated (A) and later confirmed (B) structures of Ni(ABT).

1.4.3 Pincer ligand

To stabilise metal complexes of redox-active dithiolate ligands and indium, a chelating agent that binds tightly to the indium centre must be present. For this reason, ancillary ligands must be carefully chosen when designing redox-active indium complexes, as these ligands can obstruct bond formation between the indium centre and the redox-active ligand. Under certain reaction conditions labile ligands can also easily break and replace the metal-ligand bonds. To mitigate this possibility, the use of pincer ligands becomes important, and they are used for this study (**Figure 9**, bolded). In general, pincer-type ligands limit the coordination sphere of a complex by fixing the donor groups in space in a more predictable manner. A pincer ligand can therefore restrict the structure of a compound more efficiently than labile ligands, because its (amine; cf. **Figure 9**) arms chelate to the metal centre. Another advantage of pincer ligands is that they have demonstrated enhanced chemical and thermal stability, which serve to minimize leaching of the metal during catalytic cycles. These ligands also have the ability to modulate electronic and steric properties of the metal centre, which can be exploited in a variety of applications.³¹ Although several different types of pincer ligands exist, the present work employs (2,6-bis[(dimethylamino)methyl]phenyl), an NCN-type of pincer ligand. The ligand is referred to as NCN ligand because the atoms that coordinate to the metal centre are nitrogen-carbon-nitrogen. NCN can stabilize mononuclear indium compounds through coordination of a pair of amine groups to the metal centre.

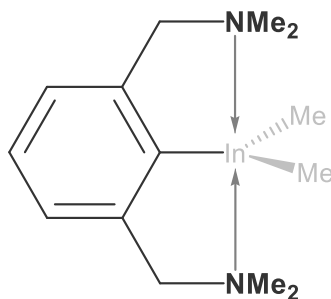


Figure 9: Pincer ligand (NCN, in bolded black) stabilizing an indium-centred molecule [(NCN)InMe₂] by coordinating through its amine groups.

1.5 Computational Chemistry

To provide further insight into the synthesis and reactivity of the indium complexes studied in this work, computational quantum chemistry calculations were performed. Density functional theory (DFT) has experienced increasing use in metal-ligand chemistry because of its low computational cost and reasonable accuracy in predicting molecular properties (i.e., thermodynamics, geometries, etc.).³² Although a large number of density functionals are available, it is crucial to select an appropriate exchange-correlation functional for a particular scientific problem. In fact, several assessments on the accuracy of DFT methods are available in the literature.³³

The B3LYP exchange–correlation functional has been widely used for calculating energies of main-group complexes. B3LYP is popular because of its superior performance in numerous energy assessments of small molecules. Its robust nature has many inorganic chemists continuing to use it for large systems, such as those involving indium, because of its convenience and reasonable accuracy. However, recent work by Nhat *et al.* has shown that the PBE1PBE functional is superior to B3LYP in computing chemical shifts for compounds containing C and H elements.^{34,35} Likewise, recent papers by Tuononen and co-workers showed that the PBE1PBE functional is superior to B3LYP in calculating energies for main group complexes with large metal centres.³⁶ For these reasons, all calculations reported herein use the PBE1PBE exchange–correlation functional (see Appendix B for further details).

1.6 Current study

This thesis is conceived around three pillars. The first pillar examines the synthesis of indium compounds containing redox-active dithiolate ligands. The second is to experimentally assess their redox activity, while the third uses computational chemistry calculations to rationalize observed structures and rationalize the redox activity of the synthesized indium compounds.

1.6.1 Synthesis and characterization of target compounds

One primary goal of this research is to synthesize and structurally characterize several neutral and stable redox-active indium complexes. The stabilities of the indium

complexes will be imparted by the organic substituents (i.e., a methyl group or NCN pincer ligand), and the redox activities will be achieved by incorporating ABT and TDT ligands. **Figure 10** shows the four target redox-active indium complexes of this study. Former student in this lab Alex Stöckli and Michael Mosher synthesised/characterized compounds **1** and **2** and synthesised compound **3**, respectively.³⁷ The current study will focus on synthesising and characterizing (NCN)In(ABT) (**4**) and spectroscopically characterising [MeIn(ABT)(py)]₂ (**3**).

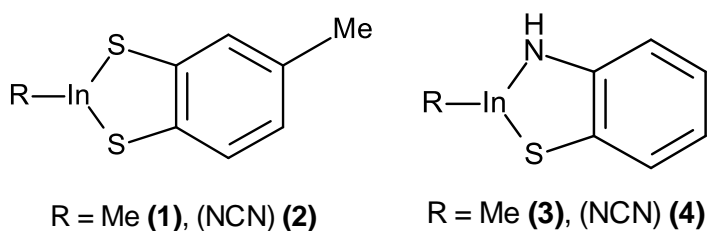


Figure 10: Target indium complexes in this study, where NCN = {2,6-bis[(dimethylamino)methyl]phenyl}, TDT = toluene-3,4-dithiolate and ABT = *o*-amidobenzenethiolate.

All isolated compounds will be fully characterized via elemental analysis, melting point analysis, and FT-IR, FT-Raman, and multinuclear NMR (¹H and ¹³C{¹H}) spectroscopies. The structural motifs of the isolated compounds will be confirmed by X-ray crystallography. Upon successful synthesis of each compound, and consistent with the second pillar around which this thesis is structured, the redox properties of the synthesized indium compounds will be studied. To test the redox properties and assess their suitability for incorporation into catalytic processes, the isolated compounds will be oxidized using I₂.

1.6.2 Computational calculations

The third goal of this research is to perform DFT calculations on all target and isolated complexes using the Gaussian 16 software package. On the basis of literature precedence, the PBE1PBE-GD3BJ/def2-TZVP level of theory has been chosen because of its accuracy in calculating geometries and energies of similar complexes.³⁸ The calculated energies will be used to rationalize reactivity, explore bonding motifs, and interpret spectroscopic data. All calculations were performed in the gas-phase without the use of implicit or explicit solvation. These calculations will also be used to address the relative

energies of the target oxidized compounds and characterize the energy profiles of the oxidation reactions of the indium complexes with oxidizing agents (e.g., I₂)

2. Experimental

2.1 General Methods and Considerations

2.1.1 Instrumentation

Air sensitive reactions were performed under a dinitrogen atmosphere using an Innovative Technology glovebox followed by standard Schlenk line methods. All ¹H and ¹³C{¹H} NMR spectra were collected at 23 °C on a Varian Mercury 200 MHz+ spectrometer. FT-IR spectra were recorded using a Thermo Nicolet diamond ATR spectrometer. FT-Raman spectra were obtained using a Thermo Nicolet NXR 9600 series spectrometer in range of 3900–100 cm⁻¹. Melting points were measured on an Electrothermal MEL-TEMP apparatus. Elemental analysis data were obtained from Guelph Chemical Laboratories Inc. X-ray crystallography was performed by Dr. Jason Masuda at Saint Mary's University.

2.1.2 Reagents

Anhydrous toluene (99.8%), anhydrous tetrahydrofuran (THF) (≥99.9%, inhibitor-free), anhydrous diethyl ether (≥99.7%), anhydrous pyridine (99.8%), and anhydrous hexane (95%) were obtained from Sigma Aldrich and dried with molecular sieves and sodium metal. Indium (III) chloride anhydrous powder (98%), n-butyllithium (1.6 M in hexanes), dimethylamine (2.0 M in THF) N-bromosuccinimide (NBS), K-Selectride (1.0 M in THF), and 2,2'-azobis(2-methylpropionitrile) (AIBN) were obtained from Sigma Aldrich and used as received. 2-Bromo-*m*-xylene and 1,8-dibromonaphthalene were obtained from TCI America and used as received. Trimethyl indium (>99%) was used as received from Strem Chemicals.

2.2 Synthesis of $C_6H_3Br-2,6-(CH_2Br)_2$ (5)

2.2.1 Synthesis of $C_6H_3Br-2,6-(CH_2Br)_2$ (5) using ultraviolet light (UV) ³⁸

2-Bromo-*m*-xylene (24.9 g, 0.135 mmol), N-bromosuccinimide (48.4 g, 0.272 mmol) and a catalytic amount of AIBN were added to CCl_4 (150 mL) to give a white heterogenous solution. This solution was irradiated with ultraviolet light and refluxed for 3 h. The reaction mixture was filtered to remove NBS and the solvent was removed via rotary evaporation. The solid residue was dissolved in boiling hexane (150 mL) and recrystallized at $-15\text{ }^\circ\text{C}$ to form colourless needles. Yield: 19.2 g, 55.9 mmol, 41%. $^1\text{H-NMR}$ ($CDCl_3$, ppm): 7.44–7.13 (m, 3H), 4.65 (s, 4H); (**Figure A.1**).

2.2.2 Synthesis of $C_6H_3Br-2,6-(CH_2Br)_2$ (5) using infrared light (IR) ³⁹

A solution of 2-bromo-*m*-xylene (14.8 g, 80.0 mmol) and N-bromosuccinimide (31.3 g, 177.0 mmol) in methyl acetate (400 mL) was irradiated using a 75W infrared light bulb for 16 h wrapped in aluminium foil. The solvent was removed by rotary evaporation and the product was dissolved in boiling hexane (400 mL). The mixture was hot gravity filtered to remove the succinimide and the solution was left in $-15\text{ }^\circ\text{C}$ to yield white crystals. Yield: 27.6 g, 80.5 mmol, 67%. $^1\text{H-NMR}$ ($CDCl_3$, ppm): 7.44–7.20 (m, 3H), 4.65 (s, 4H); (**Figure A.2**).

2.3 Synthesis of $C_6H_3Br(CH_2NMe_2)_2-2,6$ (6) ⁴⁰

Me_2NH (2 M in THF, 130 mL, 260 mmol) was added to a cooled ($0\text{ }^\circ\text{C}$) homogeneous solution of $C_6H_3Br-2,6-(CH_2Br)_2$ (10.8 g, 31.5 mmol) in Et_2O (300 mL) and stirred for 16 h. The solvent was removed by rotary evaporation to leave a yellowish white solid residue. The residue was treated with NaOH (2.5 M, 100 mL) and extracted using hexane ($2 \times 100\text{ mL}$). The combined hexane layer was dried with anhydrous $MgSO_4$ and filtered. The solvent was removed from the filtrate using rotary evaporation to produce an orange oil. After flash vacuum distillation at $90\text{ }^\circ\text{C}$, the product was obtained as a pale-yellow oil. Yield: 6.46 g, 23.8 mmol, 84%. $^1\text{H-NMR}$ ($CDCl_3$, ppm): 7.39–7.13 (m, 3H), 3.54 (s, 4H), 2.30 (s, 12H); (**Figure A.3**).

2.4 Synthesis of (NCN)InCl₂ (7) ⁴¹

To a solution of (NCN)Br (1.99 g, 7.37 mmol) in THF, n-butyllithium (1.6 M in hexanes, 4.60 mL, 7.37 mmol) was added dropwise to form a dark green solution. The solution turned orange over the course of the 1 h stir. This solution was then added to a solution of InCl₃ (1.60 g, 7.37 mmol) in 30 mL THF at room temperature. This forms a clear brownish red solution and was stirred for 16 h. The solvent was removed to give an orange gel. Toluene (10 mL) was added to the gel and the solution was centrifuged and filtered. The solvent was removed to give a yellow solid, which was washed with hexane (10 mL) to produce a beige powder. Yield: 1.17 g, 3.12 mmol, 42%. ¹H-NMR (CDCl₃, ppm): 7.29 (t, J=76 Hz, 1H), 7.04 (d, J=7.8 Hz, 2H), 3.59 (s, 4H), 2.50 (s, 12H); (**Figure A.4**).

2.5 Synthesis of InMe₂Cl (8) ⁴²

Methylolithium (1.6 M, 25.4 mL, 40.69 mmol) was added to a stirring solution of InCl₃ (4.5 g, 20.35 mmol) in 60 mL of ether in a cold bath. The solution was stirred for 2 days. The solvent was removed under reduced pressure. The product was purified by subliming at 115 °C for 6 h to a 15 °C cold finger to yield white needle-like crystals. Yield: 2.78 g, 1.54 mmol, 76%. ¹H NMR (ppm, DMSO-*d*₆): -0.30 (m, 6H); (**Figure A.5**).

2.6 Synthesis of (NCN)InMe₂ (9) ⁴⁴

n-Butyllithium (1.6 M, 7.0 mL, 11.1 mmol) was added to a solution of (NCN)Br (3.0 g, 11.06 mmol) in hexane (34 mL) at room temperature. This solution was stirred for 1 h, followed by its dropwise addition to a solution of InMe₂Cl (1.99 g, 11.06 mmol) in hexane (20 mL), which was stirred overnight. The mixture was centrifuged and the solution was decanted into a Schlenk vessel. The solvent was removed slowly under reduced pressure on an ice bath. This yielded pale yellow needle-like crystals. Yield: 2.62 g, 8.51 mmol, 77%. ¹H-NMR (CDCl₃, ppm): 7.00 (m, 3H), 3.35 (s, 4H), 2.20 (s, 12H), -0.50 (s, 6H); (**Figure A.6**).

2.7 Attempted synthesis of (NCN)In(ABT) (4)

2.7.1 Attempted synthesis of (NCN)In(ABT) via hydrocarbon elimination

A solution of (NCN)InMe₂ (0.313 g, 0.930 mmol) in 4 mL toluene was warmed to 60 °C in an oil bath. To this warm solution, H₂ABT (0.117 g, 0.93 mmol) in 3 mL toluene was added dropwise for 2 min and the mixture was heated to 86 °C for 20 min to produce a lilac powder. The reaction solution was decanted hot and centrifuged to form a purple solution. While attempting to concentrate the solution, lilac precipitate formed within 10 s. The solution was kept at room temperature for 20 min and the precipitate was collected by filtration and dried. ¹H NMR (ppm, DMSO-*d*₆): 7.17 (6H, m), 6.96 (3H, m), 5.19 (2H, s), 2.22 (5H, s), 2.14 (12H, s), -0.27 (1H, s); (**Figure A.7**).

2.7.2 Attempted synthesis of (NCN)In(ABT) via salt elimination using sodium hydride

To a solution of NaH (0.0890 g, 3.73 mmol) in 7 mL THF, H₂ABT ligand (0.233 g, 1.86 mmol) was added dropwise to form a peach solution. The solution was refluxed for 1 hr in an oil bath. This solution was added dropwise to (NCN)InCl₂ (0.703 g, 1.86 mmol) in 7 mL THF and was stirred overnight. The solution turned peach colour with a shade of white after the overnight stir. It was then filtered and concentrated to 2 mL. The solution was kept at -15 °C overnight to produce a microcrystalline precipitate. ¹H-NMR (DMSO-*d*₆, ppm): 7.16 (m, 4H), 6.79 (m, 3H), 5.59 (s, 1H), 5.01 (s, 1H), 3.45 (m, 4H), 2.15 (d, 12H); (**Figure A.8**)

2.8 Synthesis of (NCN)In(ABT) (4) via salt elimination using butyllithium

Butyllithium (1.6 M, 2.33 mL, 3.73 mmol) was added to a stirring solution of H₂ABT ligand (0.233 g, 1.86 mmol) in 6 mL THF cooled to 90 °C. After the addition was complete, the cold bath was removed, and the bright yellow solution was allowed to warm to room temperature. After 30 min of stirring, (NCN)InCl₂ (0.703 g, 1.86 mmol) in 6 mL THF was added dropwise to the Li₂ABT mixture and stirred overnight. The reaction mixture turned orange-brown with a purple tint. After 16 h, the solution was opaque, but no precipitate formed. The solution was concentrated to 4 mL and a beige powder precipitated. The solution was centrifuged to separate the clear dark reddish-purple solution and the powder precipitate. The solution was decanted and left at -15 °C for 16 h to form

plate-like crystals. Yield: 0.259 g, 0.319 mmol, 32.4%. Elemental Analysis: Calculated: C, 50.7%; H, 6.55%; N, 6.82%. Found: C, 50.45%; H, 6.81%; N, 6.49%. ^1H NMR (ppm, DMSO- d_6): 2.17 (12H, m, (N(CH $_3$) $_2$) $_2$); 3.55 (4H, m, (N(CH $_2$) $_2$) $_2$); 4.56 (1H, m, (ABT-NH)); 6.02 (1H, m, HN-C-CH-CH-CH-CH-C-CS); 6.47 (2H, m, (HN-C-CH-CH-CH-CH-C-CS); 7.01 (3H, m, 3H from NCN ligand); 7.11(1H, m, HN-C-CH-CH-CH-CH-C-CS); (**Figure A.9**). $^{13}\text{C}\{^1\text{H}\}$ (ppm, DMSO- d_6): 25.57 (THF residue), 39.91 (DMSO residue), 45.23 (NCN ligand (N(CH $_3$) $_2$) $_2$), 64.03 ((N(CH $_2$) $_2$) $_2$), 67.5 (THF residue), 111.7 (CS in ABT ligand), 112.8 (C-NH in ABT ligand), 122.8 (HN-CH-CH-CH-CH-CH-CS), 125.8 (HN-CH-CH-CH-CH-CH-CS), 128.2 (HN-CH-CH-CH-CH-CH-CS), 130.4 (HN-CH-CH-CH-CH-CH-CS), 144.6 (carbon atoms on NCN ligand), 154.1 (carbon atoms on NCN ligand); (**Figure A.10**). FT-IR (cm $^{-1}$): 441 (w), 464 (w), 503 (w), 634 (w), 669 (m), 719 (w), 741 (s), 776 (s), 844 (s), 947 (w), 987 (w), 1012 (m), 1030 (m), 1111 (w), 1170 (w), 1203 (w), 1254 (w), 1289 (s), 1321 (w), 1349 (w), 1431 (m), 1463 (m), 1571 (w), 2832 (w), 3395 (w); (**Figure A.11**). Melting point: 162–182 °C.

2.9 Synthesis of (NCN)In(HABT) $_2$ (10)

n-Butyllithium (1.6 M, 1.89 mL, 3.04 mmol) was added to a solution of 2-aminobenzenethiol (0.380 g, 3.04 mmol) in THF (7 mL) at -90 °C. The cold bath was removed after addition and the solution was stirred for 30 min. (NCN)InCl $_2$ (0.573 g, 1.52 mmol) was dissolved in THF (7 mL) and added to the LiHABT mixture. The solution turned from clear yellow to dark brown and was stirred for 16 h. The reaction mixture was then concentrated to 2 mL and a dark brown powder precipitated. The solution was filtered and brownish-yellow block crystals were collected after 1 day at room temperature. Yield: 0.509 g, 0.967 mmol, 63%. Elemental Analysis: Calculated: C, 51.99%; H, 5.64%; N, 10.10%. Found: C, 52.16%; H, 4.78%; N, 10.26%. ^1H NMR (ppm, DMSO- d_6): 2.17 (12H, m, (N(CH $_3$) $_2$) $_2$); 3.32 (4H, s, (N(CH $_2$) $_2$) $_2$); 5.21 (4H, s, (ABT-NH $_2$) $_2$); 6.32 (2H, m, H $_2$ N-CH-CH-CH-CH-CH-CS); 6.71 (4H, d, (H $_2$ N-CH-CH-CH-CH-CH-CS) $_2$); 6.95 (2H, m, H $_2$ N-CH-CH-CH-CH-CS); 7.09 (3H, m, 3H from NCN ligand); (**Figure A.12**). $^{13}\text{C}\{^1\text{H}\}$ (ppm, DMSO- d_6): 39.9 (DMSO residue), 45.4 (NCN ligand (N(CH $_3$) $_2$) $_2$), 64.5 (carbon atoms on NCN ligand + (N(CH $_2$) $_2$) $_2$), 115.3 (CS in ABT ligand), 117.9 (CS in second ABT ligand), 125.6 (CNH $_2$), 126.0 (CNH $_2$ in second ABT ligand), 128.7 (H $_2$ N-CH-CH-CH-CH-

CH-CS)₂, 134.9 (H₂N-CH-CH-CH-CH-CH-CS)₂, 144.3 (H₂N-CH-CH-CH-CH-CH-CS), 147.6 (H₂N-CH-CH-CH-CH-CH-CS); (**Figure A.13**). FT-IR (cm⁻¹): 405 (w), 431 (w), 438 (w), 549 (w), 675 (w), 736 (s), 748 (s), 789 (w), 842 (w), 895 (w), 925 (w), 1010 (m), 1033 (w), 1081 (w), 1157 (w), 1170 (w), 1201 (w), 1251 (w), 1294 (w), 1357 (w), 1442 (s), 1474 (m), 1574 (w), 1600 (m), 2794 (w), 2828 (w), 2863 (w), 2949 (w), 2981 (w), 3053 (w), 3309 (w), 3412 (w); (**Figure A.14**). Melting point: 106–117 °C.

2.10 Reactions of indium complexes 1–4 with I₂ as an oxidizing agent

2.10.1 Addition of (NCN)In(TDT) (2) to a solution of I₂

Under an atmosphere of dinitrogen, I₂ (0.0840 g, 0.330 mmol) was dissolved in 4 mL THF. (NCN)In(TDT) (0.303 g, 0.660 mmol) was dissolved in 3 mL THF and this colourless solution was added dropwise to the purple-black I₂ solution. As the number of drops increased, the colour changed from purple black to dark red to orange to pale yellow and finally to colourless. The reaction was allowed to stir for 30 min and then transferred to a test tube. The solution was concentrated to 2 mL by removing the solvent under pressure to give a darker yellow solution. The solution was stored at -15 °C for 16 h to form clear block crystals of (NCN)In(TDT). ¹H NMR (ppm, DMSO-d₆): 7.23 (4H, m, 3H from NCN ligand + SC-CH-C-CH₃ from TDT); 6.99 (1H, d, 1J_{H-H} = 7.4 Hz, H₃C-CH-CH-CS); 6.52 (1H, d, 1J_{H-H} = 7.4 Hz, Hz, H₃C-CH-CH-CS), 3.50 (4H, d, 1J_{H-H} = 28 Hz, (N(CH₂))₂), 2.22 (3H, m, TDT-CH₃); 2.17 (12H, m, (N(CH₃))₂); (**Figure A.17**). FT-IR (cm⁻¹): 627 (m), 681 (m), 710 (m), 779 (s), 808 (s), 844 (m), 950 (w), 987 (m), 1012 (m), 1033 (m), 1105 (s), 1170 (w), 1204 (w), 1252 (m), 1276 (w), 1296 (w), 1353 (w), 1451 (s), 1577 (w), 2829 (w), 2952 (w); (**Figure A.18**).

2.10.2 Addition of [MeIn(TDT)py]₂ (1) to a solution of I₂

Under dinitrogen atmosphere, I₂ (0.123 g, 0.487 mmol) was dissolved in 3 mL THF. [MeIn(TDT)py]₂ (0.276 g, 0.487 mmol) was measured and dissolved in 4 mL THF. The solution of [MeIn(TDT)py]₂ was added dropwise to a clear colourless stirring solution of I₂. The colour gradually changed from dark purple to blood red to orange to pale yellow and by the last drop the solution turned colourless. After 30 min of stirring, the solution was transferred into a test tube and concentrated to approximately 2 mL. The solution was

stored at -15 °C overnight to form colourless block crystals of [MeIn(TDT)py]₂ in pale yellow solution. ¹H NMR (ppm, DMSO-*d*₆): 8.56 (1H, m, py o-CH); 7.77 (0.5H, m, py p-CH); 7.37 (1H, m, py m-CH); 7.26 (1H, d, ¹J_{Ha-Hb} = 8.2 Hz, H₃C-CH-CH-CS, H_a); 7.23 (1H, d, ¹J_{Hc-Hb} = 1.2 Hz, H₃C-C-CH-CS, H_c); 6.51 (1H, ddd, ¹J_{Hb-Ha} = 8.2 Hz, ¹J_{Hb-Hc} = 2.0 Hz, H₃C-CH-CH-CS, H_b); 2.11 (3H, s, H₃C-C₆H₃S₂); 0.03 (1.5H, s, In-CH₃); -0.21 (1.5H, s, In-CH₃); (**Figure A.15**) FT-IR (cm⁻¹): 412 (m), 419 (m), 429 (w), 441 (w), 446 (w), 478 (w), 506 (w), 547 (m), 624 (s), 681 (s), 697 (s), 752 (m), 816 (s), 874 (m), 1006 (s), 1035 (s), 1068 (s), 1107 (s), 1148 (m), 1213 (m), 1246 (m), 1353 (w), 1378 (w), 1440 (s), 1456 (s), 1483 (w), 1597 (m), 1634 (w), 2288 (w), 2913 (w), 2900–3600 (w); (**Figure A.16**).

2.10.3 Reaction of (NCN)In(TDT) (2) with excess I₂

By analogy with the synthesis described in section 2.10.1, a solution of (NCN)In(TDT) (0.100 g, 0.220 mmol) in 3 mL THF was added dropwise to I₂ (0.551 g, 2.17 mmol) in 4 mL THF. During the addition, the solution colour remained purple black, even after 4 days of stirring. The solution was concentrated under reduced pressure, remained purple and did not yield any crystals.

2.10.4 Addition of [MeIn(ABT)py]₂ (3) to a solution of I₂

By analogy with the synthesis described in section 2.10.1, a solution of [MeIn(ABT)py]₂ (0.0500 g, 0.080 mmol) in 1.5 mL THF was added dropwise to I₂ (0.0191 g, 0.0800 mmol) in 3 mL THF. During the addition, the solution colour gradually changed from dark purple to dark red to darkish orange. No precipitate formed after the solution was left at -15 °C for 24 h.

2.10.5 Addition of (NCN)In(TDT) (4) to a solution of I₂

By analogy with the synthesis described in section 2.10.1, a solution of (NCN)In(ABT) (0.100 g, 0.0800 mmol) in 1.5 mL THF was added dropwise to I₂ (0.010 g, 0.040 mmol) in 3 mL THF. During the addition, the solution changed from light purple to dark blackish purple. The colour intensified but did not change. No precipitate formed after the solution was left at -15 °C for 24 h.

2.10.6 Addition of [MeIn(TDT)py]₂ (1) to four equivalence of I₂

A solution of [MeIn(TDT)py]₂ (0.276 g, 0.490 mmol) in 3 mL THF was added to a solution with one equivalent of I₂ (0.123 g, 0.490 mmol). The colour changed from dark purple to light yellow. Another equivalent of I₂ (0.123 g, 0.490 mmol) was added to the reaction mixture. The purple colour disappeared upon addition and a light-yellow solution was formed after 1 min of addition. A third equivalent of I₂ (0.123 g, 0.490 mmol) was added to the reaction mixture. The purple colour persisted for 20 min before disappearing to form light yellow solution. After the addition of a fourth equivalence of I₂ (0.123 g, 0.490 mmol), the reaction mixture remained dark red in colour and no crystals or precipitate was formed after 24 h at -15 °C.

2.11 Computational methods

Density functional theory (DFT) calculations were performed using Gaussian 16 Revision C.01 at the PBE1PBE- GD3BJ/def2-TZVP level of theory for all atoms except In and iodine, for which Stuttgart electron core pseudo-potentials (SDD) were employed. Structures obtained by X-ray crystallography were used as starting points in geometry optimizations when possible. All other structures were geometry-optimized and structural parameters for input files were adapted from crystal structure data. Frequency calculations were performed on all structures to verify minima with no imaginary frequencies were obtained. Dispersion corrections were included throughout using the D3 empirical correction from Grimme with Becke-Johnson dampening (GD3BJ). All energies reported herein are the sum of the total gas-phase electronic energies plus enthalpic thermal corrections at 298 K.

3. Results and Discussion

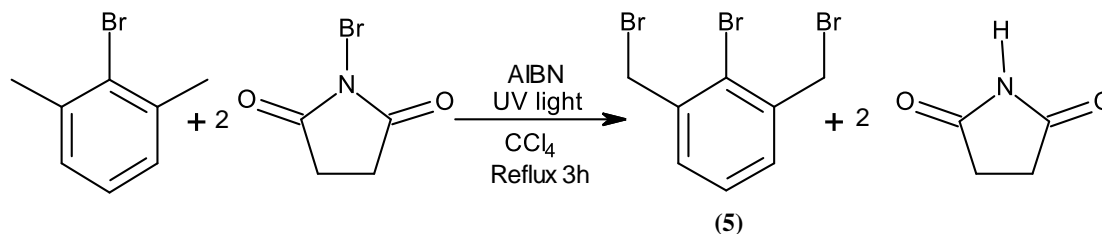
General Synthesis

3.1 Synthesis of C₆H₃Br-2,6-(CH₂Br)₂ (5)

3.1.1 Synthesis of C₆H₃Br-2,6-(CH₂Br)₂ (5) using UV light

Initially, the synthesis of C₆H₃Br-2,6-(CH₂Br)₂ was adapted from a literature procedure that required 2-bromo-*m*-xylene and NBS (*N*-bromosuccinimide) as the primary

starting materials and AIBN as the catalyst.⁴⁵ UV light was a necessary requirement because the heat source and wavelength from the UV light initiated free-radical bromination (**Scheme 1**). However, this procedure resulted in poor yields (26-41%) and incomplete reaction of the starting material. The desired product (**5**) was recrystallized with hexane and the unreacted starting material remained in solution.

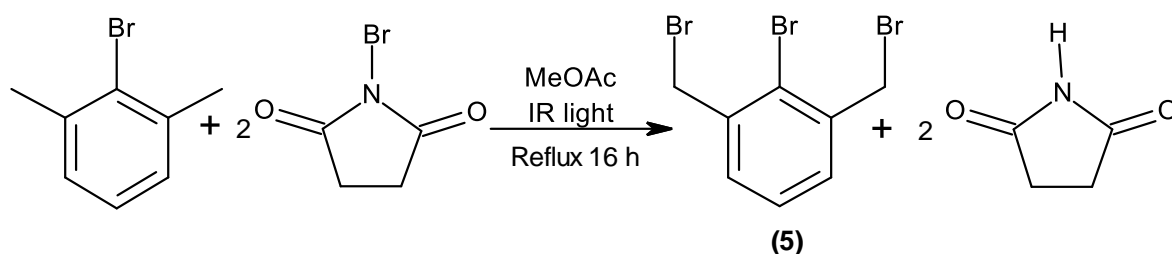


Scheme 1: Synthesis of $C_6H_3Br-2,6-(CH_2Br)_2$ (**5**) from 2-bromo-*m*-xylene and NBS using UV light and AIBN to initiate the radical reaction with CCl_4 as the solvent.

3.1.2 Synthesis of $C_6H_3Br-2,6-(CH_2Br)_2$ (**5**) using infrared light (IR)

While the previous synthesis of $C_6H_3Br-2,6-(CH_2Br)_2$ (**5**) using UV light was successful, it involved using the environmentally harmful solvent CCl_4 . Fatal poisoning in humans has been documented with ingestion of as little as 1 oz. of CCl_4 .⁴⁶ Studies have demonstrated the degradation of CCl_4 in groundwater, and provided evidence for long-term negative effects in marine life.⁴⁷ An alternative synthetic method was therefore developed that does not involve the use of chlorinated solvents (**Scheme 2**).

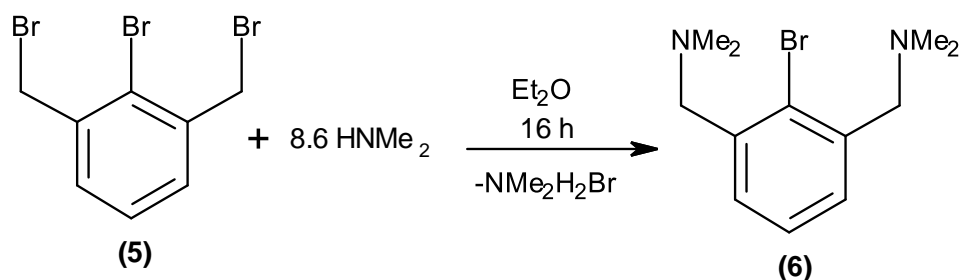
Aluminium foil was used to wrap the IR source around the round bottom flask. This was required to trap the heat produced around the round bottom flask to elevate it to reflux temperatures. The initial reaction mixture produces a white slurry. After 16 h, the reaction mixture turned into a pale-yellow solution, methyl acetate was removed, and the brownish-orange solid precipitate was extracted in 200 mL of hexane and hot gravity filtrated. This resulted in colourless, needle-like crystals at 64–68% yield in the first extraction.



Scheme 2: Synthesis of $C_6H_3Br-2,6-(CH_2Br)_2$ (**5**) from 2-bromo-*m*-xylene and NBS using IR light with methyl acetate as the solvent.

3.2 Synthesis of (NCN)Br (**6**)

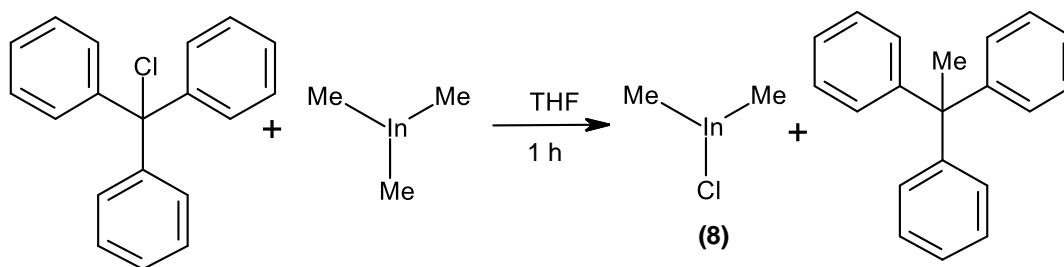
The primary starting materials for synthesising (NCN)Br (**6**) are the tribromo *m*-xylene compound (**5**) and 8.6 equivalents of dimethylamine, which are dissolved in diethyl ether (**Scheme 3**). The reaction formed a cloudy white solution after 16 h with stirring. The solvent was removed by rotary evaporation to give a pale-yellow solid residue, which was treated with NaOH and hexane. After extraction, the resulting oil was purified by flash distillation at 90–110 °C under dynamic vacuum. The yields improved as the reaction was scaled up, ranging from 55–86%.



Scheme 3: Synthesis of (NCN)Br (**6**) from $C_6H_3Br-2,6-(CH_2Br)_2$ and dimethyl amine.

3.3 Synthesis of InMe₂Cl (**8**)

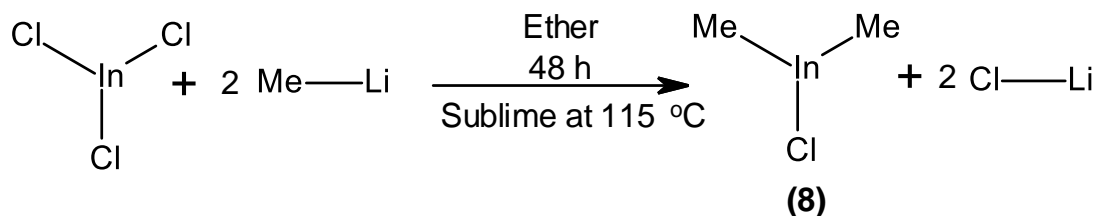
The initial synthesis of InMe₂Cl was adapted from Mukherjee *et al.* and involved the dropwise addition of trityl chloride (a clear, colourless solution) to Me₃In in THF (**Scheme 4**).⁴⁸ The solution turned bright yellow after the addition. The solution was stirred for 1 h, and the solvent was removed under reduced pressure. The yellow solid residue was extracted with pentane and washed with toluene to remove the aromatic impurity (1,1,1-triphenylmethane), which was followed by a wash with hexane to removed toluene from the mixture. This process resulted a white solid powder (72%) and its purity was confirmed by ¹H-NMR spectroscopy.



Scheme 4: Synthesis of InMe_2Cl from trityl chloride and trimethyl indium.

Although the previous synthesis was successful with a moderate yield, trityl chloride as the starting material is an expensive investment for one-time use. Additionally, the 1,1,1-triphenylmethane by-product is highly toxic to the environment. Indeed, its material safety data sheet demonstrates that it is very toxic to aquatic organisms and may have long-term effects in the aquatic environment. Studies have also shown that 1,1,1-triphenylmethane in Acid Blue 1 can be destroyed by chlorination at levels used in normal waterworks.⁴⁹ Therefore, the need for a new synthetic procedure is necessary. Coincidentally, a literature procedure which involved the use of InCl_3 and 2 equivalence of methyl-lithium was found (**Scheme 5**).

This procedure involved the addition of InCl_3 and methyl lithium in ether, which formed a white slurry solution and was stirred for 48 h. The solvent was removed under reduced pressure and a cold finger was added to the Schlenk vessel. The white reaction mixture was sublimed at $115\text{ }^\circ\text{C}$ at 8.8×10^{-2} mm Hg vacuum, giving a colourless crystalline product in 75% yield.



Scheme 5: Synthesis of InMe_2Cl with indium trichloride and methyl lithium.

When the methyl lithium was replaced with methyl magnesium bromide, the yield increased to 94% (**Scheme 6**). Grignard reagents such as methyl magnesium halides are

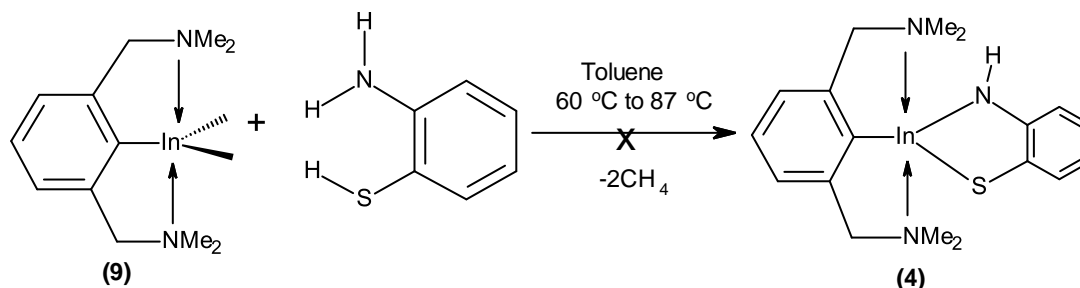
3.5 Attempted synthesis of (NCN)In(ABT) (4)

3.5.1 Attempted synthesis of (NCN)In(ABT) (4) via hydrocarbon elimination

Multiple attempts were made to synthesize (NCN)In(ABT) using a hydrocarbon elimination reaction of (NCN)InMe₂ and H₂ABT. Initial attempts involved the addition of the starting materials in toluene and refluxed for 3 h, which produced a lilac powder. ¹H-NMR spectroscopy of the lilac powder showed that the deprotonation process did not occur on the H₂ABT nitrogen atom. Therefore, the same reaction was performed at reflux temperature for 4.5 h and 16 h, but this still did not deprotonate the amine.

The next attempt involved refluxing the reaction mixture for 3 h and decanting the reaction solution while it was still hot, leaving behind the reaction precipitate. Unfortunately, both amine hydrogen atoms were still attached, as confirmed by ¹H-NMR spectroscopy.

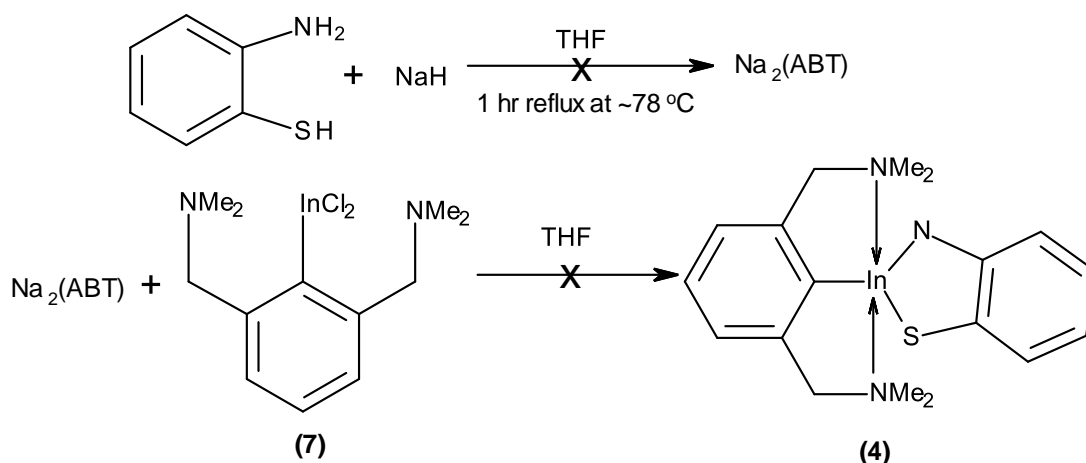
In a subsequent hydrocarbon elimination reaction, a solution of **9** in toluene was warmed at 60 °C in an oil bath (**Scheme 8**). To this warm solution, H₂ABT in toluene was added dropwise for 2 min and the mixture was heated to 86 °C for 20 min to produce a lilac solution and powder precipitate. The reaction solution was decanted while hot. While attempting to concentrate the solution, lilac precipitate started forming within 10 s. The solution was kept at room temperature for 20 min and the precipitate was collected and dried. Unfortunately, ¹H-NMR spectroscopy showed that the target product was not produced; this line of investigation was therefore abandoned.



Scheme 8: Attempted synthesis of (NCN)In(ABT) via hydrocarbon elimination.

3.5.2 Attempted synthesis of (NCN)In(ABT) (4) via salt elimination using sodium hydride

A second experimental approach involved salt elimination using sodium hydride to make the target compound (NCN)In(ABT) (4). H₂ABT was added dropwise to a solution of NaH in THF, forming a peach-coloured solution (**Scheme 9**). As it was previously determined that performing this reaction at room temperature did not afford Na₂ABT, this solution was heated at reflux for 1 h in an oil bath. The solution was then added dropwise to (NCN)InCl₂ in THF and stirred overnight. The solution, which had turned peach colour with a shade of white, was then filtered and concentrated to 2 mL. This solution was kept in the freezer overnight to produce microcrystalline precipitate in a caramel-like solution and consistency. Once again ¹H-NMR spectroscopy showed that the amine proton was not removed with this attempt.

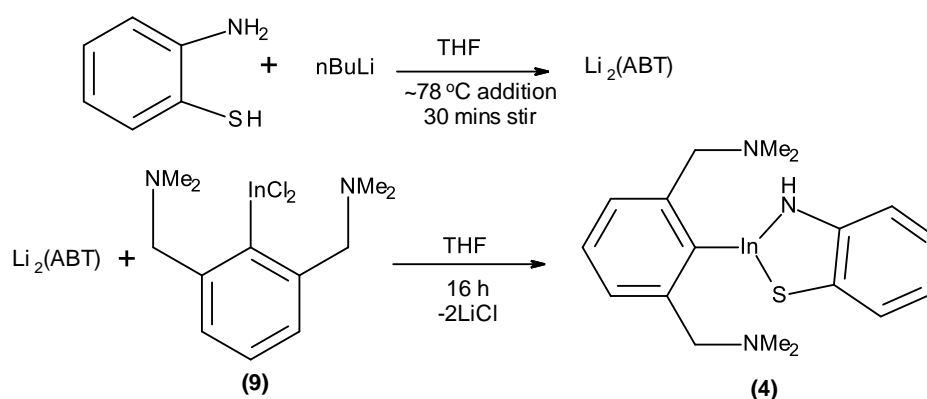


Scheme 9: Attempted synthesis of (NCN)In(ABT) via salt elimination using sodium hydride.

3.6 Synthesis of (NCN)In(ABT) (4) and accidental synthesis of (NCN)In(HABT)₂ (10) via salt elimination using n-butyllithium

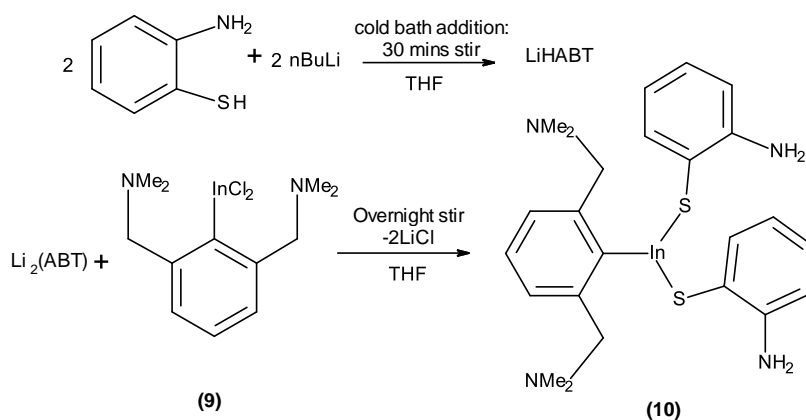
A third approach to synthesize (NCN)In(ABT) used n-butyllithium instead of NaH to deprotonate H₂ABT. The first attempt of this synthesis involved addition of n-butyllithium to a stirring solution of H₂ABT in THF in a cold ethanol bath (**Scheme 10**). After addition, the cold bath was removed and the solution was allowed to warm to room temperature, while the colour gradually changed from light yellow to orange to dark orange and ended

in dark brown. After 30 min of stirring, a solution of (NCN)InCl₂ in THF was added dropwise to a Li₂ABT mixture and stirred overnight. The resulting solution was opaque but no precipitate formed. The solution was pumped dry and the product was redissolved in a small amount of THF. It was then left at -15 °C overnight and block crystals formed in a purple solution. The ¹H-NMR spectrum of the crystals showed that the amine proton was removed and the resulting crystals were sent for X-ray analysis. The results confirmed that while the target molecule (NCN)In(ABT) (**4**) was not synthesised, the novel compound (NCN)In(HABT)₂ (**10**) was synthesized, where two HABT ligands were attached through the deprotonated sulphur while both protons on the nitrogen atoms remain (**Figure 11**).



Scheme 10: Synthesis of (NCN)In(ABT) via salt elimination using butyllithium.

Compound **10** was subsequently synthesized via the reaction of two equivalents of both n-butyllithium and H₂ABT to afford LiHABT, followed by reaction with one equivalent of (NCN)InCl₂ (**Scheme 11**).



Scheme 11: Synthesis of (NCN)In(HABT)₂ via salt elimination using butyllithium and two equivalence of ABT.

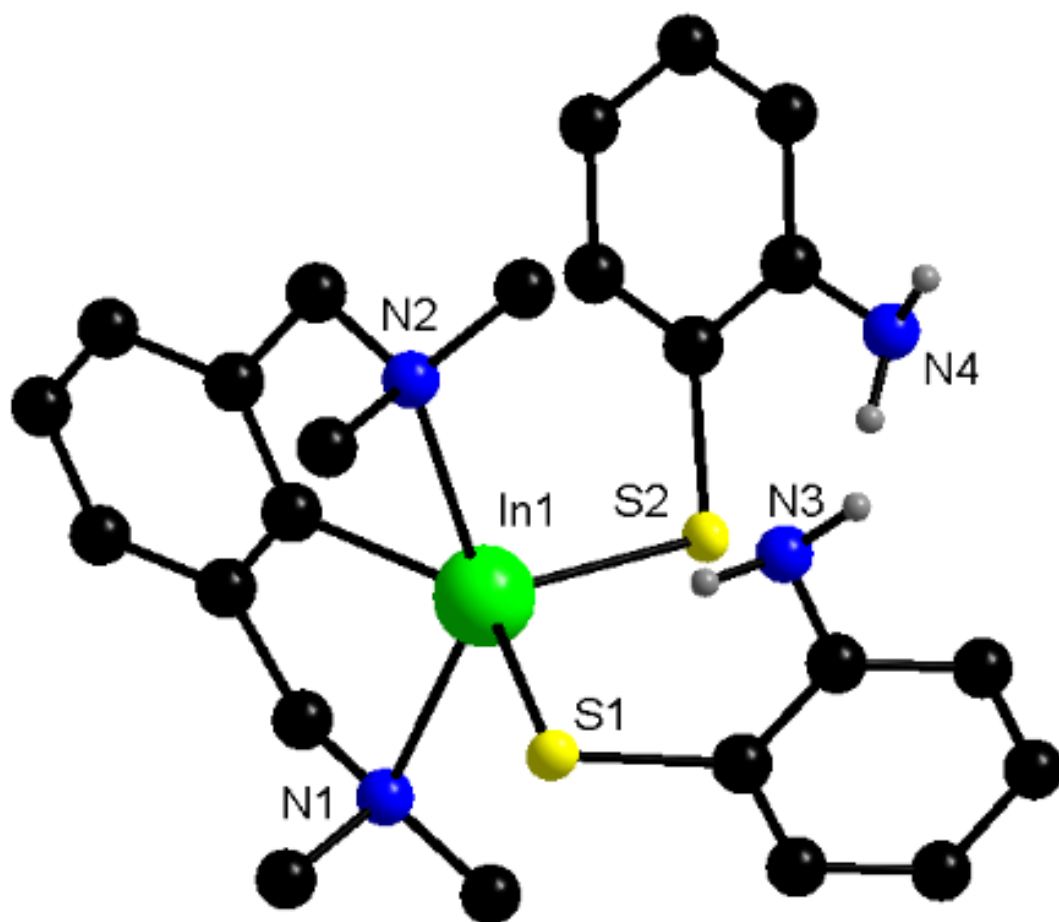


Figure 11: X-ray crystal structure of **10** (30% probability ellipsoids). Except for N-H, hydrogen atoms are omitted for clarity. Selected bond distances (Å) and angles (°): In1–N1 = 2.527(2), In–N2 = 2.557(2), In1–C1 = 2.138(3), In1–S1 = 2.4468(8), In1–S2 = 2.4487(8), C1–In1–S1 = 137.96(7), C1–In1–S2 = 114.77(7), S1–In1–S2 = 107.07(2), N1–In1–N2 = 143.07(7).

The structure of (NCN)In(HABT)₂ (**10**, **Figure 11**) shows a monomeric compound and a distorted trigonal bipyramidal bonding environment for indium. The NCN carbon atom and two HABT sulfur atoms occupy equatorial sites [C1–In1–S1 = 137.96(7)°, C1–In1–S2 = 114.77(7)°, S1–In1–S2 = 107.07(2)°], whereas the two NCN amine nitrogen atoms occupy axial sites [N1–In1–N2 = 143.07(7)°].

To achieve the target indium complex **4**, the reaction outlined in **Scheme 10** was attempted a second time after checking whether THF contained any residual water. After stirring overnight, the solution was concentrated. The solution precipitated a dark brown powder which was filtered and then left at room temperature for 1 d to afford brownish-yellow plate-like crystals. This was different from the block yellow crystals of **10**, and ^1H -NMR spectroscopy showed that the amine proton was removed. The resulting crystals were sent for X-ray analysis. **Figure 12** shows the X-ray crystal structure of **4**, confirming its successful synthesis.

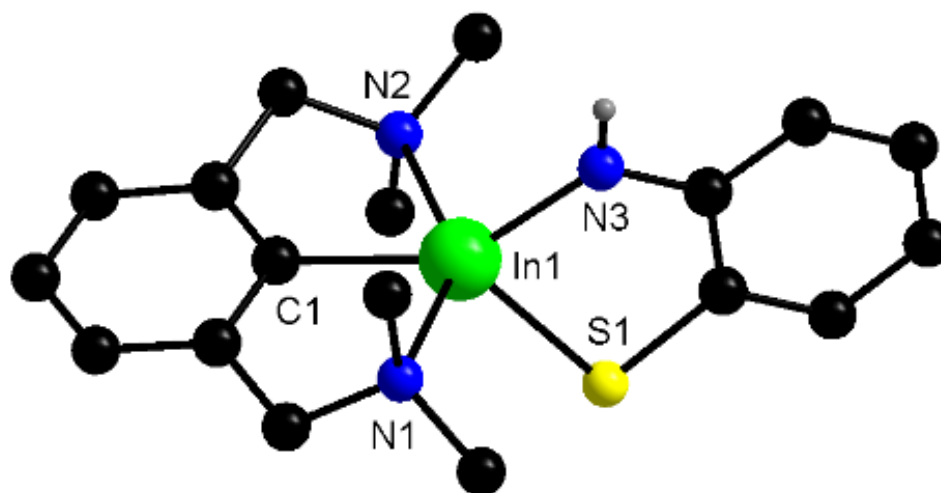


Figure 12: X-ray crystal structure of **4** (30% probability ellipsoids). Except for N-H, hydrogen atoms are omitted for clarity. Selected bond distances (\AA) and angles ($^\circ$): In1-C1 = 2.1169(9), In1-S1 = 2.4459(4), In1-N1 = 2.5101(9), In1-N2 = 2.538(1), In1-N3 = 2.062(1), C1-In1-S1 = 132.62(3), C1-In1-N3 = 142.24(4), S1-In1-N3 = 85.13(3), N1-In1-N2 = 148.07(3).

The structure of (NCN)In(ABT) (**4**) shows a monomeric compound and a distorted trigonal bipyramidal bonding environment for indium. The NCN carbon atom and ABT nitrogen and sulfur atoms occupy equatorial sites [$\text{C1-In1-S1} = 132.62(3)^\circ$, $\text{C1-In1-N3} = 142.24(4)^\circ$, $\text{S1-In1-N3} = 85.13(3)^\circ$], whereas the two NCN amine nitrogen atoms occupy axial sites [$\text{N1-In1-N2} = 148.07(3)^\circ$].

Further analysis of the crystal structure of **4** shows that the (NCN)In(ABT) complex co-crystallised with half an equivalent of (THF)₂Li(μ-Cl)Li(THF)₂ (**Figure 13**). Here, four THF molecules solvate the lithium atoms of an LiCl dimer.

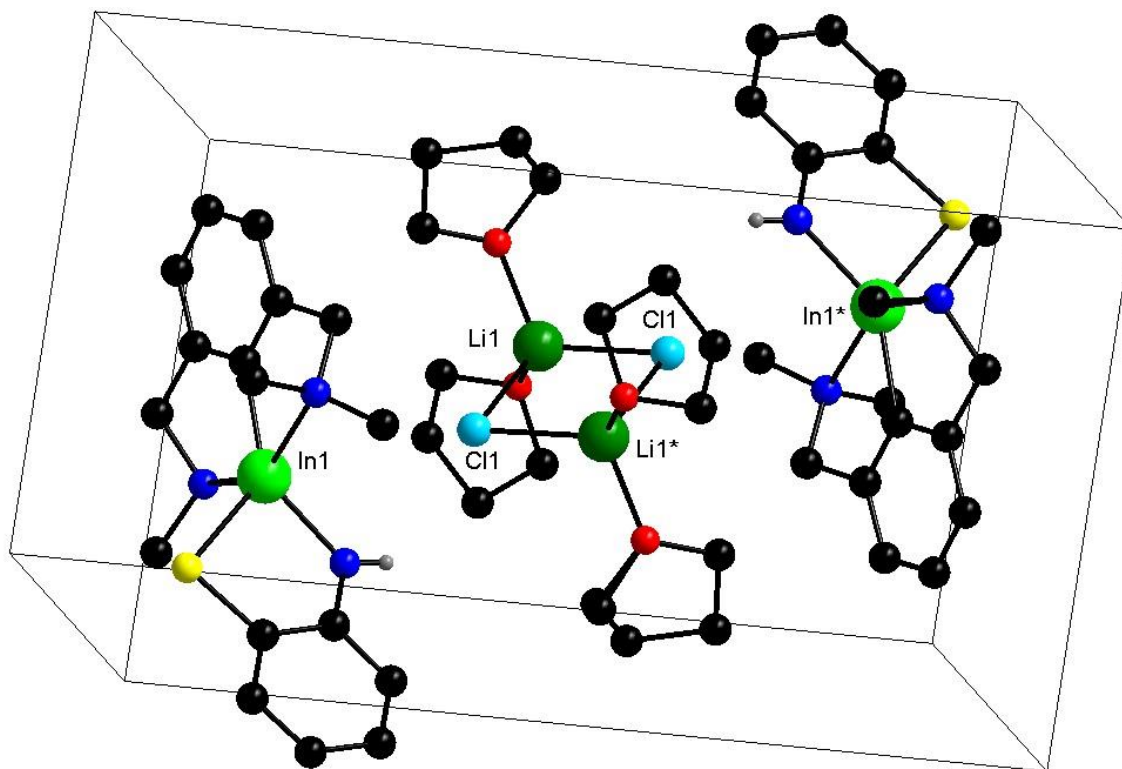


Figure 13: X-ray crystal structure of **4** (30% probability ellipsoids) co-crystallised with LiCl and THF. Except for N-H, hydrogen atoms are omitted for clarity.

Reactivity and Theoretical Calculations

3.7 [MeIn(TDT)py]₂ (**1**)

3.7.1 Structure of [MeIn(TDT)py]₂ (**1**)

DFT calculations were performed to provide insight into the preference for the observed dimeric form of [MeIn(TDT)py]₂. The X-ray crystal structure of complex **1** along with its geometry-optimized structure are shown in **Figure 14**. The X-ray structure of **1** shows a dimeric species via strong intermolecular In1---S1* interactions. Indium adopts a distorted trigonal bipyramidal bonding environment; it is bonded to a methyl carbon atom (C1) and two sulfur atoms, one from the chelating TDT ligand (S2) and one from the bridging TDT ligand (S1*). The bond angle between the equatorial atoms ranges from 106–

133°. In the axial sites, indium is bonded to a pyridine nitrogen atom (N1) and a sulfur atom (S1) from the chelating TDT ligand. The intermolecular In1–S1* bond distance [2.524(1) Å] is shorter than the axial In–S1 bond distance to the chelating TDT ligand [2.740(1) Å], suggesting a very strongly bonded dimer.

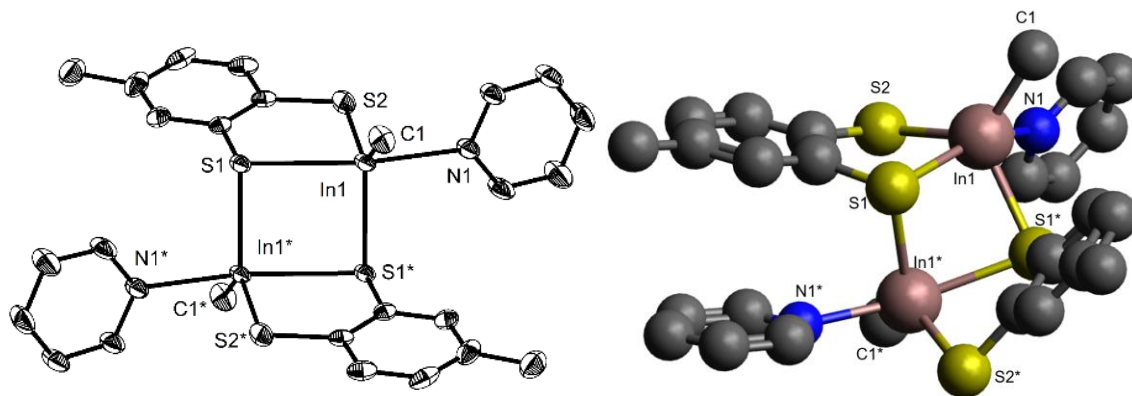


Figure 14: X-ray crystal (left, 30% probability ellipsoids) and geometry-optimized (right) structures of [MeIn(TDT)(py)]₂ (**1**). Hydrogen atoms are omitted for clarity.

Table 1 shows a comparison of selected experimental and calculated data of complex **1**. As seen, there is overall very good agreement between the calculated values and the X-ray diffraction data.

Table 1: Comparison of experimental and calculated bond distances (Å) and bond angles (°) of [MeIn(TDT)(py)]₂ (**1**).

		X-ray crystal structure	Geometry-optimized structure
Bond distances	In1–S1	2.740(1)	2.635
	In1–S2	2.453(1)	2.471
	In1–C1	2.146(4)	2.145
	In1–N1	2.408(3)	2.367
	In1–S1*	2.525(1)	2.546
Bond angles	C1–In1–S1	97.06(11)	108.5
	C1–In1–S2	133.69(11)	127.3
	S2–In1–S1	106.89(3)	82.3
	N1–In1–S1*	91.95(7)	153.6

3.7.2 Dimerization of [MeIn(TDT)py]₂ (**1**)

The initial attempts of synthesizing MeIn(TDT)py]₂ involved adding a 1:1 ratio of trimethylindium and H₂(TDT) in toluene. This resulted in yellow-tinted powders of

MeIn(TDT) that did not crystallise. When four equivalents of pyridine were added to the reaction mixture, however, white block crystals did form. This suggests that pyridine was necessary for crystallisation to occur. It was hypothesised that two equivalents of pyridine would coordinate to the indium centre to give the monomeric complex (**11**, **Figure 15**). As seen in the crystal structure (**Figure 14**), however, the molecule is dimeric and only one pyridine ligand coordinates to each indium centre (**1**). This raises the question of why the binuclear mono-pyridine structure (**1**) crystallises instead of the mononuclear bis-pyridine structure (**11**).

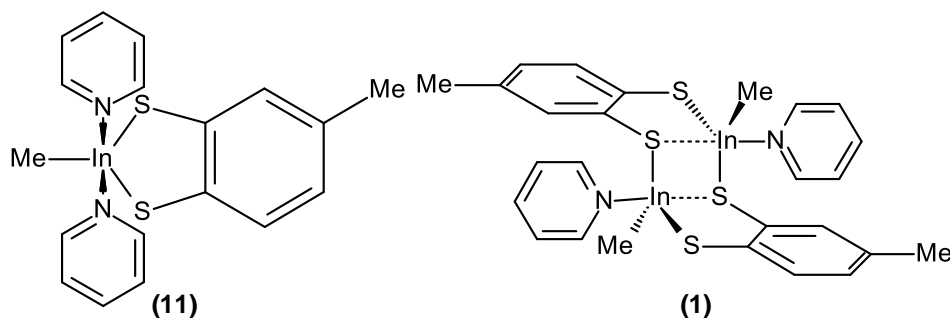
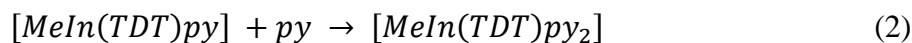
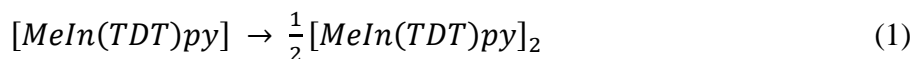


Figure 15: Chemical structures of mononuclear bis-pyridine [MeIn(TDT)py₂] (**11**) and binuclear mono-pyridine [MeIn(TDT)py]₂ (**1**).

To address this question and provide insight into the preference for the observed binuclear mono-pyridine structure (**1**), DFT calculations were performed. The energies associated with the formation of these structure can be calculated using Eqn. (1) and (2).



The total energies of the structures for Equations 1 and 2 are reported in **Table A.1** in Appendix B. Equation 1 has a net reaction energy of $-57.9 \text{ kJ mol}^{-1}$, suggesting an exothermic reaction and that, all things equal, formation of this complex is favourable. Although the calculated reaction energy for Equation 2 is also exothermic ($-51.4 \text{ kJ mol}^{-1}$) for formation of mono-nuclear bis-pyridine adduct (**11**, **Figure 16**), it is higher in energy than that for Equation 1. These calculations support the observation that [MeIn(TDT)(py)₂] (**1**) is the preferred form of the complex in the presence of four equivalents of pyridine.

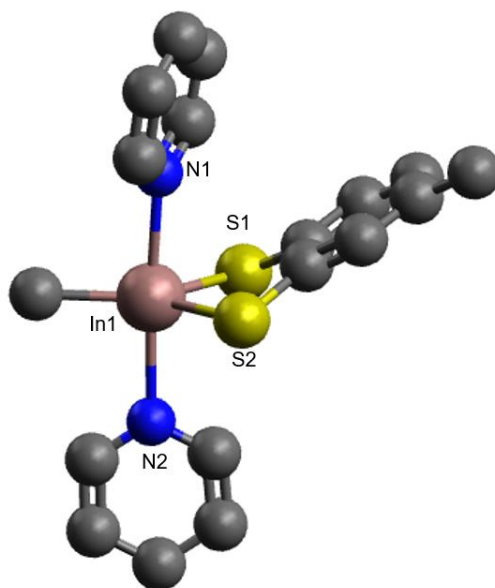


Figure 16: Calculated structure of $[\text{MeIn}(\text{TDT})(\text{py})_2]$ (**11**). Hydrogen atoms are omitted for clarity.

Dimerization of TDT complexes is not uncommon. Previous literature work has shown to observe the same with transition metals. One such distinct examples is $[\text{Fe}(\text{TDT})_2]_2[\text{Bu}_4\text{N}]_2$, which forms a dimer in a distorted square-planar structure.⁵⁰

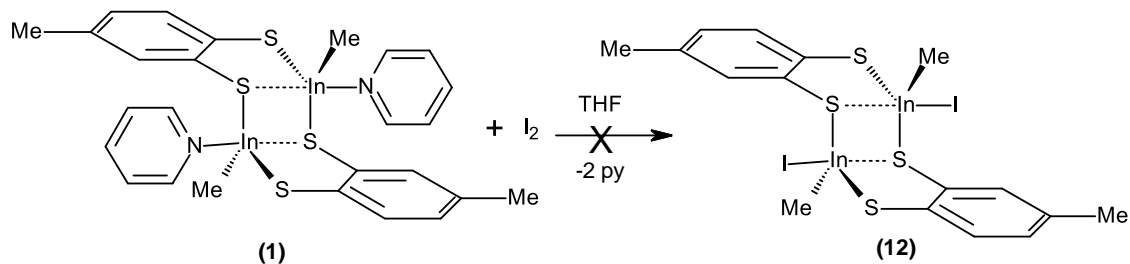
3.7.3 Reactivity of $[\text{MeIn}(\text{TDT})\text{py}]_2$ (**1**) with a mild oxidizing agent

3.7.3.1 Reaction of $[\text{MeIn}(\text{TDT})(\text{py})]_2$ (**1**) with one equivalent of I_2

The study by Piskunov *et al.* demonstrated the concept of using redox-active ligands for catalytic transformations with indium(III) complexes, first introduced in section 1.4.1.²⁹ They showed a mild oxidizing agent diiodine (I_2) reacting with $(\text{AP})\text{InI}(\text{TMEDA})$ to give an (*o*-iminobenzosemiquinonato)-indium(III) product complex. The complex shown in **Figure 5** has TMEDA coordinating to the indium center in a bidentate fashion, which presumably stabilizes the complex.

To test the reactivity of **1**, the complex was similarly reacted with one equivalent of I_2 . The colour of the diiodine solution changed as the solution of **1** was added (**Scheme 12**). The colour changed gradually from dark purple to blood red to orange to pale yellow and

by the last drop of the solution of **1**, the reaction mixture turned colourless (**Figure 17**). The reaction was stirred for 30 min and then transferred to a test tube. The solution was concentrated by removing solvent under pressure and gave a darker yellow solution. The solution was stored at $-15\text{ }^{\circ}\text{C}$ overnight to form colourless block crystals in a pale-yellow solution. The product was determined to be the starting material ($[\text{MeIn}(\text{TDT})\text{py}]_2$) by $^1\text{H-NMR}$ (**Figure A.15**) and FT-IR (**Figure A.16**) analyses.



Scheme 12: Addition of **1** to a solution of I_2 .

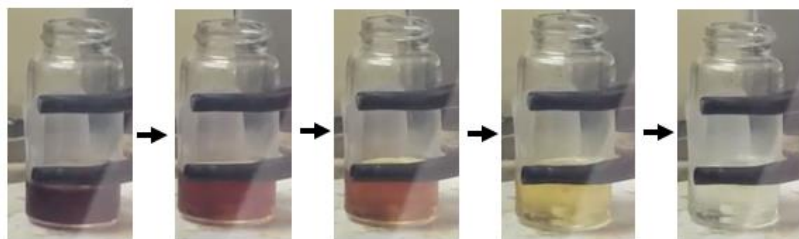


Figure 17: Colour change during the addition of $[\text{MeIn}(\text{TDT})\text{py}]_2$ to a solution of I_2 .

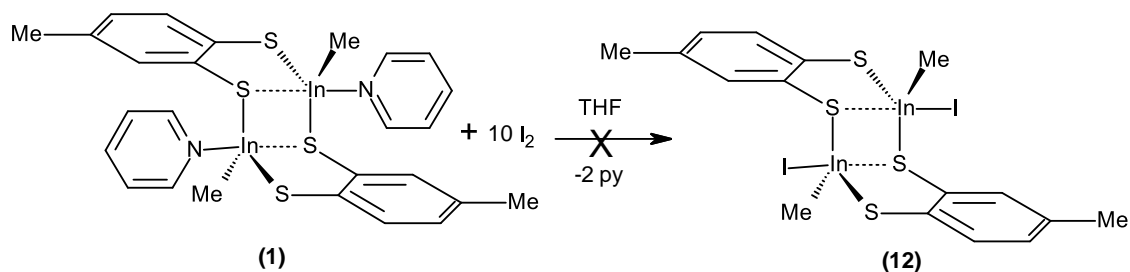
To understand this reaction further, a different solvent was used to observe if the reactivity differed. When the reaction was performed in toluene, no colour change was observed. Since compound **1** is very poorly soluble in toluene, this indicates that the reactivity of **1** is dependent on the solubility of the complex.

Since the diiodine solution was discoloured, presumably via the reduction of iodine to iodide, and the neutral indium complex **1** was recovered from the reaction, it was hypothesised that the reaction could be catalytic.

3.7.3.2 Reaction of $[\text{MeIn}(\text{TDT})\text{py}]_2$ (**1**) with excess I_2

A solution of **1** was added dropwise to a solution of 10 molar equivalents of I_2 in THF (**Scheme 13**). The purple black solution remained unchanged after 4 days of stirring. The

solution was concentrated but did not yield any precipitate, suggesting that the indium compound did not catalyse the reduction of diiodine.

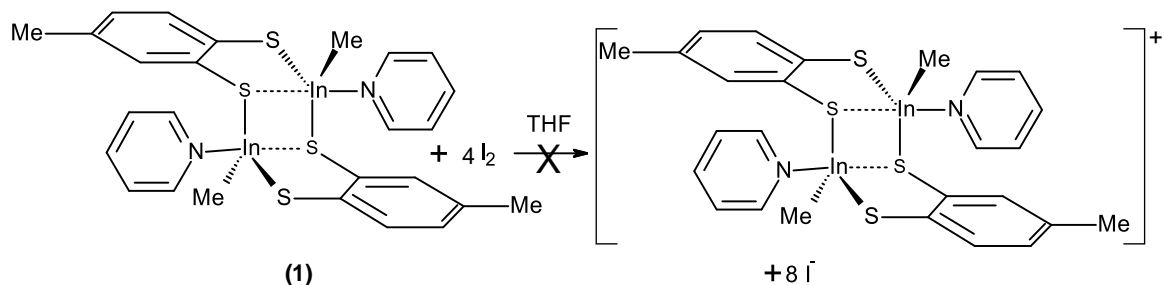


Scheme 13: Addition of a catalytic amount of $[\text{MeIn}(\text{TDT})\text{py}]_2$ to a solution I_2 did not cause reduction of diiodine.

The next set of experiments were carried out to determine the number of equivalents of diiodine with which compound **1** would cause reduction of diiodine.

3.7.3.3 Reaction of $[\text{MeIn}(\text{TDT})\text{py}]_2$ (**1**) with four equivalents of I_2

In this set of experiments, multiple solutions containing one equivalent of diiodine were individually added to a solution of compound **1** until the colour of the diiodine persisted, indicating no further reaction (**Scheme 14**). During the addition of the first and second equivalents of diiodine, the purple colour disappeared quickly and the solution turned yellow. During addition of the third equivalent, however, disappearance of the purple colour became much slower, suggesting the reaction was near an endpoint or equilibrium. Addition of the fourth equivalent resulted in no reaction and the purple diiodine colour persisted, even after 24 h of continuous stirring.



Scheme 14: Attempted addition of 4 equivalence of I_2 to a solution of $[\text{MeIn}(\text{TDT})\text{py}]_2$.

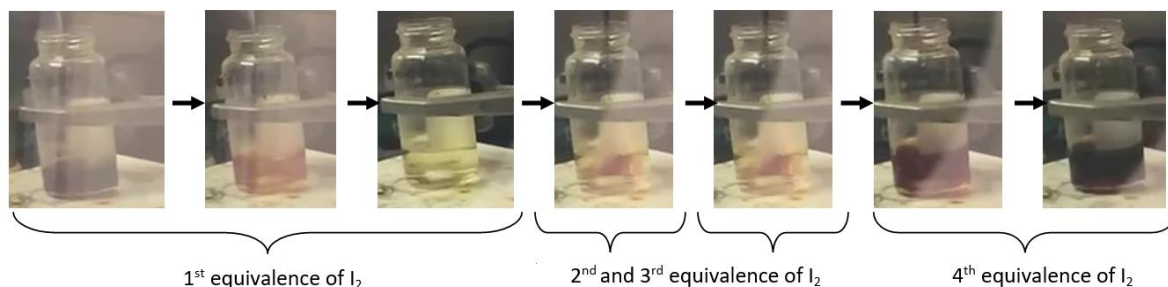


Figure 18: Colour change during the sequential addition of iodine to $[\text{MeIn}(\text{TDT})\text{py}]_2$.

3.7.4 Theoretical calculations on $[\text{MeIn}(\text{TDT})\text{py}]_2$ (**1**)

As seen in Figure 18, a colour change occurs following the addition of complex **1** to a solution of I_2 , suggesting that I_2 may be oxidizing complex **1**. However, a material in which the iodine atom forms a complex with **1** was not isolated. To provide insight into why compound **12** was not formed from this reaction, DFT calculations were performed.

The HOMO (Highest Occupied Molecular Orbital) of **1** show that the largest electron densities are primarily located on the TDT ligand. This confirms that oxidation of **1** should involve oxidation of the redox-active TDT ligand (**Figure 19**).

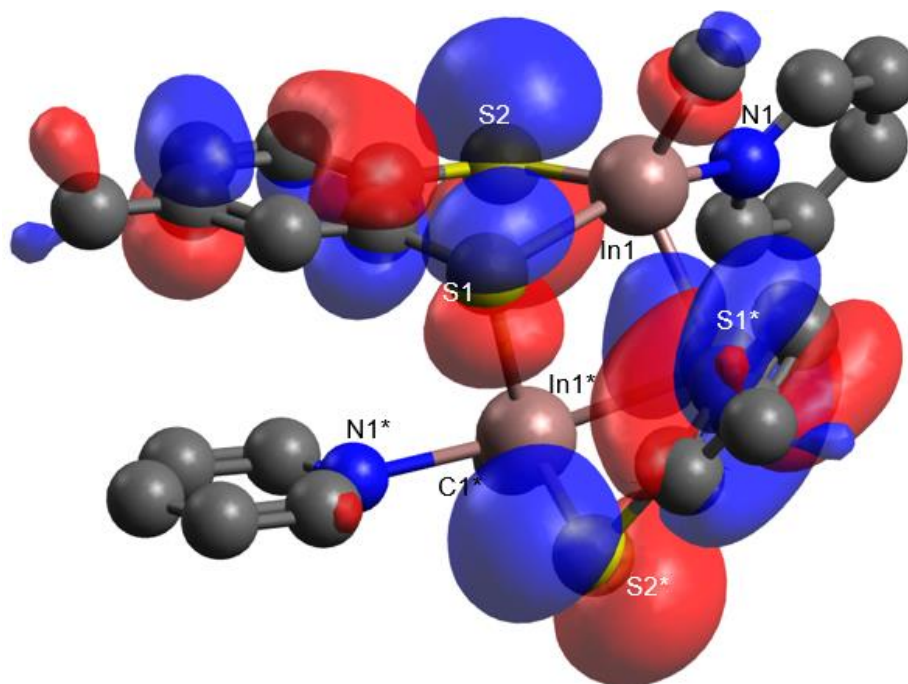


Figure 19: HOMO of complex **1**.

Geometry optimization of the possible product **12** formed from the oxidation of **1** by diiodine (**Scheme 13**) shows that it is higher in energy by 1242326 kJ mol⁻¹ compared with **1** (**Table A.1**). Further, the geometry-optimized structure shows that the oxidized TDT ligands dimerize to form a disulfide bond. Each TDT moiety of the disulfide remains chelated to an indium center, but now does so through a terminal thiolate sulfur of one TDT group and the disulfide sulfur of the second TDT ligand (**Figure 20**). The S1*---S2 bond distance in the geometry-optimized structure is 2.160 Å. One important property of a disulfide bond is the S-S bond distance. Disulfide bonds are usually ~2.05 Å, and in complex **12** it is 2.160 Å, which is close to the literature value.⁵¹

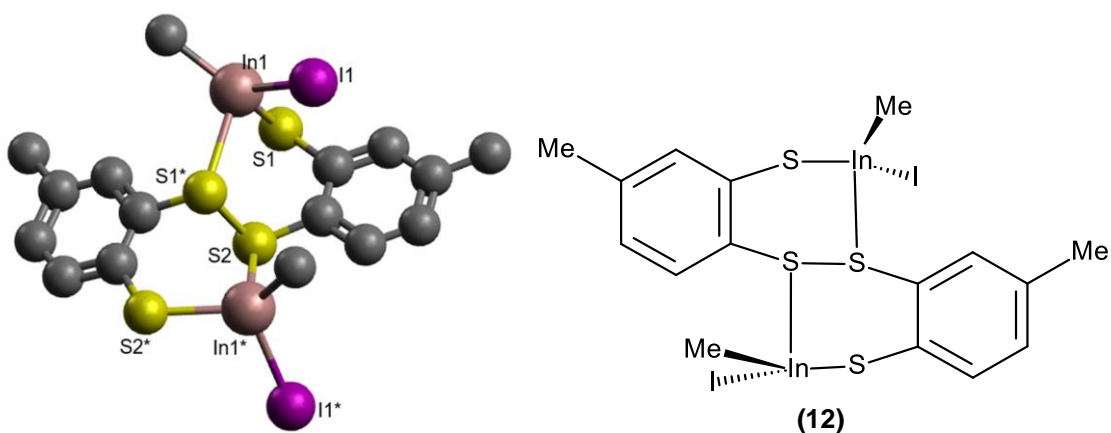
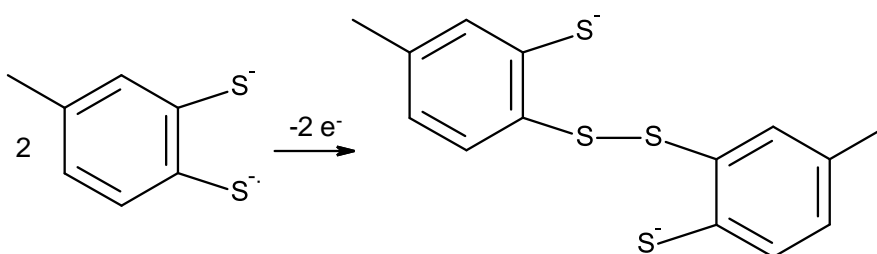


Figure 20: Geometry-optimized structure and the chemical structure of **12**. Hydrogen atoms are omitted for clarity.

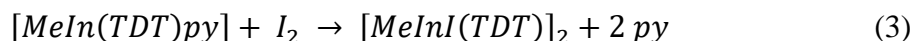


Scheme 15: Electron oxidation of TDT to form a dimer linked through the terminal sulfur atoms.

Scheme 15 shows a potential route for the formation of complex **12**. Oxidation of two TDT ligands could lead to S-centered radicals on each ligand, which could dimerize

to form a disulfide bond. The indium moiety could then subsequently bond to TDT dimer via the sulfur atoms of the ligands.

The expected energy associated with the reaction between complex **1** and I_2 can be calculated using Eqn. (3).



The reaction energy of Eqn 3 is calculated to be endothermic by 63.2 kJ mol^{-1} , suggesting that the formation of **12** is unlikely in the absence of other inputs (such as heating) to the reaction.

3.8 (NCN)In(TDT) (**2**)

3.8.1 Structure of (NCN)In(TDT) (**2**)

The structure of (NCN)In(TDT) (**2**, **Figure 21**) shows the indium center chelated by the tridentate pincer ligand and a bidentate (TDT)²⁻ ligand. The indium centre is in a distorted trigonal bipyramidal bonding environment, similar to complex **1** (**Figure 14**). It is bonded to a carbon atom (C1) from the NCN ligand and two sulfur atoms (S1 and S2) from the chelating TDT ligand. The bond angle between the equatorial atoms ranges from $131\text{--}136^\circ$. In the axial sites, indium is bonded to both the nitrogen atoms from the NCN ligand [$N1\text{--}In1\text{--}N2 = 148.53(8)^\circ$].

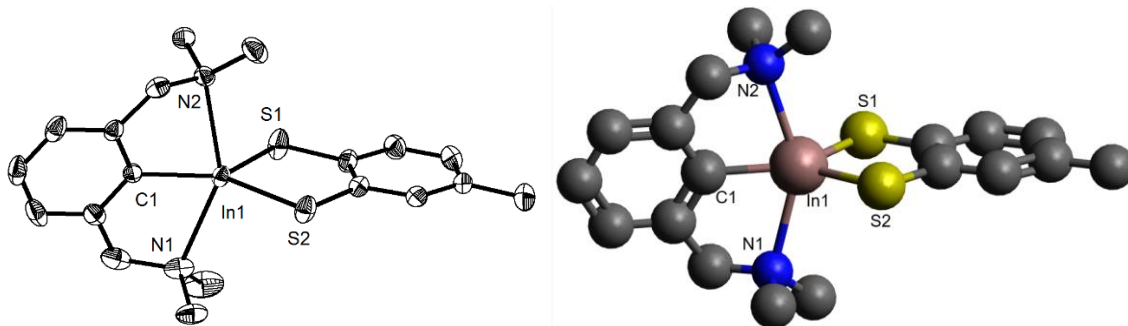


Figure 21: X-ray crystal (left, 30% probability ellipsoids) and geometry-optimized (right) structures of (NCN)In(TDT) (**2**). Hydrogen atoms are omitted for clarity.

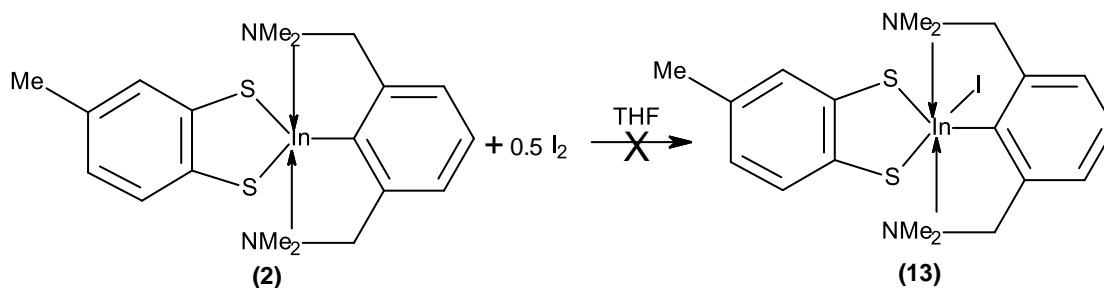
As seen in Table 2, good agreement for selected bond distances and bond angles is found between the X-ray crystal structure of (NCN)In(TDT) **2** and its calculated structure.

Table 2: Comparison of bond distances (Å) and bond angles (°) of X-ray crystal structure and geometry-optimized structure of (NCN)In(TDT) (**2**).

		X-ray crystal structure	Geometry-optimized structure
Bond distances	In1–C1	2.115(2)	2.114
	In1–S1	2.427(1)	2.401
	In1–S2	2.416(1)	2.403
	In1–N1	2.486(2)	2.491
	In1–N2	2.544(2)	2.490
Bond angles	C1–In1–S1	136.71(6)	133.5
	C1–In1–S2	131.45(7)	133.5
	S1–In1–S2	91.72(3)	93.2
	N1–In1–N2	148.53(8)	148.3

3.8.2 Reaction of (NCN)In(TDT) (**2**) with I₂

Complex **2** was reacted with half of an equivalent of I₂ to test its reactivity. As observed with complex **1** (Figure 17), the colour of the diiodine solution gradually changed as the solution of **2** was added: from purple black to dark red to orange to pale yellow and by the last drop the solution turned colourless. The reaction was allowed to stir for 30 min before it was transferred to a test tube. The solution was concentrated by removing solvent under pressure to give a dark yellow solution. The solution was stored at -15 °C overnight to form colourless block crystals. The product was determined to be the starting material (NCN)In(TDT) (**2**) by ¹H-NMR (Figure A.17) and FT-IR (Figure A.18) analyses.



Scheme 16: Addition of **2** to half an equivalence of I₂ solution.

3.8.3 Theoretical calculations on $(NCN)In(TDT)$ (**2**)

3.8.3.1 Frontier orbitals of $(NCN)In(TDT)$ (**2**) and $[(NCN)In(TDT)]^{J+}$

DFT calculations were performed to provide insight into why compound **13** was not isolated from the reaction of complex **2** with diiodine. A colour change occurs following the addition of complex **2** to a solution of half equivalence of I_2 , suggesting that I_2 reacted with complex **2**. However, the iodine atom does not attach to the In center. Understanding the electronic density of complex **2** can provide insight into where the reaction occurs. Graphically, the electron density surface also serves as a canvas upon which electronic properties of the molecule can be displayed. The HOMO (mapped onto the electron density) can provide an indicator for the effect of adsorption on a metal.⁵² The HOMO of complex **2** shows that the largest electron densities are primarily located on the TDT ligand; therefore, the oxidation reaction must have occurred there (**Figure 22**).

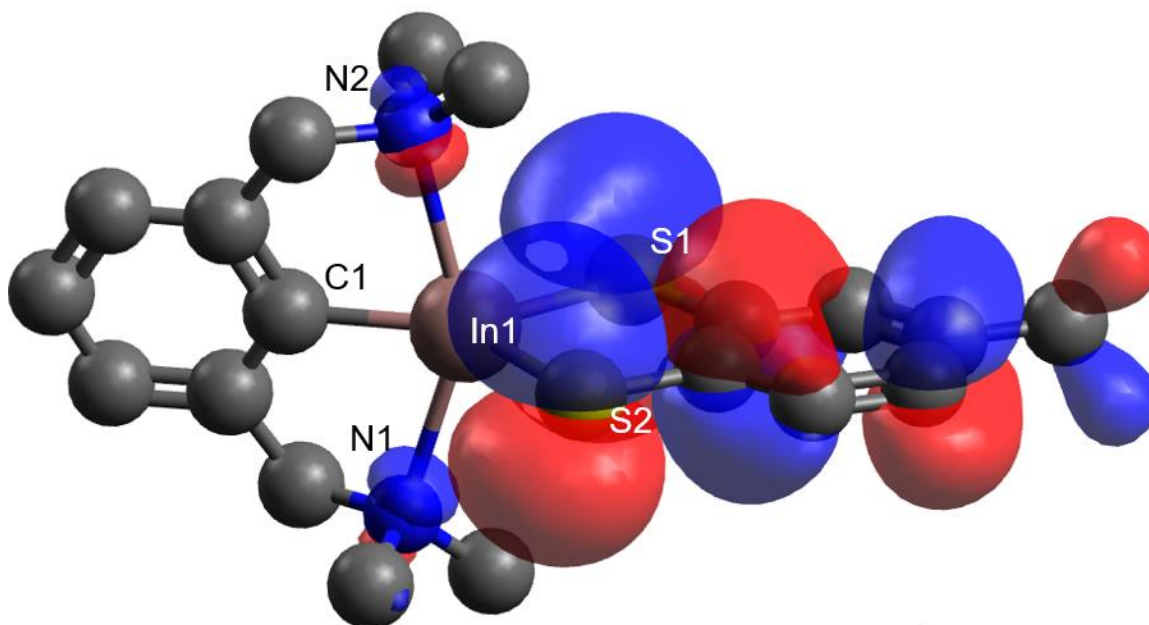


Figure 22: HOMO of complex **2**.

If oxidation does occur, then the molecule must lose an electron and form a radical cation. Cation radicals are species which are formed from neutral molecules by the removal of a single electron. If one electron is removed from complex **2** then the resulting species will have a positive charge and a unit of spin density. The HOMO of the radical cation of **2** is shown in **Figure 23**.

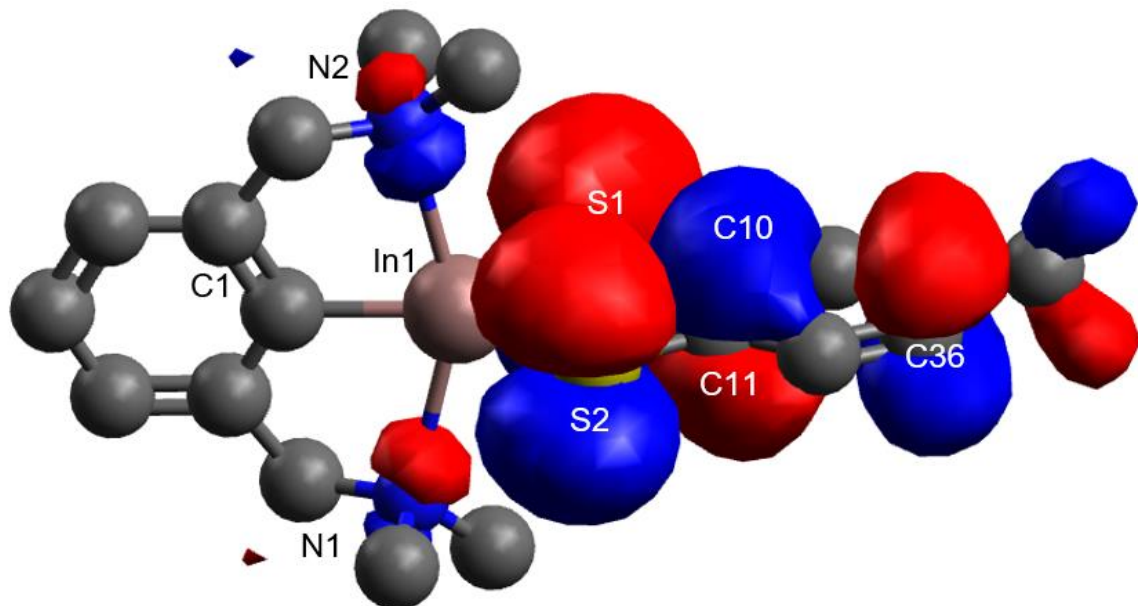


Figure 23: HOMO of the cation radical of complex **2**.

The HOMO of the radical cation is located on the TDT ligand, similar to the HOMO of the neutral complex **2** (**Figure 22**). This suggests that the TDT moiety retains its redox activity following oxidation and may subsequently be reduced reversibly. This raises the question of where the electron spin resides in the radical cation. According to the principles of quantum mechanics, the precise location of an electron cannot be predicted, only its probability distribution as governed by the Heisenberg Uncertainty Principle. The spin density describes the extent of unpaired electron density in a system. It is defined as the summation of the electron densities of electrons of one spin orientation (e.g., up or alpha spin) minus the summation of the electron densities of electrons of the other spin orientation (e.g., down or beta). The net spin density in the radical cation is 1, meaning there is one unpaired electron (following oxidation of the closed-shell, neutral complex **2**) within the system.

Instead of residing on just one atom center in complex **2**, the net spin of the radical cation resides on several atoms. The atoms with the majority of spin density are S2, S1, C10, C11 and C26, with 0.32, 0.22, 0.16, 0.13, and 0.12 $e\text{\AA}^{-3}$, respectively. S2 has the highest spin density in the radical cation of complex **2**. All five atoms listed above comprise 95% of the spin density in the oxidized form of complex **2**. By comparison, just 2% is

located on the In center (In1); this is consistent with the HOMO of the neutral and radical cation, which does not include indium (**Figures 22 and 23**), and reinforces the notion that redox chemistry involving the In center directly is not favorable.

3.8.3.2 Structure of *(NCN)InI(TDT)* (**2**) and its reaction energy profile.

Geometry optimization of the expected product **13** from the oxidation of **2** with diiodine is shown in **Figure 24**. The In1---I1 bond distance is long (2.864 Å), which is not surprising given the indium center is now six-coordinate. The In1–S1 and In1–S2 bond distances are significantly different at 2.702 Å and at 2.510 Å, respectively. Further, both the In1–S1 and In1–S2 bonds in complex **13** are longer than the In1–S1 (2.401 Å) and In1–S2 (2.401 Å) bond distances in the neutral molecule (**2**). Considering that complex **13** is a six-coordinate system, the longer bond distances are reasonable, suggesting that complex **13** could be synthesized.

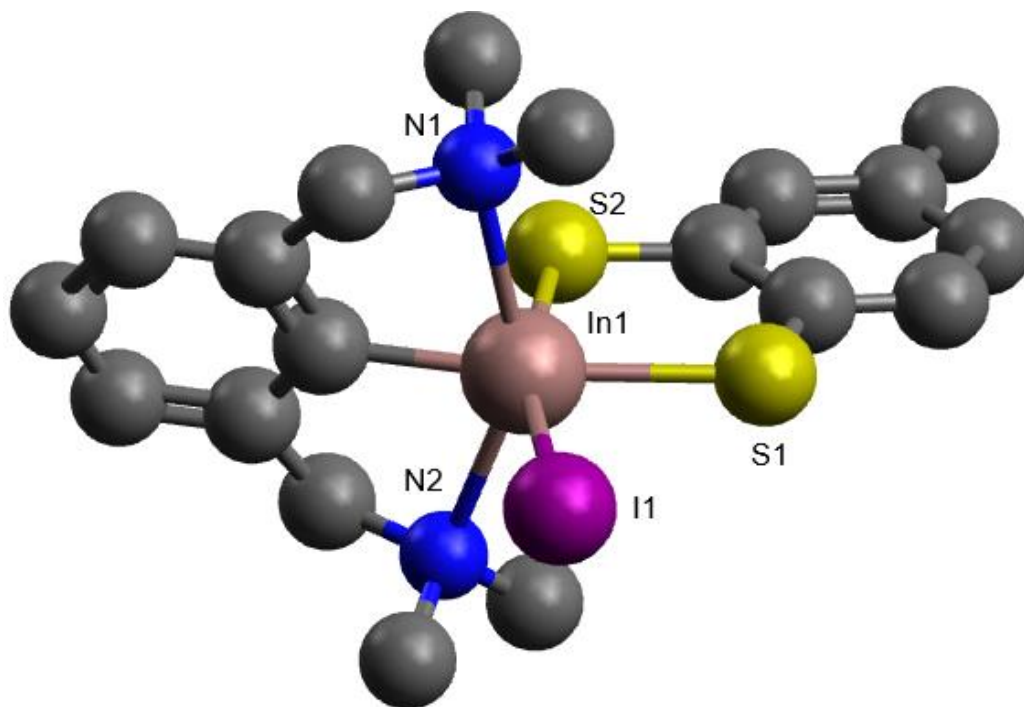


Figure 24: Geometry-optimized structure of **13**. Hydrogen atoms are omitted for clarity.

The calculated reaction energy of the reaction between complex **2** and I₂ (Eqn. 4) is -33.6 kJ mol⁻¹, suggesting that the formation of complex **13** is favourable and, in

principle, could be synthesized. Experimentally, however, complex **13** could not be isolated during the course of this project.



It should be noted that only the thermodynamic aspect of this reaction has thus far been considered; the kinetic aspect has not been addressed. Therefore, even though the reaction to form complex **13** is calculated to be exothermic, a large activation barrier may be prohibiting product formation. Since the reaction mechanism is unknown, it is challenging to determine the energy of the activation. Also, it is worth noting that solvent effects were not considered in these calculations. If they were considered, it is unlikely to significantly change the energy profile however, because there is no experimental indication that solvation effects govern reactivity. If anything, gas-phase calculations provide a rigorous bound to an energetic profile since any type of solvation effect would stabilise the system (reactants and/or products). Additionally, for simplicity we assume that the reactants are infinitely separated species when calculating the reaction energies, since it is not practical to know the configuration of the reactant complex *a priori*, and especially in the absence of detailed mechanistic information, which is beyond the scope of the present work.

Overall, it can be concluded that the reaction to oxidize (NCN)In(TDT) (Eqn 4) is predicted to be exothermic. That the reaction is not productive experimentally suggests that heating the reaction could drive the reaction forward and potentially yield the expected product **13**.

3.9 [MeIn(ABT)py]₂ (**3**)

3.9.1 Structure of [MeIn(ABT)py]₂ (**3**)

The structure of [MeIn(ABT)(py)]₂ (**3**) is similar to that of complex **1** and shows a dimeric species via strong intermolecular In1...N1* interactions (**Figure 25**). Indium is again in a distorted trigonal bipyramidal bonding environment with a methyl carbon atom

(C1), a sulfur atom (S1) from the chelating ABT ligand and a nitrogen atom (N1*) from a bridging ABT ligand in equatorial sites, and a pyridine nitrogen atom (N2) and a nitrogen atom (N1) of the chelating ABT ligand in axial sites. The intermolecular In1–N1 interaction bond distance [2.197(6) Å] is shorter than the axial In1–N1* bond distance to the chelating ABT ligand [2.330(9) Å], again suggesting a very strongly bonded dimer.

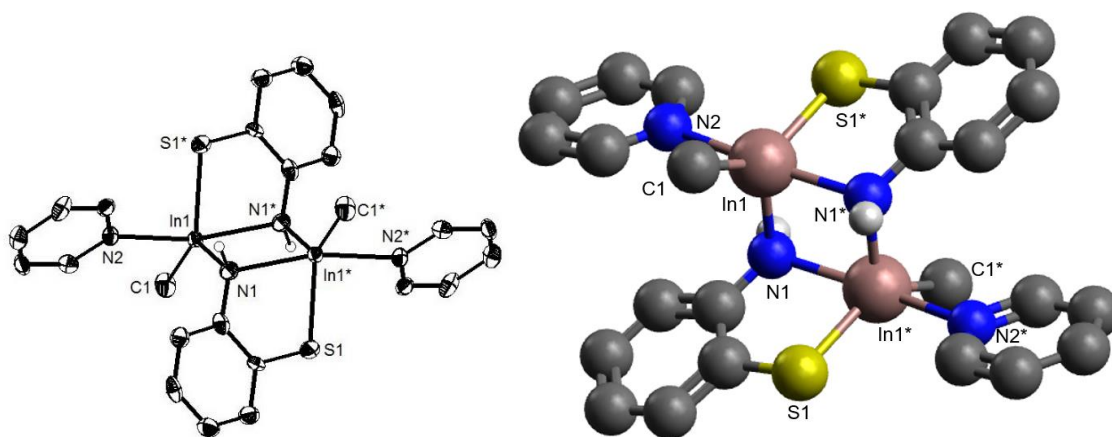


Figure 25: X-ray crystal (left, 30% probability ellipsoids) and geometry-optimized (right) structures of [MeIn(ABT)py]₂ (**3**). Except for N-H, hydrogen atoms are omitted for clarity.

Table 3 shows a comparison of selected structural parameters of the geometry-optimized structure and X-ray crystal structure of [MeIn(ABT)(py)]₂ (**3**). The calculated values and those through X-ray diffraction are sufficiently close to conclude the validity of the former.

Table 3: Comparison of bond distances (Å) and bond angles (°) of the X-ray crystal structure and geometry-optimized structure of [MeIn(ABT)py]₂ (**3**).

		X-ray crystal structure	Geometry-optimized structure
Bond distances	In1–N1	2.197(6)	2.189
	In1–N2	2.483(11)	2.406
	In1–C1	2.129(10)	2.146
	In1–N1*	2.330(9)	2.240
	In1–S1*	2.467(3)	2.461
Bond angles	C1–In1–S1*	135.3(3)	139.8
	C1–In1–N1	124.2(4)	120.4
	N1–In1–S1*	100.5(2)	99.7
	N1–In1–N1*	161.2(3)	85.7

3.9.2 Dimerization of $[\text{MeIn}(\text{ABT})\text{py}]_2$ (**3**) via bridging nitrogen atoms of ABT

The structure of **3** resembles that of $[\text{MeIn}(\text{TDT})\text{py}]_2$ (**1**), which dimerizes via bridging TDT sulfur atoms. Therefore, dimerization in **3** was expected to be linked via the sulfur atoms (S1 and S1*) of the ABT ligand, given the larger atomic radius and soft nature of sulfur versus nitrogen. However, the X-ray crystal structure reveals that bridging occurs via the ABT amine nitrogen atoms. Therefore, DFT calculations were performed to provide insight into the preference for the *N*-linked dimer. Both the *S*-linked and *N*-linked dimer were geometry-optimized and it was found that the *S*-linked dimer (**Figure 26**, right) is lower in energy by 23.3 kJ mol^{-1} compared with the *N*-linked dimer (**Figure 26**, left). This contradicts the experimental data, so the bond angles and distances were analyzed in detail to understand this observation.

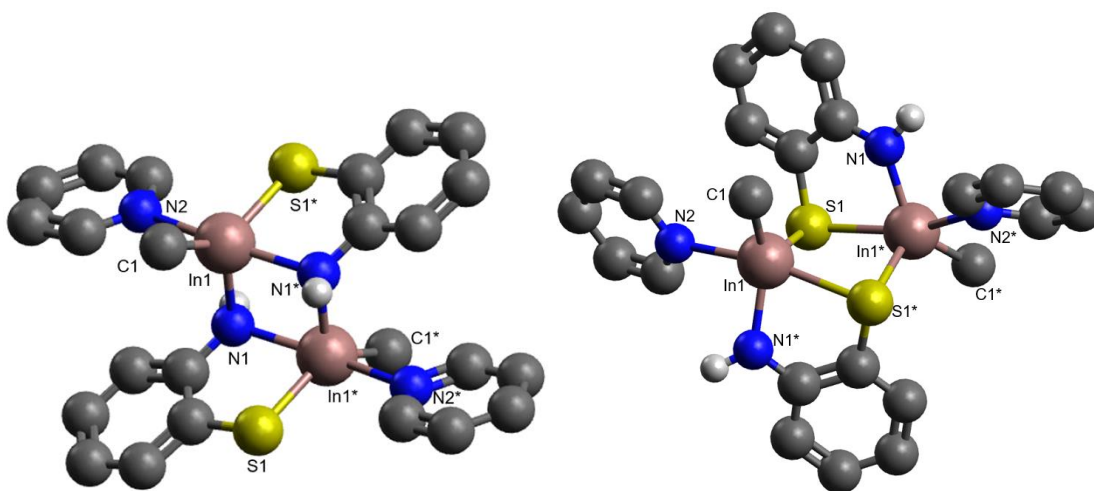


Figure 26: Geometry-optimized structures of *N*-linked (left) and *S*-linked (right) $[\text{MeIn}(\text{ABT})\text{py}]_2$ dimers. Except for N-H, hydrogen atoms are omitted for clarity.

Table 4: Comparing the bond distances (Å) and the bond angles (°) of the calculated structures of *N*-linked and *S*-linked [MeIn(ABT)py]₂ (**3**) dimers.

		[MeIn(ABT)py] ₂			
		<i>N</i> -linked		<i>S</i> -linked	
Bond distances	In1–N1	2.189		In1–S1	2.560
	In1–N1*	2.240		In1–S1*	2.653
	In1–C1	2.189		In1–C1	2.143
	In1–N2	2.406		In1–N2	2.369
	In1–S1*	2.461		In1–N1*	2.062
Bond angles	C1–In1–S1*	139.8		C1–In1–N1*	136.7
	C1–In1–N1	120.4		C1–In1–S1	119.1
	N1–In1–N1*	85.7		S1–In1–S1*	88.6
	N1–In1*–N1*	85.7		S1–In1*–S1*	89.5
Dihedral angle	In1–N1–In1*–N1*	-0.0		In1–S1–In1*–S1*	22.7
	In1–N1*–In1*–N1	0.0		In1–S1*–In1*–S1	-21.9

As seen in Table 4, the In1–N1 and In1–N1* bond distances are shorter in the *N*-linked structure than the In1–S1 and In1–S1* bond distances in the *S*-linked structure. This is expected because nitrogen has a smaller atomic radius than sulfur. The most significant difference in the two structures is that the dihedral angle of In1–N1–In1*–N1* is 0.0°, whereas the dihedral angle for In1–S1–In1*–S1* ring is 22.7°. This difference can be seen in the *S*-linked dimer in the form of a twisted center ring (**Figure 27**). Preference for the *N*-bridged dimer is likely because nitrogen is a better sigma donor than sulfur and forms stronger bonding interactions with the Lewis acidic indium centre.

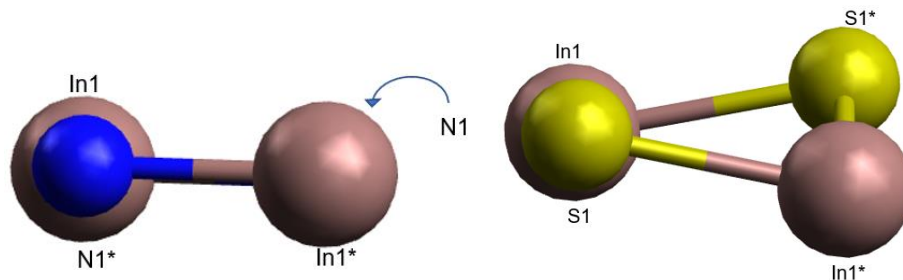
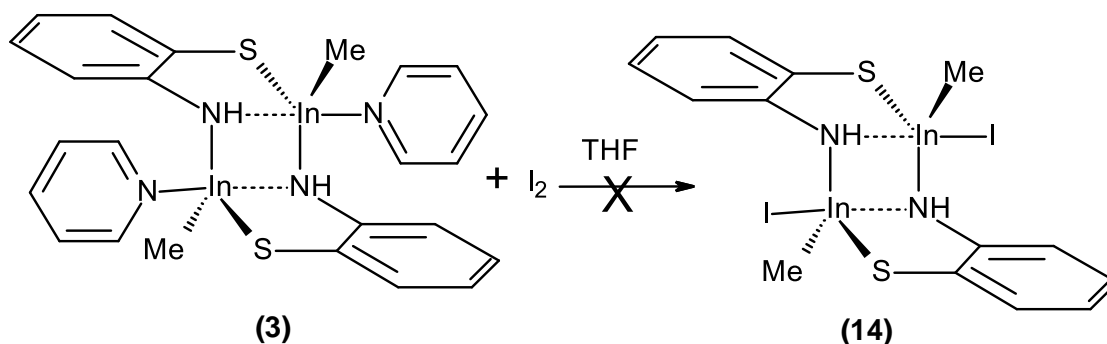


Figure 27: Center rings of the *N*-linked and *S*-linked [MeIn(ABT)py]₂ dimers. N1 in the *N*-linked ring is located behind In1*. Hydrogen atoms are omitted for clarity.

3.9.3 Reaction of [MeIn(ABT)py]₂ (**3**) with I₂

Complex **3** was reacted with one equivalent of I₂ (**Scheme 17**) to test its reactivity. Addition of a light purple solution of [MeIn(ABT)py]₂ to a solution of I₂ yielded no obvious

colour change (**Figure 28**). The colour was dark red after the addition was complete, which suggests that I_2 might have reacted but the purple colour of **3** did not allow observation of any further colour change. When the solution was stored at $-15\text{ }^\circ\text{C}$ overnight, no precipitate formed. This may be because of the scale of the reaction; only 50 mg of $[\text{MeIn}(\text{TDT})\text{py}]_2$ was used, which might not have been enough to stimulate crystallisation.



Scheme 17: Addition of $[\text{MeIn}(\text{ABT})\text{py}]_2$ (**3**) to a solution of I_2 .

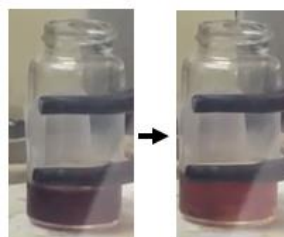


Figure 28: Colour change during the addition of $[\text{MeIn}(\text{TDT})\text{py}]_2$ to a solution of I_2 .

3.9.4 Theoretical calculations on $[\text{MeIn}(\text{ABT})\text{py}]_2$ (**3**)

3.9.4.1 Structure of $[\text{MeIn}(\text{ABT})]_2$ (**3**)

DFT calculations were performed to provide insight into whether the target complex **14** can be isolated from the reaction of **2** and diiodine, and also to determine whether complex **3** could react as efficiently as **1**. The calculated structure of **14** shows that both the $\text{In}2\text{-I}1$ and $\text{In}1\text{-I}2$ bond distances are 2.831 \AA , which is relatively close to the literature value of 2.746 \AA (**Figure 29**).⁵³ The $\text{In}1\text{-S}1$ and $\text{In}1\text{-S}2$ bond distances for complex **14** are both at 2.497 \AA , and the $\text{In}1\text{-S}1$ and $\text{In}1\text{-S}2$ bond distances in the starting material **3** are 2.461 \AA and 2.462 \AA , respectively. The similarity between these bond distances suggests that that complex **14** should be isolable too.

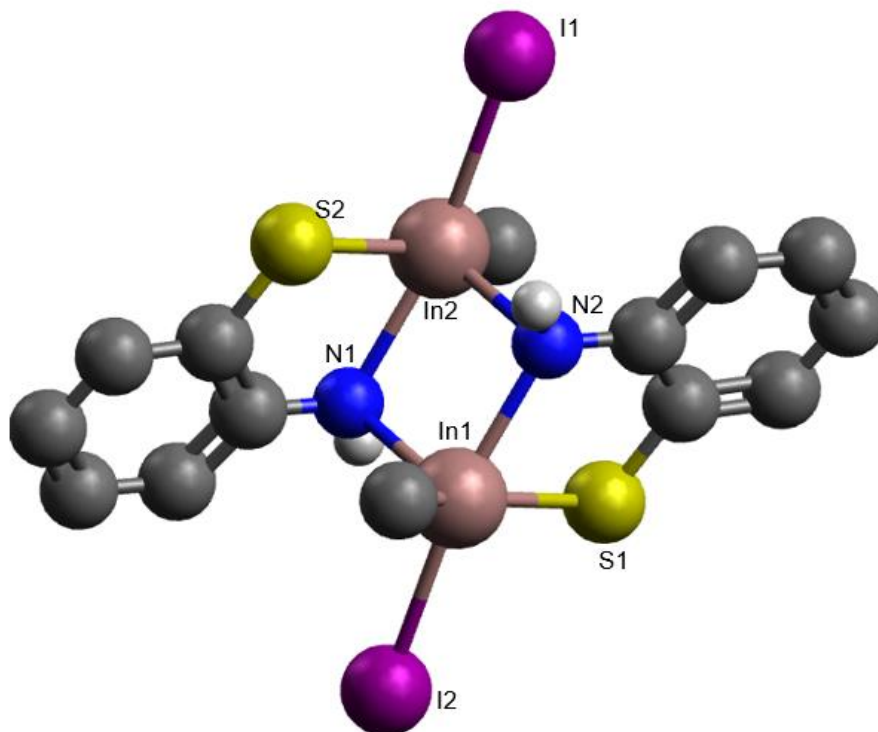
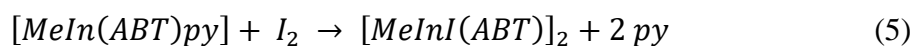


Figure 29: Geometry-optimized structure of **14**. Except for N-H, hydrogen atoms are omitted for clarity.

The calculated reaction energy associated with the reaction of complex **3** and I_2 can be determined using Eqn. (5).



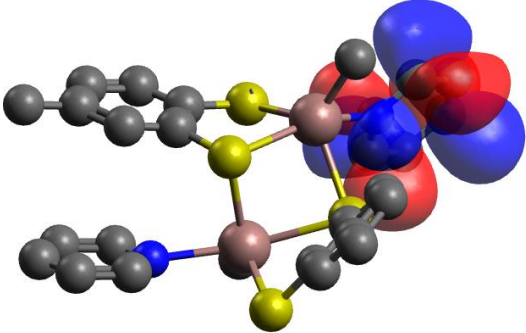
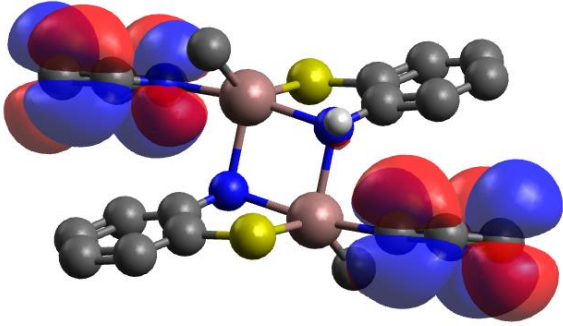
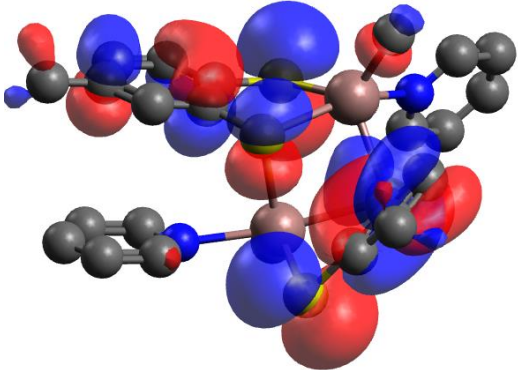
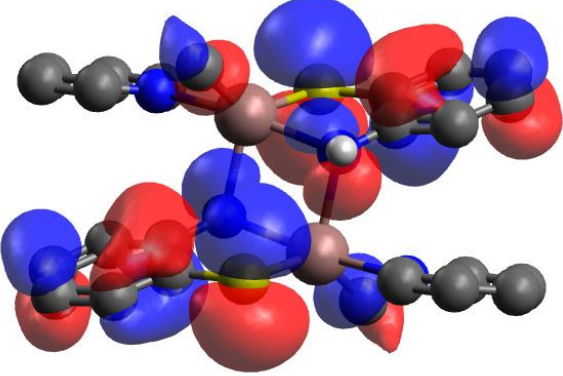
The predicted reaction energy for this reaction is endothermic by $118.2 \text{ kJ mol}^{-1}$. The high energy of complex **14** relative to the starting material (**1**) suggests its formation is unlikely and/or that its formation may be fleeting. Indeed, it is possible that complex **14** forms, but it is too short-lived to be isolated, and the starting material (and/or other products) is formed. However, to further understand whether the ABT dimer (**3**) can react with I_2 the same way the TDT dimer (**1**), the frontier molecular orbitals were examined.

3.9.4.2 Investigation of frontier molecular orbitals of $[MeIn(ABT)py]_2$ (**3**)

The reactivity or stability of a compound is related to its frontier orbitals (HOMO and LUMO). The difference in energy between the HOMO and LUMO can provide insight into various parameters such as reactivity and stability of the complex. For example, a large

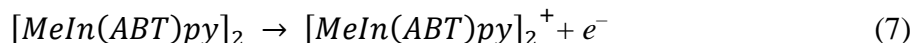
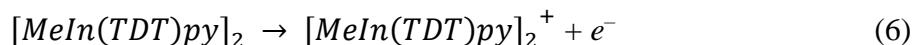
HOMO-LUMO energy gap is indicative of high excitation energies for many excited states, good stability, and a high chemical hardness for the complex.⁵⁴ The HOMO-LUMO gaps of **1** and **3** were therefore calculated to understand these complexes more fully. The frontier orbitals of both complexes and the energies associated with them are shown in **Table 5**. The LUMO of complex **1** is located on the top pyridine ring and the HOMO is located on the TDT ligand. The LUMO of complex **3** is located on both the pyridine rings and the HOMO is located primarily on the ABT ligand. The HOMO-LUMO gap (Δ_{H-L} , eV) is 3.66 eV for complex **1**, whereas it is 3.562 eV for complex **3**. These results suggest that the ABT-containing complex **3** should be more reactive than the TDT-containing complex **1**. But this is not observed experimentally; in fact, the opposite is observed. Clearly, the lack of reactivity of the ABT complex is more complicated than a simple analysis on HOMO-LUMO gaps can provide.

Table 5: Frontier molecular orbitals for complexes **1** and **3** along with their calculated energies.

[MeIn(TDT)py] ₂ (1)	[MeIn(ABT)py] ₂ (3)
	
LUMO = -1.653 eV	LUMO = -1.627 eV
	
HOMO = -5.313 eV	HOMO = -5.189 eV

3.9.4.3 Investigation of ionization energy of $[MeIn(TDT)py]_2$ (**1**) and $[MeIn(ABT)py]_2$ (**3**)

The ionization energy of complexes **1** and **3** can be calculated using Equations 6, 7, and 8 respectively.



The ionization energies of complexes **1** and **3** are calculated to be $603.5 \text{ kJ mol}^{-1}$ and $598.9 \text{ kJ mol}^{-1}$, respectively. The slightly higher ionization energy (4.6 kJ mol^{-1}) of the TDT dimer (**1**) than the ABT dimer (**3**) suggests that the former would oxidize more easily than the latter. But this is not what is observed experimentally. However, it should be noted that the small difference of $\sim 5 \text{ kJ mol}^{-1}$ is within chemical accuracy of the theoretical method used here.⁵⁵

At this point it is instructive to consider the ionization energy calculated here relative to the calculated HOMO-LUMO gaps from section 3.9.4.2. Ionization is the process by which electrons are infinitely separated from a system (from the HOMO, for example). For systems in which the energy difference between adjacent energy levels is relatively small, less energy will therefore be required to oxidize/ionize the molecule. For the redox-active TDT ligand, for instance, the energy separation between the HOMO and LUMO is larger than that for ABT (cf. Table 5), and this is reflected in its higher ionization energy.

This tells us that the HOMO-LUMO gap alone cannot help us understand the lack of reactivity of ABT-containing complexes. However, the slightly higher ionization energy for TDT is consistent with the notion that larger HOMO-LUMO gaps are more difficult to ionize.

3.10 (NCN)In(ABT) (4)

3.10.1 Structure of (NCN)In(ABT) (4)

The structure of (NCN)In(ABT) (**4**, **Figure 4**) is discussed in section 3.6 (**Figure 30**).⁵⁶

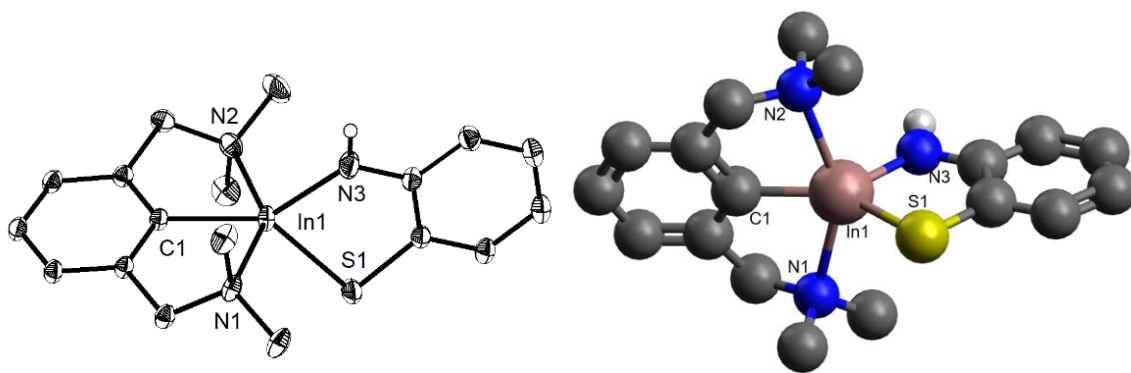


Figure 30: X-ray crystal (left, 30% probability ellipsoids) and geometry-optimized (right) structures of (NCN)In(ABT) (**4**). Except for N-H, hydrogen atoms are omitted for clarity.

Similar to the other complexes here, the structural parameters values obtained from the calculated structure and those obtained through X-ray crystallography are similar enough to conclude the validity of the former (**Table 6**).

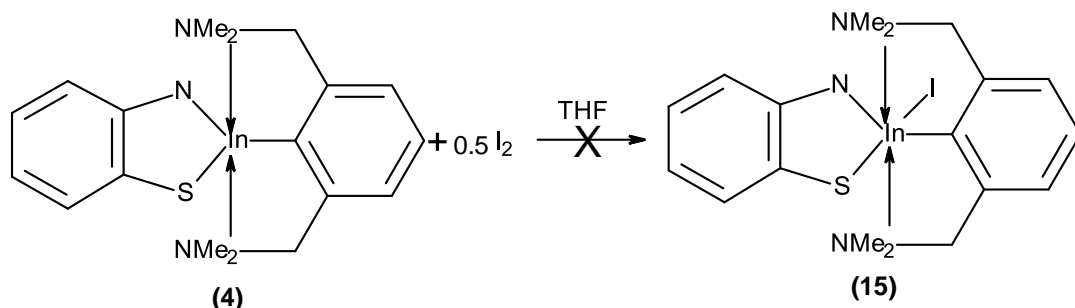
Table 6: Comparison of bond distances (Å) and bond angles (°) of the X-ray crystal structure and geometry-optimized structure of (NCN)In(ABT) (**4**).

		X-ray crystal structure	Geometry-optimized structure
Bond distances	In1-C1	2.1169(9)	2.114
	In1-S1	2.4459(4)	2.396
	In1-N1	2.5101(9)	2.476
	In1-N2	2.538(1)	2.490
	In1-N3	2.062(1)	2.034
Bond angles	C1-In1-S1	132.62(3)	140.0
	C1-In1-N3	142.24(4)	131.9
	S1-In1-N3	85.13(3)	88.0
	N1-In1-N2	148.07(3)	148.6

3.10.2 Reaction of (NCN)In(ABT) (4) with I₂

Complex **4** was reacted with one equivalent of I₂ to test its reactivity (**Scheme 18**). Dissolving (NCN)In(ABT) in THF gave a pale yellow solution. Upon addition to the dark

purple I_2 solution, the purple colour intensified until it was blackish purple. There was no observable colour change after stirring for 60 min, suggesting that no reaction occurred (**Figure 31**).



Scheme 18: Addition of (NCN)In(ABT) (**4**) to a solution of 0.5 equivalence of I_2 .

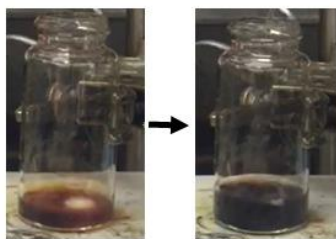


Figure 31: Intensification of purple colour during the addition of (NCN)In(ABT) to a solution of I_2 .

3.10.3 Theoretical calculations on (NCN)In(ABT) (**4**)

DFT calculations were performed to provide insight into whether the target complex **15** can be isolated from the reaction of **4** and diiodine and to determine whether complex **4** could react as efficiently as **2**.

Geometry optimization of the possible product **15** from the oxidation of **4** with diiodine is shown in **Figure 32**. The In1---I1 bond distance is long (2.901 Å), which is not surprising given the indium centre is now six-coordinate. The In1–S1 and In1–N3 bond distances are significantly different at 2.677 Å and at 2.117 Å, respectively. Both bond distances are longer than the analogous bond distances in the starting material (**4**) (cf. In1–S1= 2.396 Å and In1–N1= 2.034 Å), suggesting that complex **13** is isolable considering the six-coordinate system.

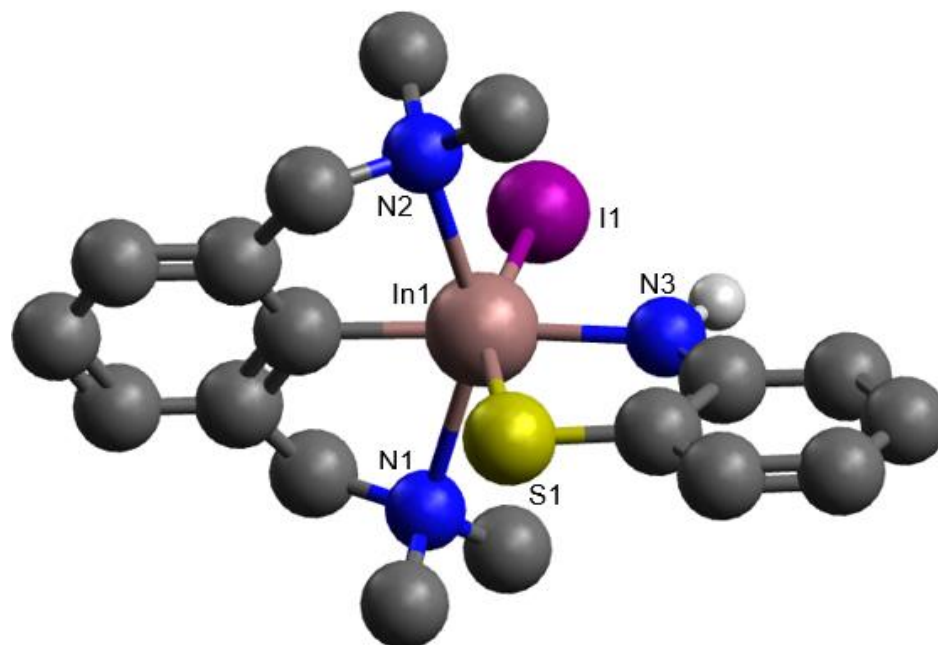


Figure 32: Geometry-optimized structure of complex **15**. Except for N-H, hydrogen atoms are omitted for clarity.

The calculated reaction energy for the reaction of (NCN)In(ABT) (**4**) with I₂ to form (NCN)InI(ABT) (**15**) is predicted to be exothermic by -90.0 kJ mol⁻¹ (Equation 9).



Interestingly, although the calculated reaction energy predicts formation of **15** to be favourable, it is not observed experimentally, as no discolouration of the mixture was observed during the reaction. This result once again demonstrates that the TDT ligand reacts differently than the ABT ligand in these indium complexes.

3.10.4 Investigation of frontier molecular orbitals of (NCN)In(TDT) (**2**) and (NCN)In(ABT) (**4**)

The frontier orbitals of complexes **2** and **4** and their energies are shown in **Table 7** that its formation may be fleeting. Indeed, it is possible that complex **14** forms but it is too short-lived to be isolated, and the starting material (and/or other products) is formed.

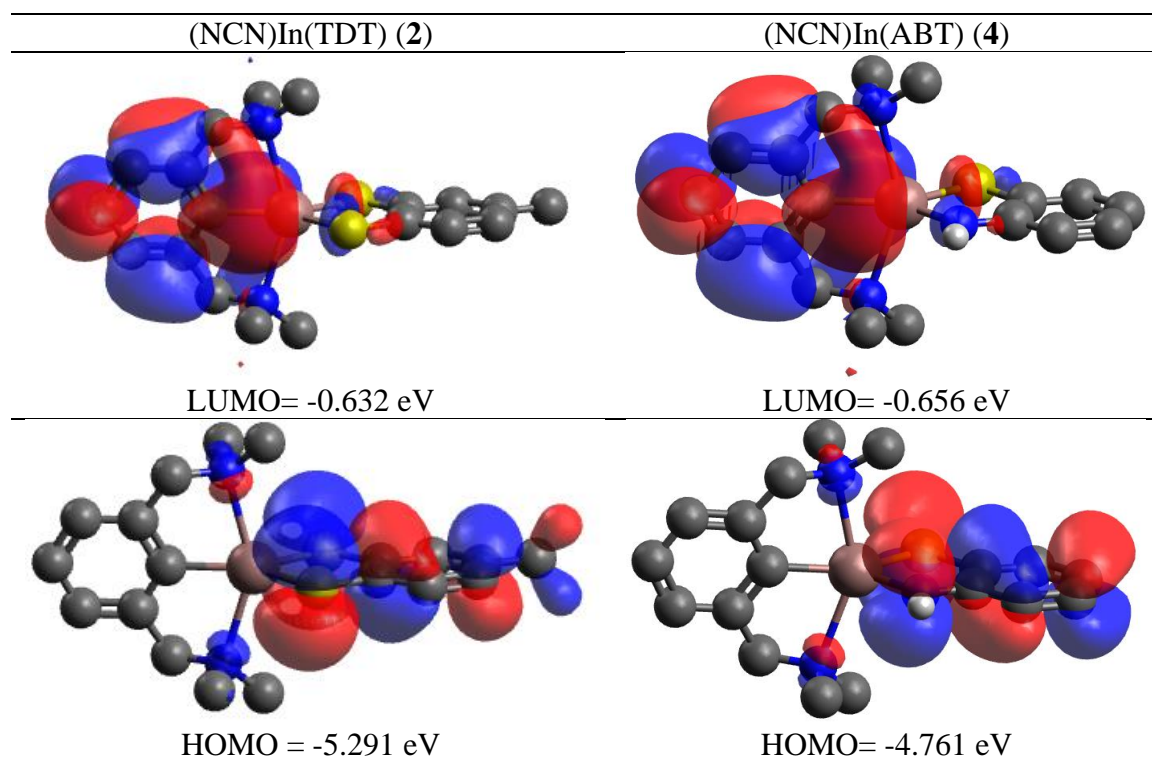
However, to further understand whether the ABT dimer (**3**) can react with I₂ in the same way as the TDT dimer (**1**), the frontier molecular orbitals were examined.

3.10.4.1 Investigation of frontier molecular orbitals of [MeIn(ABT)py]₂ (**3**)

The reactivity or stability of a compound is related to its frontier orbitals (HOMO and LUMO). The difference in energy between the HOMO and LUMO can provide insight into various parameters such as reactivity and stability of the complex. For example, a large HOMO-LUMO energy gap is indicative of high excitation energies for many excited states, good stability, and a high chemical hardness for the complex.⁵³ The HOMO-LUMO gaps of **1** and **3** were therefore calculated to understand these complexes more fully. The frontier orbitals of both complexes and the energies associated with them are shown in **Table 5**. The LUMO of complex **1** is located on the top pyridine ring and the HOMO is located on the TDT ligand. The LUMO of complex **3** is located on both the pyridine rings and the HOMO is located primarily on the ABT ligand. The HOMO-LUMO gap (Δ_{H-L} , eV) is 3.66 eV for complex **1**, whereas it is 3.562 eV for complex **3**. These results suggest that the ABT-containing complex **3** should be more reactive than the TDT-containing complex **1**. But this is not observed experimentally; in fact, the opposite is observed. Clearly, the lack of reactivity of the ABT complex is more complicated than an analysis on HOMO-LUMO gaps can provide.

Table 5 The LUMO of complex **2** is located on the pincer ligand and the HOMO is located on the TDT ligand. The LUMO of complex **4** is located on the pincer ligand as well and the HOMO is located primarily on the ABT ligand. This shows that the reactive sites on both complexes are the redox-active ligands. However, the calculated HOMO-LUMO gap, Δ_{H-L} , is 4.659 eV for complex **2**, whereas it is 4.105 eV for complex **4**. Which shows that **4** should be easier to oxidize than (NCN)In(TDT) (**2**).

Table 7: Frontier molecular orbitals of complexes **2** and **4** along with their calculated energies.



This is at odds with the experimental data again suggesting that that the HOMO-LUMO gap—alone—cannot help us understand the lack of reactivity of the ABT-containing complexes.

4. Conclusions

In conclusion, a procedure to reliably form (NCN)In(ABT) (**4**) as blocky, yellowish crystals and (NCN)In(HABT)₂ (**10**) as brown plate-like crystals has been developed. The X-ray crystal structure of **4** shows a distorted trigonal bipyramidal geometry at the indium centre, with a tridentate pincer ligand and a bidentate TDT ligand. Complex **4** co-crystallizes with half an equivalent of (THF)₂Li(μ-Cl)₂Li(THF). The X-ray crystal structure of **10** shows a monomeric compound and a distorted trigonal bipyramidal bonding environment for indium, with a tridentate pincer ligand and two monodentate HABT ligands.

Computational studies indicate that dimerization is more favourable from an energetic perspective for the MeInL species versus the (NCN)InL species (L = TDT, ABT). The reactivities of [MeIn(TDT)(py)]₂ (**1**), (NCN)In(TDT) (**2**), [MeIn(ABT)(py)]₂ (**3**) and (NCN)In(TDT) (**4**) were tested experimentally with I₂ as a mild oxidizing agent. The TDT complexes reacted with I₂ but, notably, the ABT complexes did not. The theoretical calculations performed herein suggest that the expected iodine-containing products **12–15** could be isolable; their formation may be encouraged with an external energy input such as heating.

Understanding the reactivity of the redox-active indium complexes synthesized here (**1–4**) is an important step in developing alternatives to transition metals in catalytic chemistry, and these complexes would be ideal green catalysts. Indeed, they are cheap to make, stable, have a favorable risk-reward profile for human health and the environment, and they likely undergo reversible redox reactions.

5. Future Directions

In the future, reliable methods for accessing the redox activity of stable indium complexes must be developed. To further enhance the scope of these complexes, their reactivity should be tested with stronger oxidizing agents such as Cl₂ and/or another mild oxidizing like PhSSPh. The redox activity of these complexes should also be assessed quantifiably through cyclic voltammetry, which will demonstrate stability of the

compounds on being reduced and oxidized. More work is needed to understand the lack of reactivity of the ABT complexes (**3** and **4**). Electron paramagnetic resonance spectroscopy can provide more information about the potential for the involvement of radical-based chemistry in these reactions, and this should be explored. Further, to rationalise these results and predict reactivity, computational calculations could continue to be employed at the PBE1PBE-GD3BJ/def2-TZVP level of theory for these systems.

6. References

- (1) Global, Regional, and National Age–Sex Specific All-Cause and Cause-Specific Mortality for 240 Causes of Death, 1990–2013: A Systematic Analysis for the Global Burden of Disease Study 2013. *The Lancet* **2015**, 385 (9963), 117–171.
- (2) Varma, D. F.; Mulay, S. CHAPTER 7 - The Bhopal Accident and Methyl Isocyanate Toxicity. In *Toxicology of Organophosphate & Carbamate Compounds*; Gupta, R. C., Ed.; Academic Press: Burlington, **2006**; pp 79–88.
- (3) US EPA, O. Pollution Prevention Act of 1990 <https://www.epa.gov/p2/pollution-prevention-act-1990>
- (4) Anastas, P.; Eghbali, N. Green Chemistry: Principles and Practice. *Chem. Soc. Rev.* **2009**, 39 (1), 301–312.
- (5) *Green Chemical Syntheses and Processes*; Anastas, P. T., Heine, L. G., Williamson, T. C., Eds.; ACS Symposium Series; American Chemical Society: Washington, DC, **2000**; Vol. 767.
- (6) Varma, R. S. Greener and Sustainable Chemistry. *Applied Sciences* **2014**, 4 (4), 493–497.
- (7) Ivanković, A.; Dronjić, A.; Bevanda, A.; Talić, S. Review of 12 Principles of Green Chemistry in Practice. *International Journal of Sustainable and Green Energy* **2017**, 6, 39–48.
- (8) Sheldon, R. A. The E Factor 25 Years on: The Rise of Green Chemistry and Sustainability. *Green Chem.* **2017**, 19 (1), 18–43.
- (9) Chanshetti, U. Green Chemistry: Environmentally Benign Chemistry. *Chemical Science* **2014**, 1, 110–115.
- (10) Cue, B. W.; Zhang, J. Green Process Chemistry in the Pharmaceutical Industry. *Green Chemistry Letters and Reviews* **2009**, 2 (4), 193–211.
- (11) Anastas, P.; Eghbali, N. Green Chemistry: Principles and Practice. *Chemical Society Reviews* **2010**, 39 (1), 301–312.
- (12) Etzkorn, F. A. *Green Chemistry: Principles and Case Studies*; Royal Society of Chemistry, **2019**.
- (13) Delidovich, I.; Palkovits, R. Catalytic versus Stoichiometric Reagents as a Key Concept for Green Chemistry. *Green Chemistry* **2016**, 18 (3), 590–593.
- (14) Anastas, P. T.; Kirchhoff, M. M.; Williamson, T. C. Catalysis as a Foundational Pillar of Green Chemistry. *Applied Catalysis A: General* **2001**, 221 (1), 3–13.
- (15) Einstein, F. W. B.; Hunter, G.; Tuck, D. G.; Yang, M. K. Complexes of Indium with Unsaturated Bidentate Sulphur-Donor Ligands. *Chem. Commun. (London)* **1968**, No. 7, 423–423.
- (16) Ludwig, J. R.; Schindler, C. S. Catalyst: Sustainable Catalysis. *Chem* **2017**, 2 (3), 313–316.
- (17) Lehmann, H.; LaVecchia, L. Scale-Up of Organic Reactions in a Pharmaceutical Kilo-Lab Using a Commercial Microwave Reactor. *Org. Process Res. Dev.* **2010**, 14 (3), 650–656.
- (18) Devendar, P.; Qu, R.-Y.; Kang, W.-M.; He, B.; Yang, G.-F. Palladium-Catalyzed Cross-Coupling Reactions: A Powerful Tool for the Synthesis of Agrochemicals. *J. Agric. Food Chem.* **2018**, 66 (34), 8914–8934.

- (19) Roy, D.; Uozumi, Y. Recent Advances in Palladium-Catalyzed Cross-Coupling Reactions at Ppm to Ppb Molar Catalyst Loadings. *Advanced Synthesis & Catalysis* **2018**, *360* (4), 602–625.
- (20) Anila, P. A.; Sutha, J.; Nataraj, D.; Ramesh, M. In Vivo Evaluation of Nano-Palladium Toxicity on Larval Stages and Adult of Zebrafish (*Danio Rerio*). *Science of The Total Environment* **2021**, *765*, 144268.
- (21) Egorova, K. S.; Ananikov, V. P. Toxicity of Metal Compounds: Knowledge and Myths. *Organometallics* **2017**, *36* (21), 4071–4090.
- (22) Alfantazi, A. M.; Moskalyk, R. R. Processing of Indium: A Review. *Minerals Engineering* **2003**, *16* (8), 687–694.
- (23) Green, M. *Organometallic Chemistry: Volume 30*; Royal Society of Chemistry, **2007**.
- (24) Gándara, F.; Gomez-Lor, B.; Gutiérrez-Puebla, E.; Iglesias, M.; Monge, M. A.; Proserpio, D. M.; Snejko, N. An Indium Layered MOF as Recyclable Lewis Acid Catalyst. *Chem. Mater.* **2008**, *20* (1), 72–76.
- (25) Eisenberg, R.; Gray, H. B. Noninnocence in Metal Complexes: A Dithiolene Dawn. *Inorg. Chem.* **2011**, *50* (20), 9741–9751.
- (26) Lyaskovskyy, V.; de Bruin, B. Redox Non-Innocent Ligands: Versatile New Tools to Control Catalytic Reactions. *ACS Catal.* **2012**, *2* (2), 270–279.
- (27) R. Luca, O.; H. Crabtree, R. Redox-Active Ligands in Catalysis. *Chemical Society Reviews* **2013**, *42* (4), 1440–1459.
- (28) Sproules, S.; Wieghardt, K. O-Dithiolene and o-Aminothiolate Chemistry of Iron: Synthesis, Structure and Reactivity. *Coordination Chemistry Reviews - COORD CHEM REV* **2010**, *254*, 1358–1382.
- (29) Piskunov, A. V.; Meshcheryakova, I. N.; Ershova, I. V.; Bogomyakov, A. S.; Cherkasov, A. V.; Fukin, G. K. The Reactivity of O-Amidophenolate Indium(III) Complexes towards Different Oxidants. *RSC Adv.* **2014**, *4* (80), 42494–42505.
- (30) Chauhan, H. P. S.; Joshi, S.; Bakshi, A.; Carpenter, J. Structural Investigation on Toluene-3,4-Dithiolatoantimony(III) Alkyldithiocarbonate Complexes: Thermal, Powder XRD and Biological Studies. *New J. Chem.* **2015**, *39* (3), 2279–2288.
- (31) Lawrence, M. A. W.; Green, K.-A.; Nelson, P. N.; Lorraine, S. C. Review: Pincer Ligands—Tunable, Versatile and Applicable. *Polyhedron* **2018**, *143*, 11–27.
- (32) Tekarli, S. M.; Drummond, M. L.; Williams, T. G.; Cundari, T. R.; Wilson, A. K. Performance of Density Functional Theory for 3d Transition Metal-Containing Complexes: Utilization of the Correlation Consistent Basis Sets. *J. Phys. Chem. A* **2009**, *113* (30), 8607–8614.
- (33) Mardirossian, N.; Head-Gordon, M. Thirty Years of Density Functional Theory in Computational Chemistry: An Overview and Extensive Assessment of 200 Density Functionals. *Molecular Physics* **2017**, *115* (19), 2315–2372.
- (34) Kruse, H.; Goerigk, L.; Grimme, S. Why the Standard B3LYP/6-31G* Model Chemistry Should Not Be Used in DFT Calculations of Molecular Thermochemistry: Understanding and Correcting the Problem. *J. Org. Chem.* **2012**, *77* (23), 10824–10834.
- (35) Nhat, P. V.; Si, N. T. Performance of B3PW91, PBE1PBE and OPBE Functionals in Comparison to B3LYP for ¹³C NMR Chemical Shift Calculations. **2017**, 11.

- (36) Queen, J. D.; Lehmann, A.; Fettinger, J. C.; Tuononen, H. M.; Power, P. P. The Monomeric Alane-diyl :AlAriPr₈ (AriPr₈ = C₆H₂-2,6-(C₆H₂-2,4,6-Pri₃)₂-3,5-Pri₂): An Organoaluminum(I) Compound with a One-Coordinate Aluminum Atom. *J. Am. Chem. Soc.* **2020**, *142* (49), 20554–20559.
- (37) Stöckli, A.-H. Synthesis of Redox-Active Organoindium Dithiolate Catalysts. *BSc Honours thesis, Mount Allison University* **2020**, 58.
- (38) Kaltsoyannis, N.; McGrady, J. E. *Principles and Applications of Density Functional Theory in Inorganic Chemistry II*; Springer Science & Business Media, **2004**.
- (39) Bibal, C.; Mazières, S.; Gornitzka, H.; Couret, C. New Arylchlorogermynes Stabilized by Two Ortho Side-Chain Donor Ligands. *Polyhedron* **2002**, *21* (27–28), 2827–2834.
- (40) Amijs, C. H. M.; Klink, G. P. M. van; Koten, G. van. Carbon Tetrachloride Free Benzylic Brominations of Methyl Aryl Halides. *Green Chem.* **2003**, *5* (4), 470–474.
- (41) Steenwinkel, P.; James, S. L.; Gossage, R. A.; Grove, D. M.; Kooijman, H.; Smeets, W. J. J.; Spek, A. L.; van Koten, G. Sequential C–H and C–Ru Bond Formation and Cleavage during the Thermally Induced Rearrangement of Aryl Ruthenium(II) Complexes with [C₆H₃(CH₂NMe₂)₂-2,6]- as a Bidentate H₂-C,N Coordinated Ligand. The Crystal Structures of the Isomeric Pairs [RuCl{η⁶-C₁₀H₁₄}{η²-C,N-C₆H₃(CH₂NMe₂)₂-2,N}] (n = 4 or 6) and [Ru(H₅-C₅H₅){η²-C,N-C₆H₃(CH₂NMe₂)₂-2,N}(PPh₃)] (n = 4 or 6). *Organometallics* **1998**, *17* (21), 4680–4693.
- (42) Schumann, H.; Wassermann, W.; Dietrich, A. Synthesis and Molecular Structure of CH₃CH₂-[C(CH₃)₂NCH₂]₂C₆H₃ InCl, an Intramolecular Stabilized Monomeric Diorganoindium Chloride. *Journal of Organometallic Chemistry* **1989**, *365* (1), 11–18.
- (43) Clark, H. C.; Pickard, A. L. Organoindium Chemistry: I. A Convenient Preparation of Dimethylindium(III) Derivatives. *Journal of Organometallic Chemistry* **1967**, *8* (3), 427–434.
- (44) Schumann, H.; Hartmann, U.; Wassermann, W. Synthesis and Characterization of Organogallium and Organoindium Compounds with Tridentate 2,6-Bis[(dialkylamino)methyl]phenyl Ligands. *Chem. Ber.* **1991**, *124* (7), 1567–1569.
- (45) Bibal, C.; Mazières, S.; Gornitzka, H.; Couret, C. New Arylchlorogermynes Stabilized by Two Ortho Side-Chain Donor Ligands. *Polyhedron* **2002**, *21* (27–28), 2827–2834.
- (46) Williams, A.; Burk, R. Carbon Tetrachloride Hepatotoxicity: An Example of Free Radical-Mediated Injury. *Semin Liver Dis* **1990**, *10* (04), 279–284.
- (47) Davis, A.; Fennimore, G. G.; Peck, C.; Walker, C. R.; McIlwraith, J.; Thomas, S. Degradation of Carbon Tetrachloride in a Reducing Groundwater Environment: Implications for Natural Attenuation. *Applied Geochemistry* **2003**, *18* (4), 503–525.
- (48) Mukherjee, D.; Spaniol, T. P.; Okuda, J. Unexpected Alkane Elimination from Cationic Group 13 Dialkyls in a Reaction with a Macrocyclic Polyamine. *Dalton Trans.* **2017**, *46* (3), 651–655.
- (49) Richardson, M. L.; Waggott, A. Occurrence and Fate of Certain Triphenylmethane Blue Dye-stuffs in the Aquatic Environment. *Ecotoxicology and Environmental Safety* **1981**, *5* (4), 424–436.

- (50) Sawyer, D. T.; Srivatsa, G. Susan.; Bodini, M. E.; Schaefer, W. P.; Wing, R. M. Redox Chemistry and Spectroscopy of Toluene-3,4-Dithiol (TDTH₂) and of Its M(TDT)₂²⁻ Complexes with Zinc(II), Copper(II), Nickel(II), Cobalt(II), Iron(II), and Manganese(II). Formation of a Stable Dn-(·Cn·SR) Bond upon Oxidation by One Electron. *J. Am. Chem. Soc.* **1986**, *108* (5), 936–942.
- (51) Sun, M.; Wang, Y.; Zhang, Q.; Xia, Y.; Ge, W.; Guo, D. Prediction of Reversible Disulfide Based on Features from Local Structural Signatures. *BMC Genomics* **2017**, *18*, 279.
- (52) Kröger, J.; Néel, N.; Berndt, R.; Wang, Y. F.; Gopakumar, T. G. Exploring the Organic–Inorganic Interface With a Scanning Tunneling Microscope. In *Encyclopedia of Interfacial Chemistry*; Wandelt, K., Ed.; Elsevier: Oxford, **2018**; pp 81–98.
- (53) Piskunov, A. V.; Mescheryakova, I. N.; Fukin, G. K.; Cherkasov, V. K.; Abakumov, G. A. Indium(III) Complexes with o-Iminobenzoquinone in Different Redox States. *New J. Chem.* **2010**, *34* (8), 1746–1750. <https://doi.org/10.1039/C0NJ00229A>.
- (54) Shafaatian, B.; Mousavi, S. S.; Afshari, S. Synthesis, Characterization, Spectroscopic and Theoretical Studies of New Zinc(II), Copper(II) and Nickel(II) Complexes Based on Imine Ligand Containing 2-Aminothiophenol Moiety. *Journal of Molecular Structure* **2016**, *1123*, 191–198.
- (55) Pople, J. A. Nobel Lecture: Quantum Chemical Models. *Rev. Mod. Phys.* **1999**, *71* (5), 1267–1274.
- (56) Blasberg, F.; Bolte, M.; Wagner, M.; Lerner, H.-W. An Approach to Pin Down the Solid-State Structure of the “Turbo Grignard.” *Organometallics* **2012**, *31* (3), 1001–1005.

7. Appendices

Appendix A: Spectroscopic data

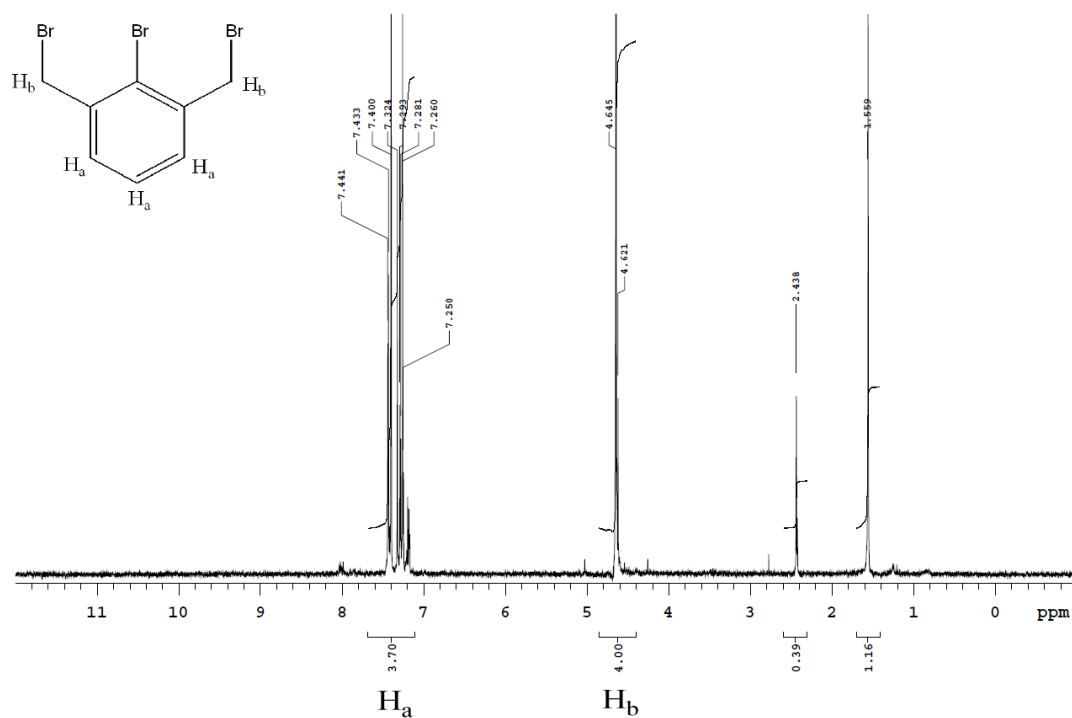


Figure A.1: $^1\text{H-NMR}$ spectrum in CDCl_3 of $\text{C}_6\text{H}_3\text{Br-2,6-(CH}_2\text{Br)}_2$ (**5**) produced from reaction with ultraviolet light.

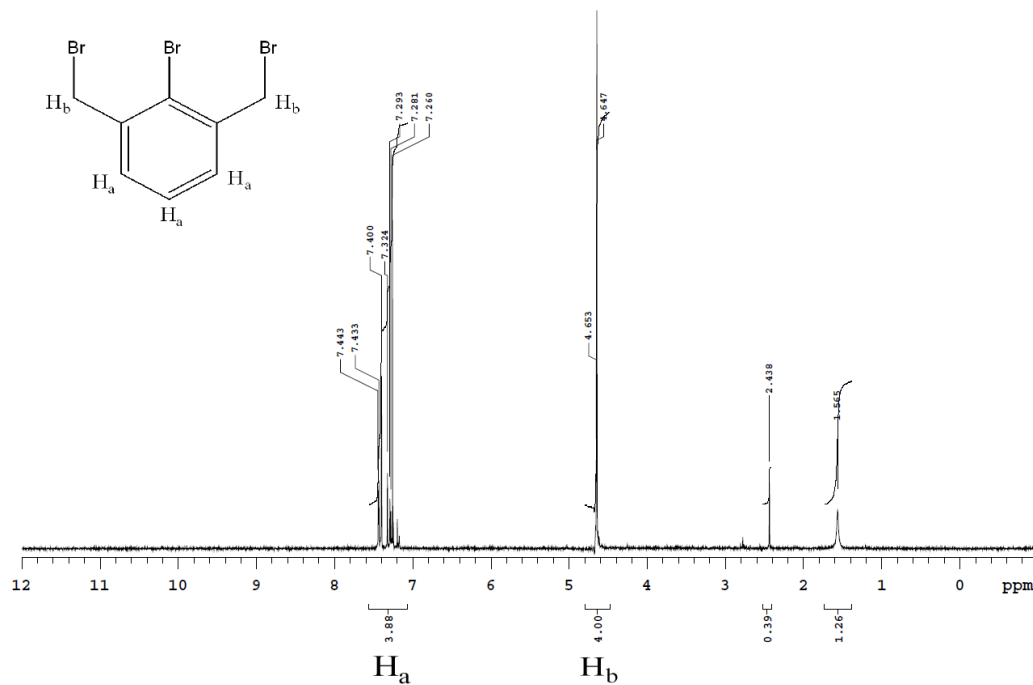


Figure A.2: 1H -NMR spectrum in $CDCl_3$ of $C_6H_3Br-2,6-(CH_2Br)_2$ (**5**) from reaction with infrared light.

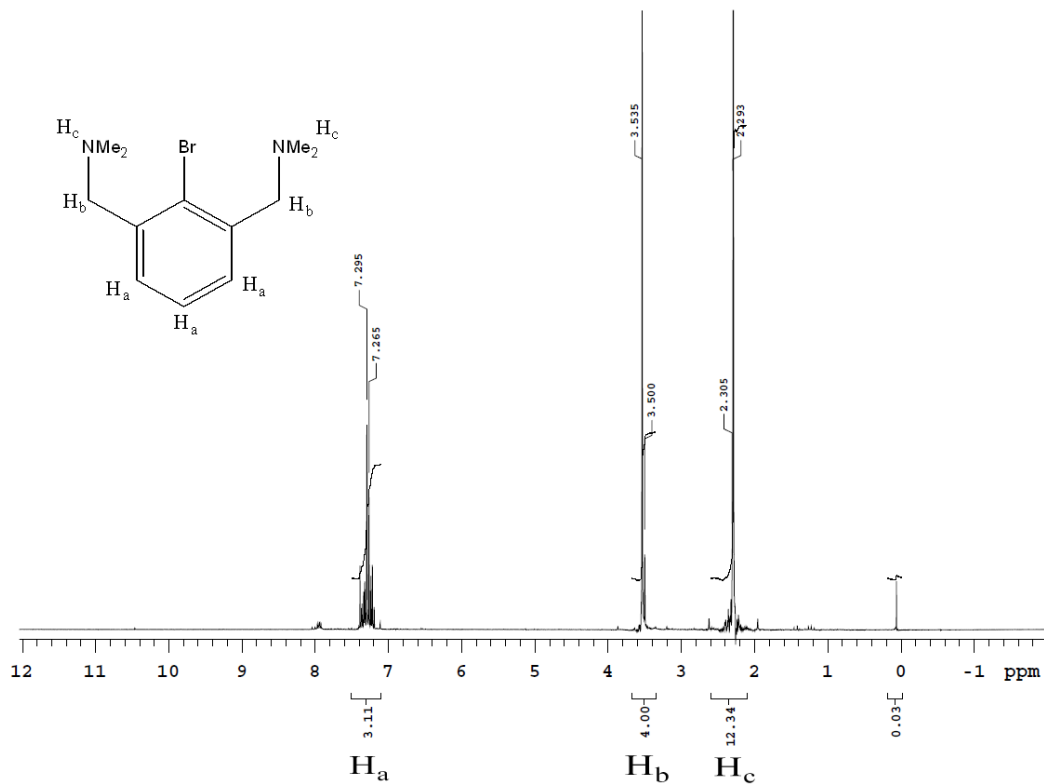


Figure A.3: 1H -NMR spectrum in $CDCl_3$ of $C_6H_3Br(CH_2NMe_2)_2-2,6$ (**6**); pincer ligand.

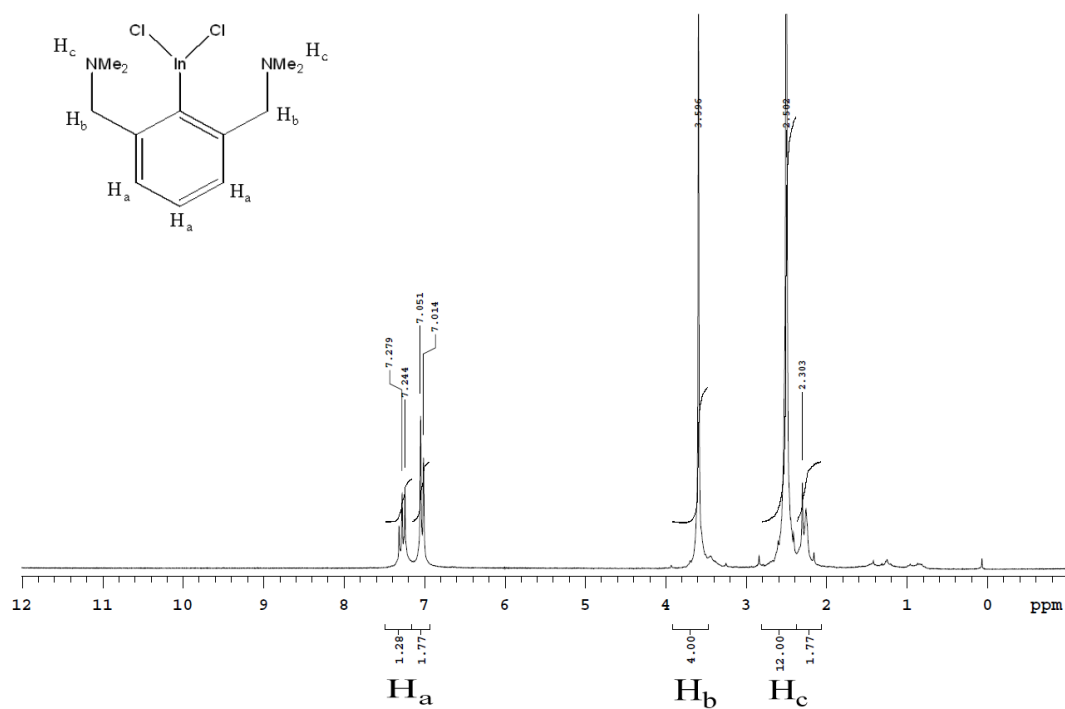


Figure A.4: $^1\text{H-NMR}$ spectrum in CDCl_3 of $(\text{NCN})\text{InCl}_2$ (**7**).

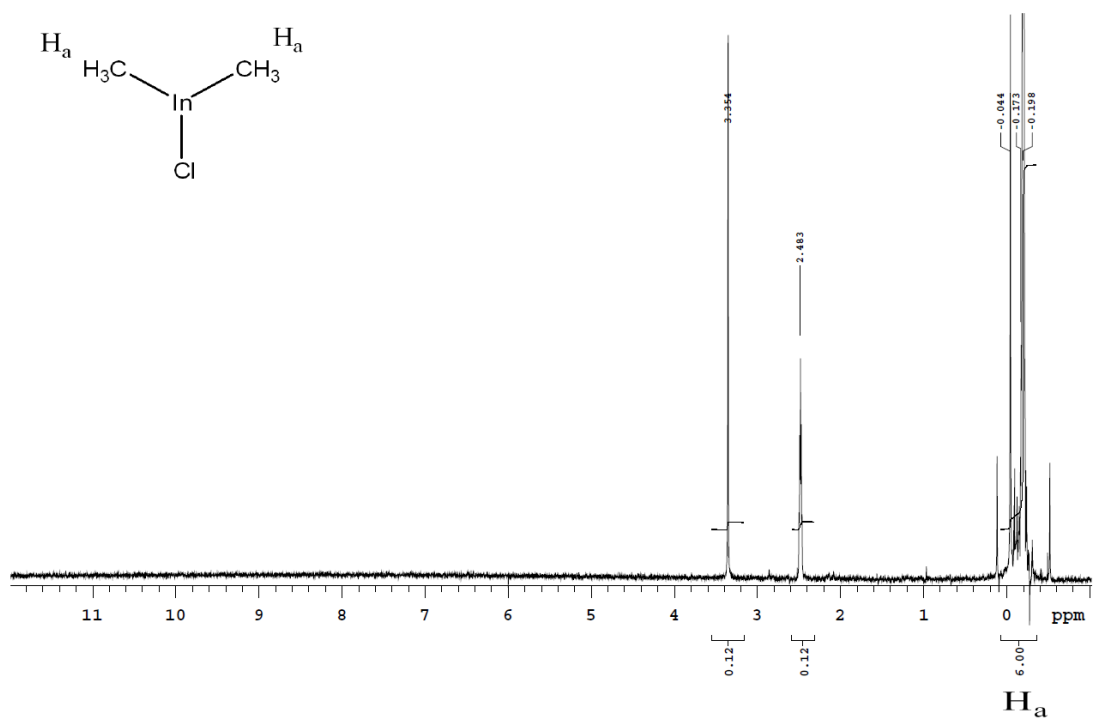


Figure A.5: $^1\text{H-NMR}$ spectrum in DMSO-d_6 of InMe_2Cl (**8**).

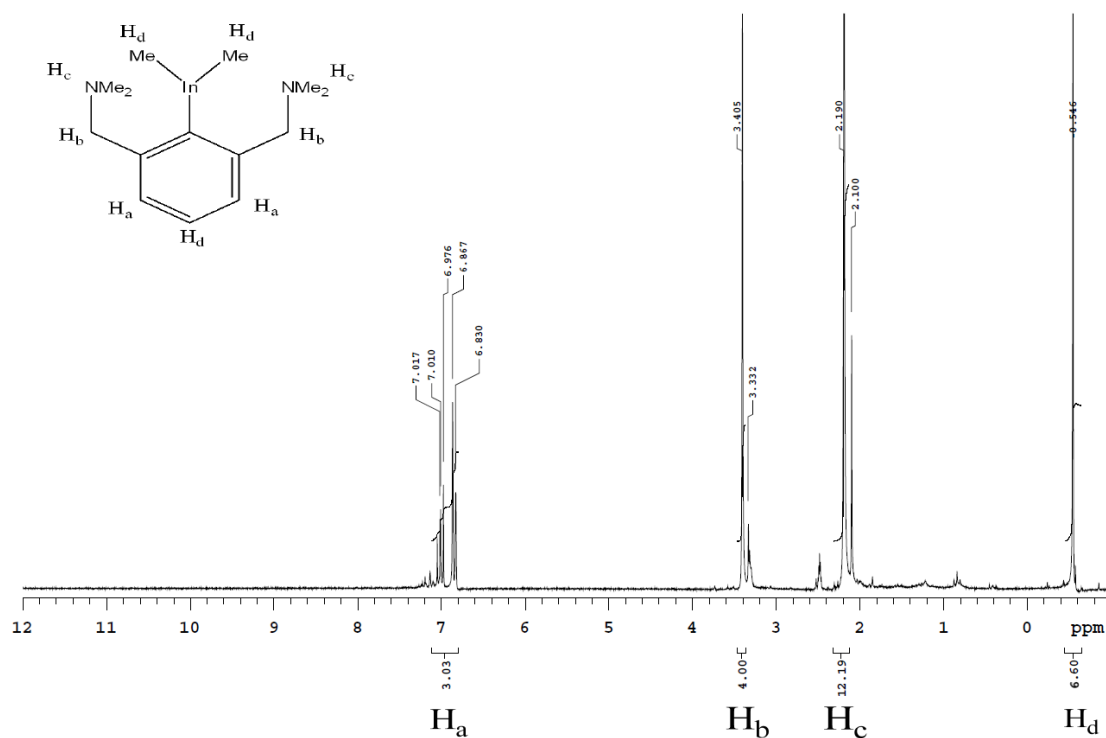


Figure A.6: ^1H -NMR spectrum in DMSO- d_6 of (NCN)InMe $_2$ (**9**).

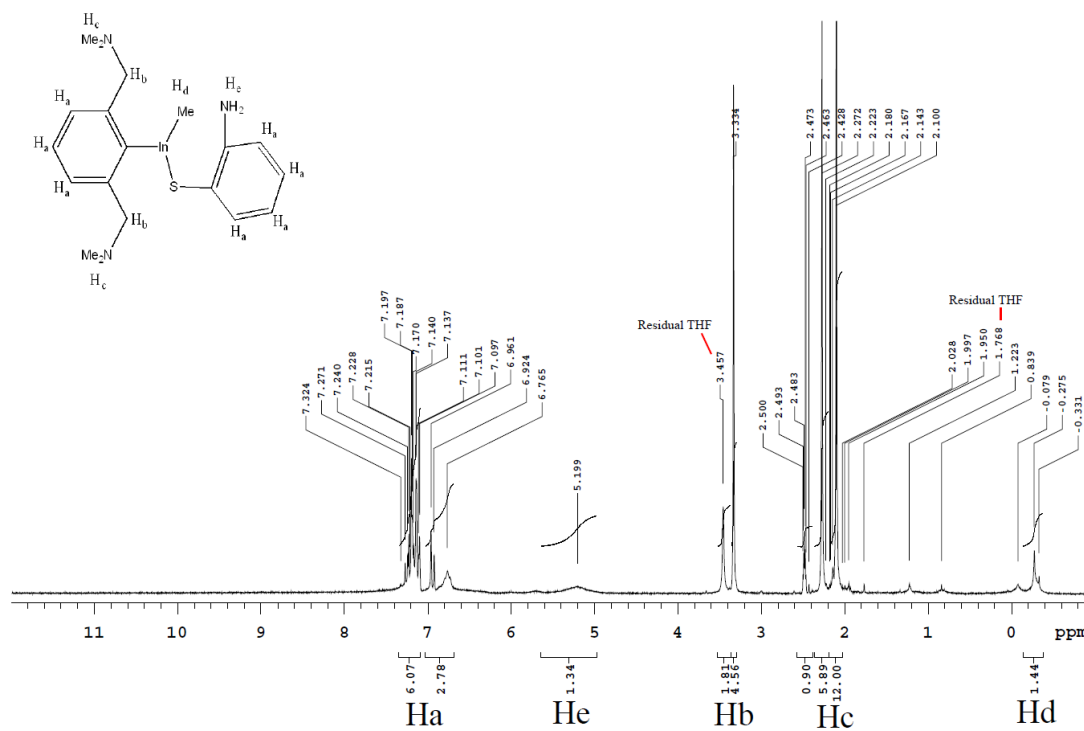


Figure A.7: ^1H -NMR spectrum in DMSO- d_6 of (NCN)InMe(H $_2$ ABT) via hydrocarbon elimination.

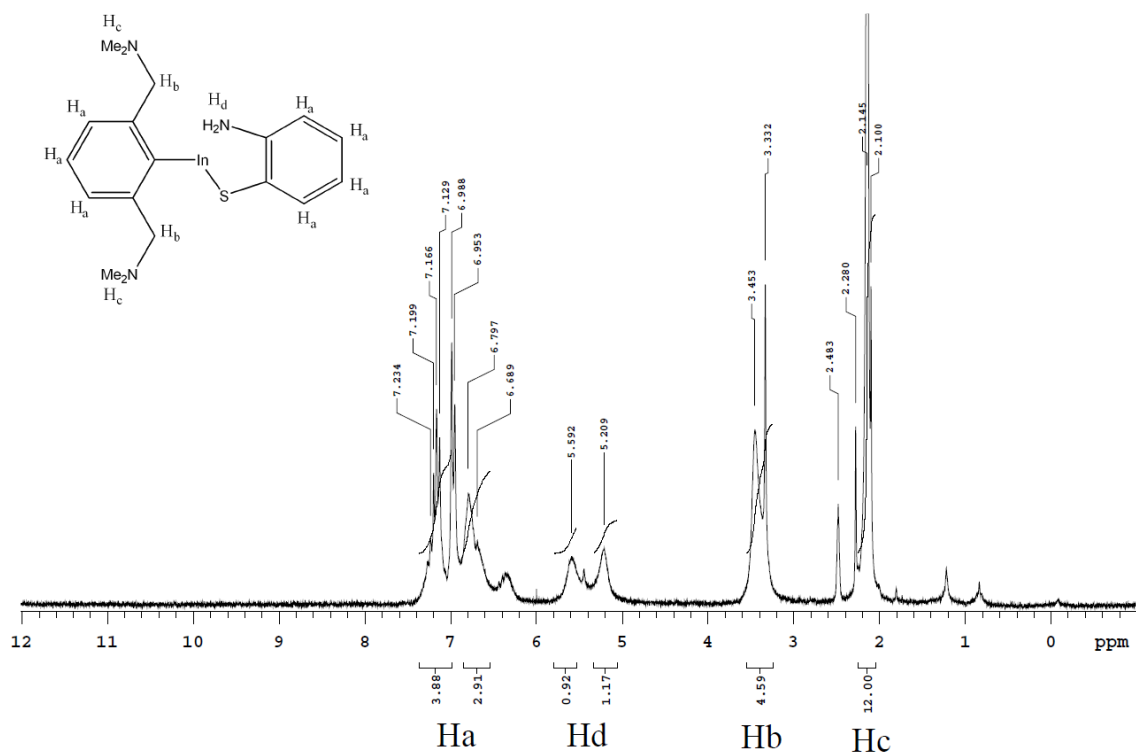


Figure A.8: $^1\text{H-NMR}$ spectrum for attempted synthesis of $(\text{NCN})\text{In}(\text{ABT})$ via sodium hydride in DMSO-d_6 .

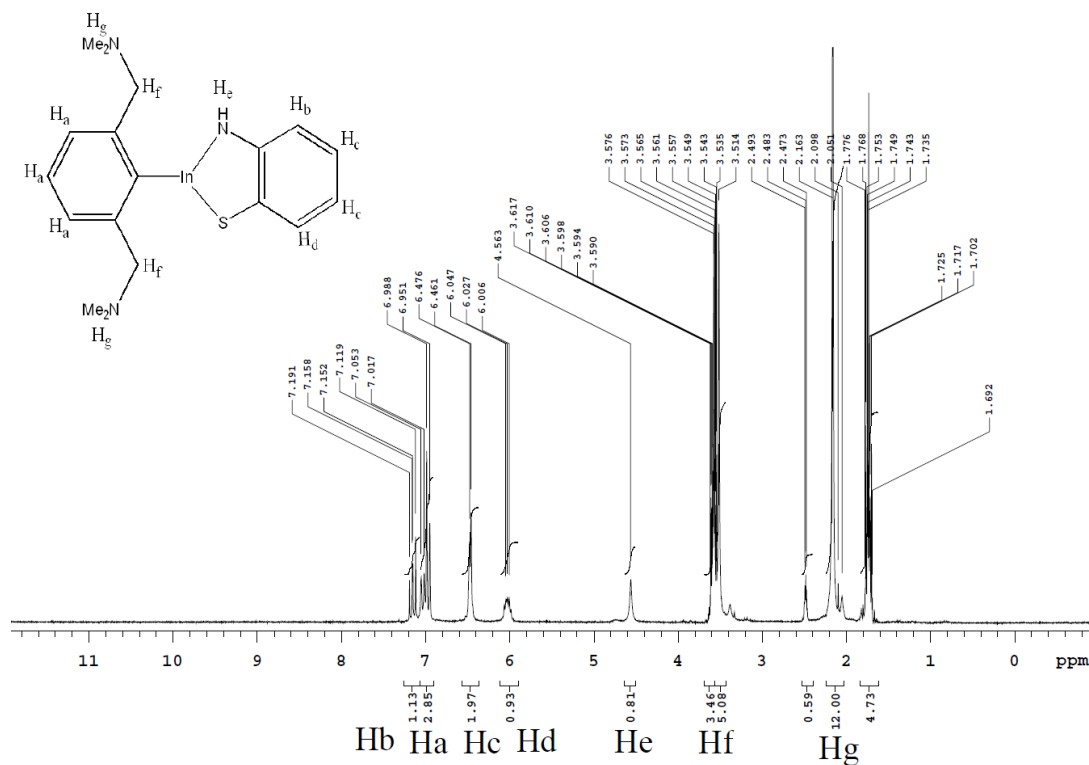


Figure A.9: $^1\text{H-NMR}$ spectrum of $(\text{NCN})\text{In}(\text{ABT})\cdot\text{LiCl}_2$ (**4**) via butyllithium in DMSO-d_6 .

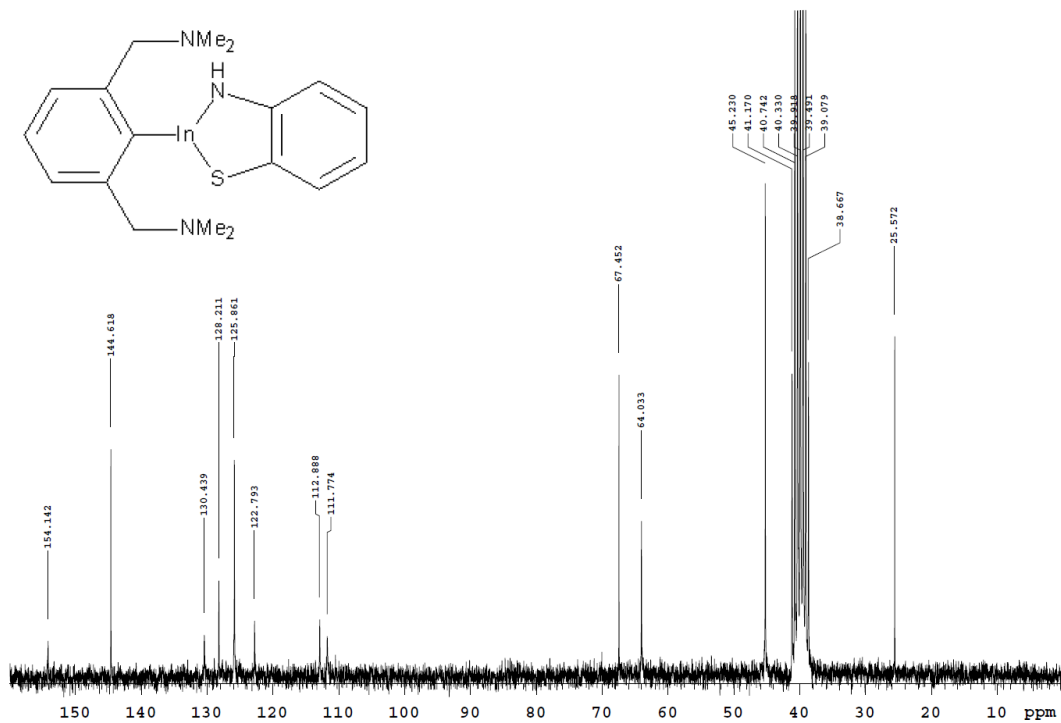


Figure A.10: ^{13}C -NMR spectrum of $(\text{NCN})\text{In}(\text{ABT})\cdot\text{LiCl}_2$ (**4**) via butyllithium in DMSO-d_6 .

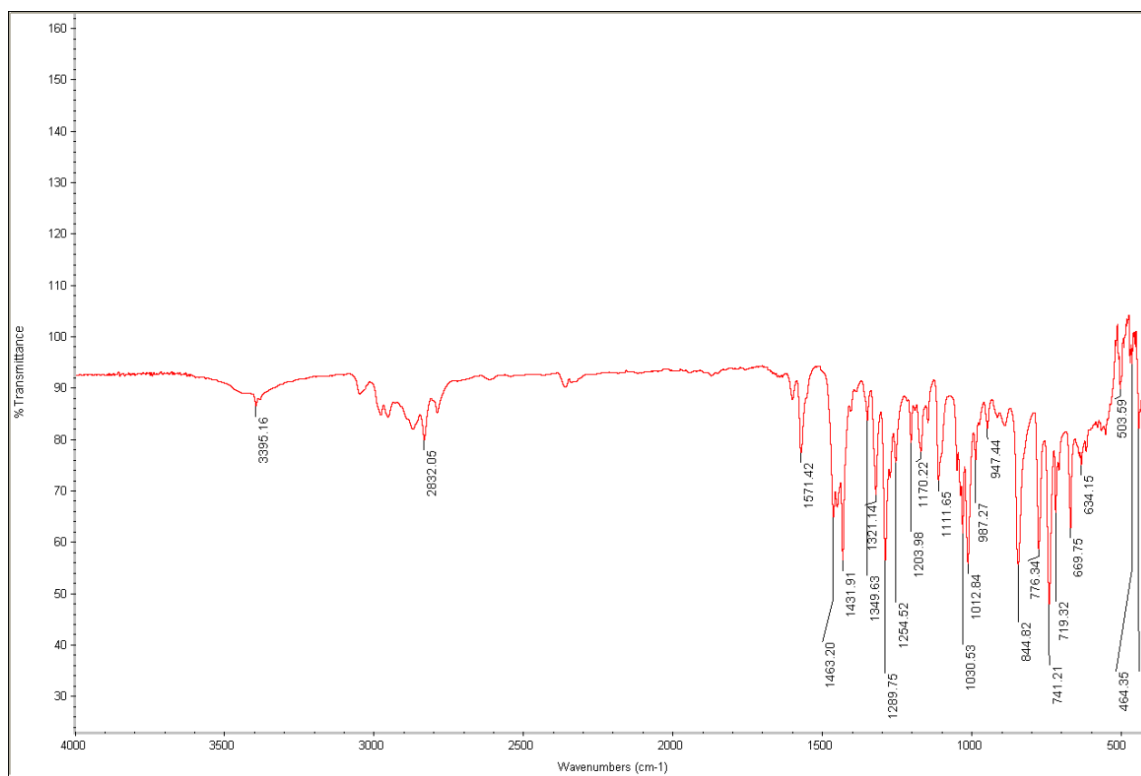


Figure A.11: FT-IR spectrum of $(\text{NCN})\text{In}(\text{ABT})\cdot\text{LiCl}_2$ (**4**) via butyllithium.

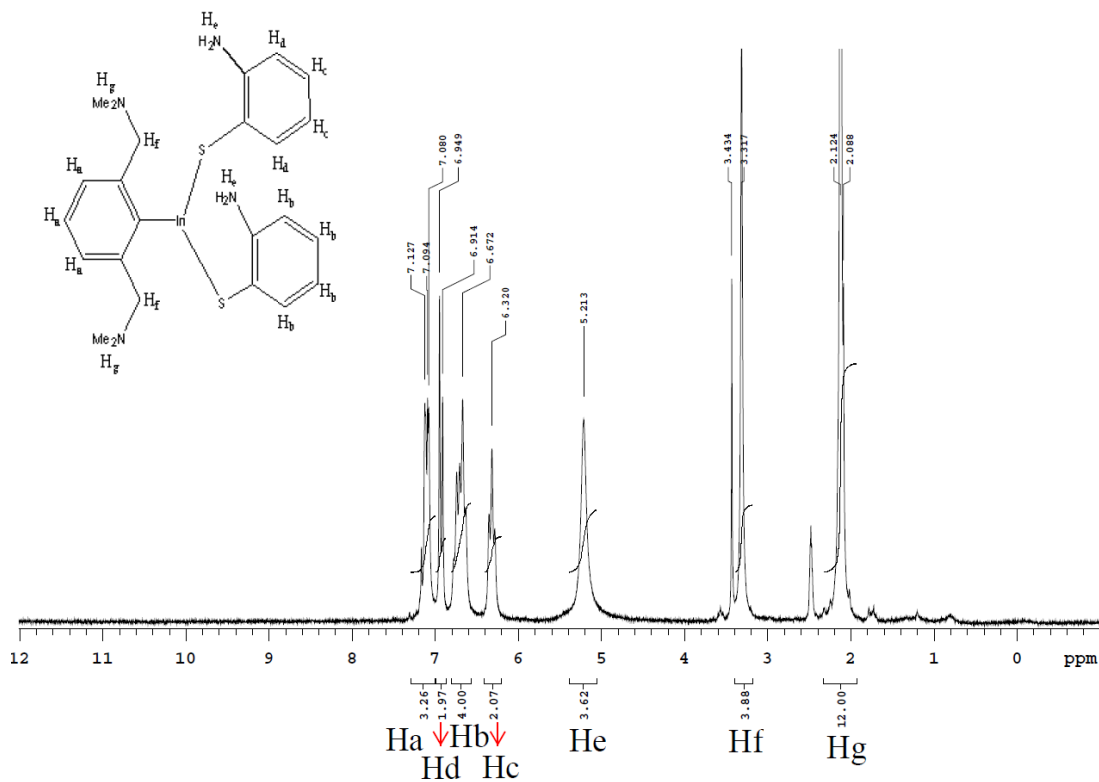


Figure A.12: $^1\text{H-NMR}$ spectrum in DMSO-d_6 of $(\text{NCN})\text{In}(\text{HABT})_2$ (10).

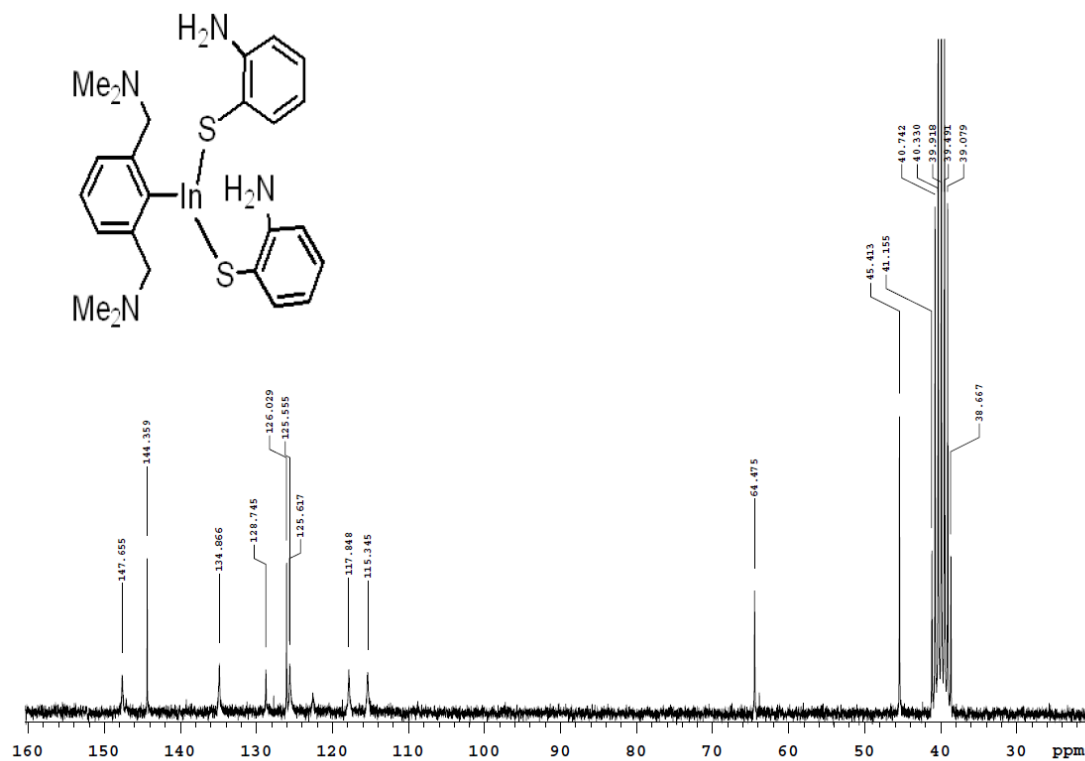


Figure A.13: $^{13}\text{C-NMR}$ spectrum in DMSO-d_6 of $(\text{NCN})\text{In}(\text{HABT})_2$ (10).

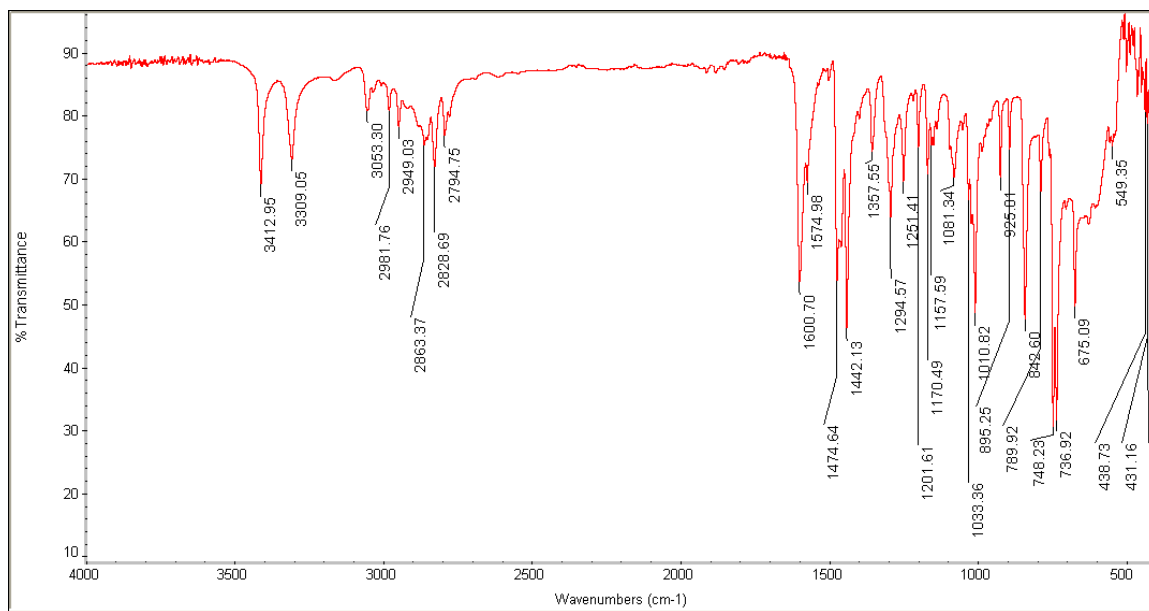


Figure A.14: FT-IR spectrum of (NCN)In(HABT)₂ (10).

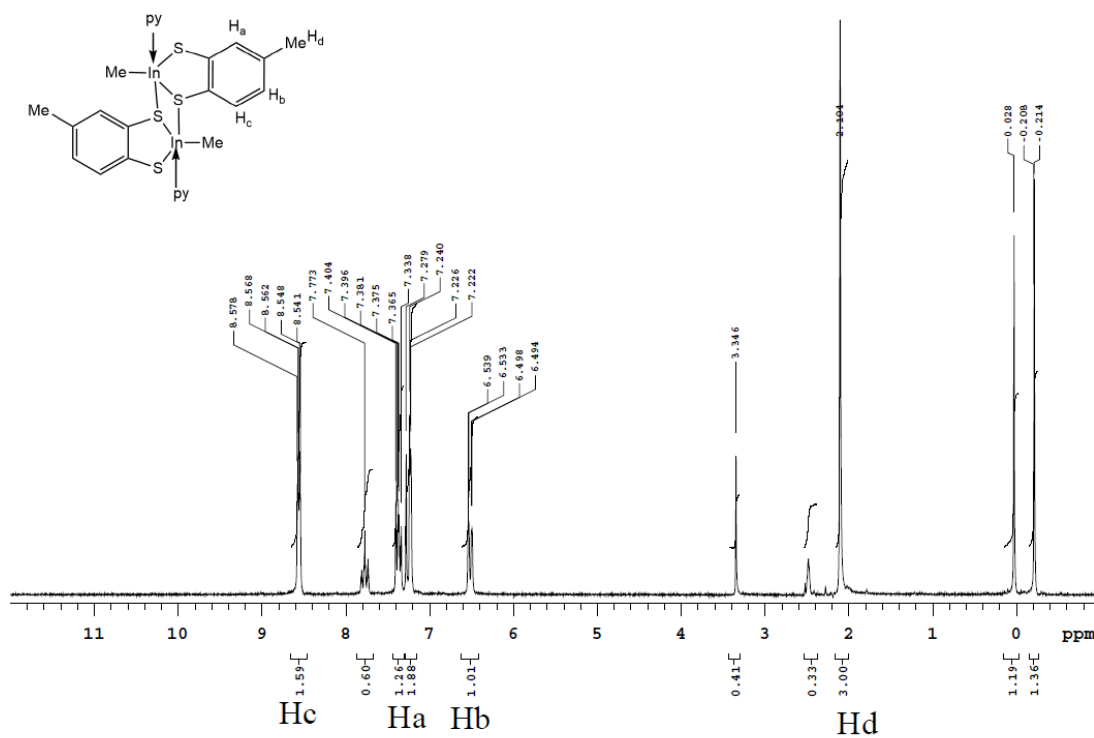


Figure A.15: ¹H-NMR spectrum in DMSO-d₆ of [MeIn(TDT)py]₂ (1) after the addition of I₂.

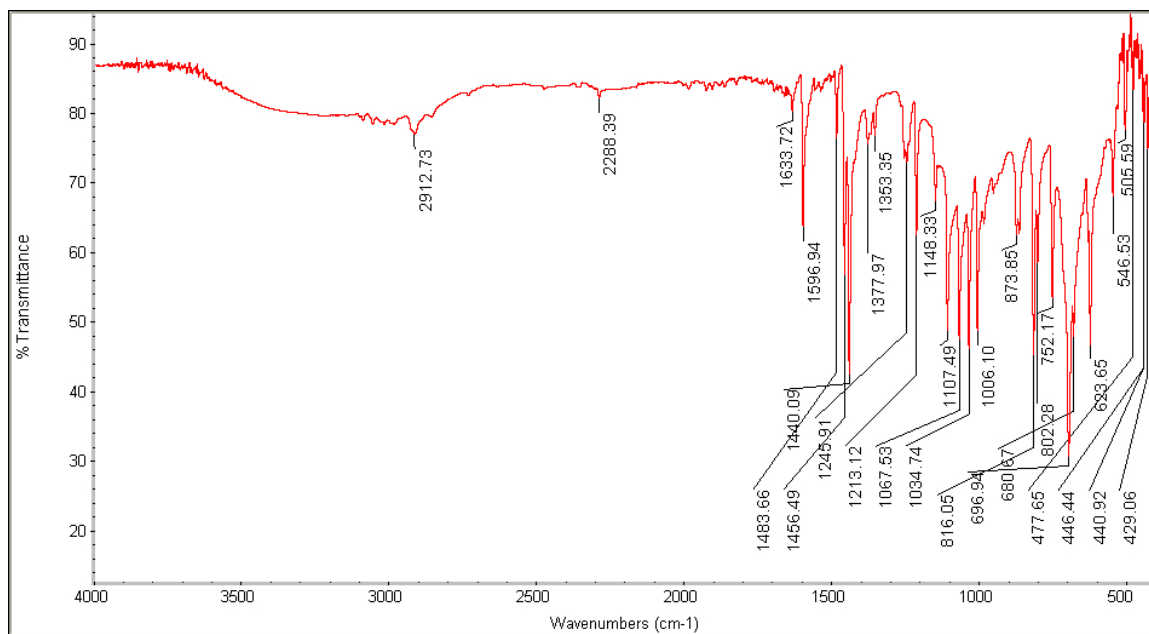


Figure A.16: FT-IR spectrum of [MeIn(TDT)py]₂ (**1**) after the addition of I₂.

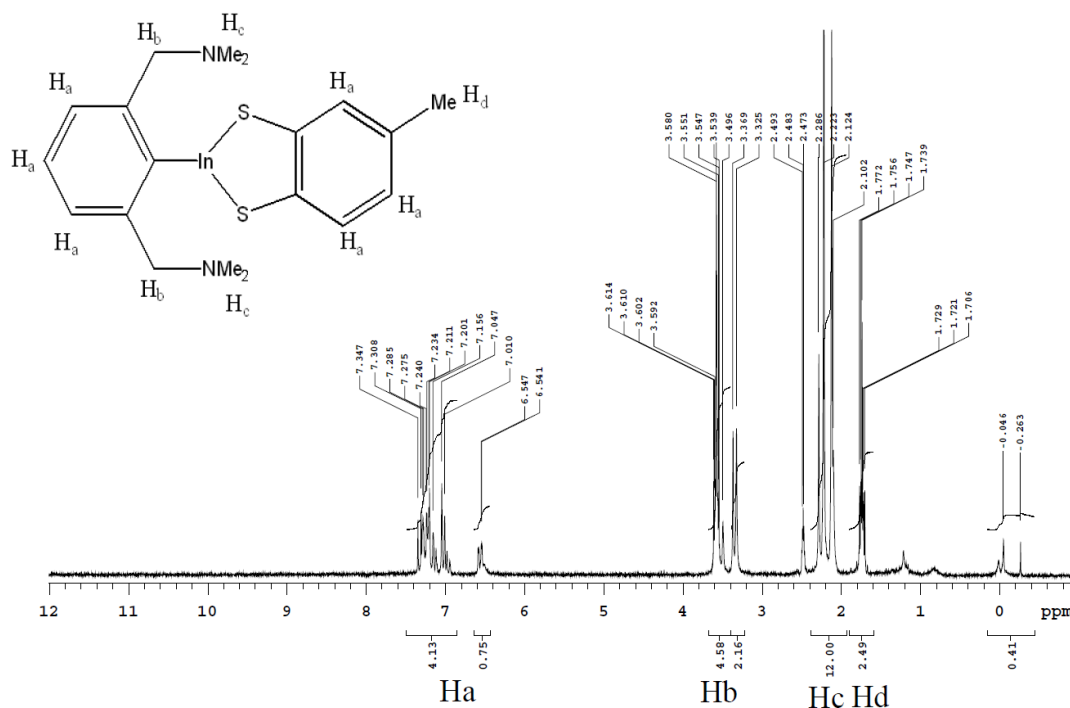


Figure A.17: ¹H-NMR spectrum in DMSO-d₆ of (NCN)In(TDT) (**2**) after the addition of I₂.

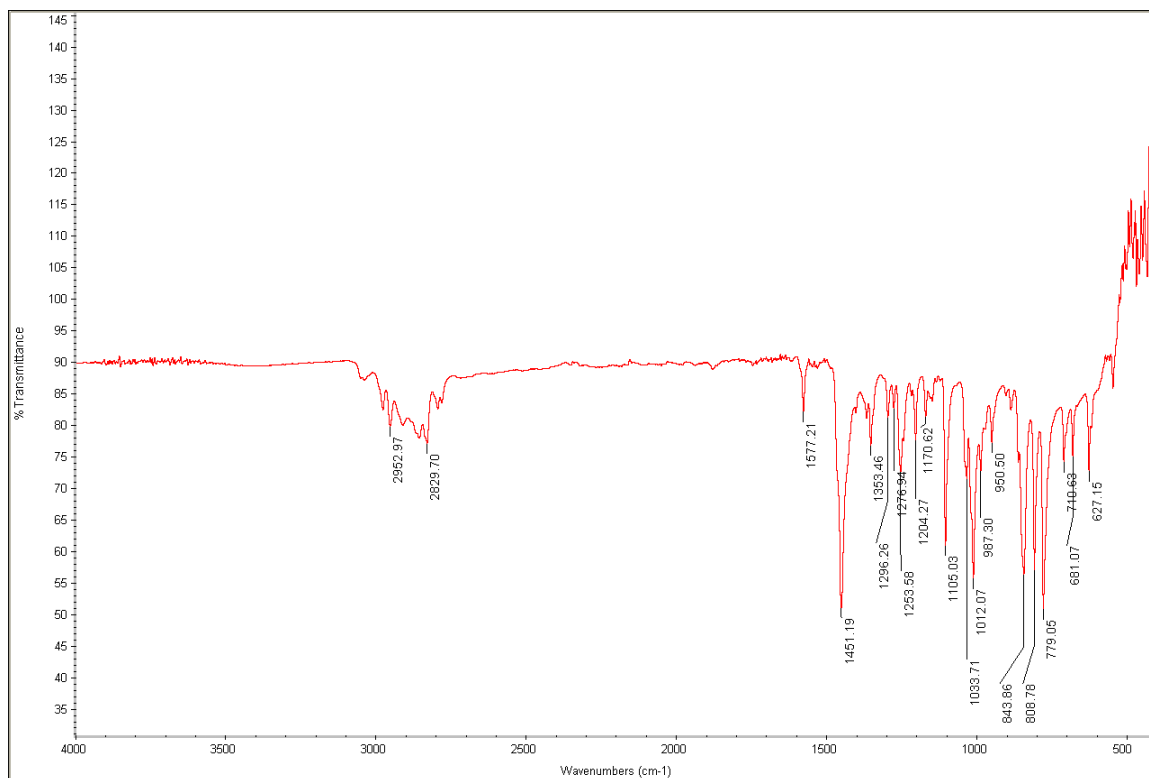


Figure A.18: FT-IR spectrum of (NCN)In(TDT) (**2**) after the addition of I₂.

Appendix B: Calculated energies of molecules using PBE1PBE-GD3BJ/def2-TZVP

Table A.1: Calculated total energies E (hartree) for geometry-optimized [MeIn(ABT)] structures and pyridine (py).

Compound	E
[MeIn(TDT)py]	-1356.00120
[MeIn(TDT)py] ₂	-2712.04659
[MeIn(TDT)py] ₂	-1604.01154
MeIn(TDT)	-1107.97376
Py	-247.990767
[MeInI(TDT)] ₂	-2238.86954

Table A.2: Calculated total energies E (hartree) for geometry-optimized neutral and cationic (NCN)In(TDT) structures and that reduced by iodine, (NCN)InI(TDT).

Compound	E
(NCN)In(TDT)	-1645.62464
(NCN)In(TDT) ⁺	-1645.38795
(NCN)InI(TDT)	-1657.05171

Table A.3: Calculated total energies E (hartree) for geometry-optimized [MeIn(ABT)] structures.

Compound	E
[MeIn(ABT)py] ₂ <i>S</i> -linked	-1947.96100
[MeIn(ABT)py] ₂ <i>N</i> -linked	-1947.96987
[MeIn(ABT)py] ₂ ⁺	-1947.74176
[MeIn(ABT)py] ₂ ⁺² singlet	-1947.41745
[MeIn(ABT)py] ₂ ⁺² triplet	-1947.40888
[MeInI(ABT)] ₂	-1474.77186

Table A.4: Calculated total energies E (hartree) for geometry-optimized neutral and cationic (NCN)In(ABT) structures and that reduced by iodine, (NCN)InI(ABT).

Compound	E
(NCN)In(ABT)	-1263.57976
(NCN)In(ABT) ⁺	-1263.36066
(NCN)InI(ABT)	-1275.028342